BROWNIAN MOTION OF MACROMOLECULES INSIDE SINGLE INTACT BIOLOGICAL CELLS: MICROSCOPE LASER LIGHT SCATTERING SPECTROSCOPY

by

JOYCE ANNE PEETERMANS

License, Vrije Universiteit Brussel, Belgium

(1978)

SUBMITTED IN PARTIAL FULFILLMENT OF THE

REQUIREMENTS FOR THE DEGREE OF

DOCTOR OF PHILOSOPHY

at

MASSACHUSETTS INSTITUTE OF TECHNOLOGY

SEPTEMBER, 1985

Signature of Author_____
Department of Physics
September 25, 1985

Certified by_____
Professor Toyoichi Tanaka
Thesis Supervisor

Accepted by_____
Professor George F. Koster
Chairman, Departmental Committee

BROWNIAN MOTION OF MACROMOLECULES INSIDE INTACT SINGLE BIOLOGICAL CELLS: MICROSCOPE LASER LIGHT SCATTERING SPECTROSCOPY

by

Joyce Anne Peetermans

Submitted to the Department of Physics on September 25, 1985,
in partial fulfillment of the requirements for
the Degree of Doctor of Philosophy

ABSTRACT

Photon correlation spectroscopy was performed on the light scattered from particles inside single, intact biological cells and from the membrane of these cells. The experimental technique is new and, so far, unique and is described in detail in this thesis. We call it Microscope Laser Light Scattering Spectroscopy (MLLSS). MLLSS is different from the commonly used dynamic laser light scattering technique developed in the 1960's in that the scattering volume is $(2\mu m)^3$ in MLLSS, a factor of 10^5 smaller than in most conventional dynamic light scattering set-ups. Incorporated in the microscope set-up is Single Cell Absorption Spectroscopy, so that scattering and absorption by the intracellular components can be monitored in parallel. The usefulness of MLLSS in small, non-biological samples is also demonstrated.

Brownian motion can be an important mechanism for intracellular transport. In fact, prevention of Brownian motion of cytoplasmic constituents is central for intracellular storing mechanisms and, in some cases, can cause disease. One example of such a disease is studied at length in this thesis: the pathologic aggregation of hemoglobin upon the deoxygenation of red blood cells of people with sickle cell anemia. The aggregation causes very much increased cell rigidity, blood stagnation in the blood capillaries and, as a result, inproper tissue and organ oxygenation. MLLSS was used to monitor, for the first time, the **reversible hemoglobin aggregation inside single, metabolically active sickle cell anemia red blood cells.** The interaction of sickle hemoglobin molecules is determined by the charge of the molecules which is in turn determined by the degree of oxygen saturation of the hemoglobin. It was believed that a one to one relation exists between this oxygen saturation and the ambient partial oxygen

pressure (pO_2). Using single cell absorption spectroscopy, we demonstrated the existence of large **cell-to-cell variability in the oxygen saturation of sickle hemoglobin at a given** pO_2. It is one of the first examples of a non-invasive study demonstrating the existence of cell-to-cell variation on intact cells. Such findings can be essential in the understanding of a disease and its symptoms.

MLLSS is also capable of studying **membrane flexibility** of single small biological cells. This was demonstrated on red blood cells and is, to our knowledge, the only cell flexibility study that does not involve exposing the cells to an external stress.

Cell differentiation is a fundamental biologic process in which the characteristics of the **single cell** are essential. We used MLLSS and conventional dynamic laser light scattering in a study of the synthesis of a crystallin protein coincident with cell differentiation in embryonic chick eye lenses.

A small MLLSS study on submillimeter gels demonstrates the utility of the technique on small **non-biologic samples.** In this case, it was used to observe critical density fluctuations and abruptly altered compressibility of a isopropylacrilamide gel undergoing a volume **phase transition.**

Thesis Supervisor: Dr. Toyoichi Tanaka
Title: Professor of Physiscs

TABLE OF CONTENTS

Chapter 1 :

INTRODUCTION

Scattered light carries important information on the scatterers in the volume illuminated by the laser beam of a light scattering experiment. The average scattered light intensity is determined by the size and shape of the particles, by their concentration and the refractive index difference between the scatterer and the solvent. The rate of scattered intensity fluctuations is determined by the hydrodynamic particle size, the viscosity of the solvent and the interactions between the particles. The light scattered from the inside of biological cells should thus provide important information on the state and content of the cytoplasm. Changes in the scattered light should also reflect cellular activity in the case of processes such as protein synthesis, protein aggregation, cytoskeletal melting etc. However, scattered light does not originate only from moving particles. It also has contributions from non-moving cell parts such as possibly a rigid cell membrane and cytoskeleton. An analysis of an intracellular phenomenon from the average scattered intensity only is thus difficult. Photon correlation spectroscopy distinguishes different frequencies in the scattered light and thus contributions from moving and non-moving scatterers. The technique is often referred to as dynamic laser light scattering spectroscopy.

Dynamic or quasi-elastic laser light scattering (QLS) has rapidly become a well established technique after its development in the early 1960's [1,2]. It has been used very successfully in the study of macromolecular motion in suspensions (for example [3-5]), of particle shape [6,7], of flow in capillaries [8,9], of formation of organized structures and associated phase transitions in systems such as gels [10], single polymers [11] and liquid crystals [12,13]. Several applications of QLS were in the field of biophysics in that the system under study was a biological system and that the question addressed was of biological or medical interest [1,7-9,14-16].

The advantages of QLS over many other techniques used in biology, is its **high spatial resolution** and its **non-invasiveness.** Typically, the length scale L of dielectric constant fluctuations that scatter light, is between a few 10Å and a few 1000Å depending on the angle between the incident laser beam and the scattered light collected for analysis. If the sample does not absorb at the wavelength of the laser, the incident beam does not affect the sample and changes that occur on the length scale L as a result of a change in conditions or as a function of time in a kinetic event, can be monitored on one and the same sample. I will illustrate the **usefulness** of and the **necessity** for such a **high spatial resolution, non-invasive technique at the level of a single biological cell** in the following two examples. One example is of clinical interest, the other addresses a fundamental question in biology.

There exists a disease, called **sickle cell anemia**, which is documented in more detail in chapter 4 and in which the hemoglobin inside the red blood cells is in monomeric form when it carries oxygen and is polymerized

when it releases oxygen. This is the result of a chemical alteration in the hemoglobin molecule, which, in the case of the disease, is called hemoglobin-S. Polymerization of the hemoglobin-S causes many complications which eventually lead to death of the patient. So far, the only temporary relief for a patient at a time of crisis is to attempt to slightly swell the red blood cells by hydrating the patient. The decreased hemoglobin-S concentration diminishes the polymerization. For this reason it was postulated that sickle cell anemia patients with naturally lower intracellular hemoglobin-S concentrations should show less severe symptoms of the disease. Such a population of sickle cell anemia patients exists [17,18]. They are peoples who's level of hemoglobin-F (fetal hemoglobin, a hemoglobin type which constitutes a small fraction of all adults hemoglobin) is unusually high. Hemoglobin-F does not polymerize when deoxygenated nor does it get included into hemoglobin-S polymers. When this hypothesis was tested in a clinical investigation [19,20], no correlation was found between the severeness of sickle cell anemia symptoms and hemoglobin-F levels. Very importantly, in this study the hemoglobin-F levels were measured by pooling the content of a very large amount of red blood cells. Therefore, it was suggested [19] that, in patients with the unusually high hemoglobin-F levels, the intracellular hemoglobin-F could be distributed unequally over the red blood cells so that the hemoglobin-S polymerization is more extensive in the low hemoglobin-F concentration cells and vise versa. This assumption could never be tested because of the lack of a technique capable of measuring hemoglobin concentration and polymerization of hemoglobin at the single red blood cell level. The technique presented in this thesis, **Microscope Laser Light Scattering Spectroscopy (MLLSS)**, is clearly capable of studying this clinical problem. Indeed, it can investi-

gate cell-to-cell differences and establish whether the present hypothesis for explaining the lack of correlation between intracellular hemoglobin-F level and severeness of sickle cell anemia symptoms is correct.

Another example in which MLLSS can be an extremely powerful tool, is in the study of **differentiating cells.** It is a question of very fundamental importance in biology to understand the driving force and the regulating factors in the process of differentiation. Differentiation occurs in the development of a living organism. It is the process in which a mother cell divides into cells with different characteristics and functions than the mother cell. This occurs mostly in embryology (for example the formation of a human being with cells of an enormous variety out of one fertilized egg cell) and in the continuous renewal of died off cells in adult tissue (for example the hematopoesis of several different blood cells out of one stem cell). Some pathologies, such as cancers, are the result of a malfunction of a differentiation process that results in the proliferative production of one type of cell. The study of any differentiation process involves the comparison of cells that were initially thought to be identical and that may have developed, differentiated into different cells. One example is found in the embryologic development of the eye lens [21-23]. More details in relation to this topic are given in Chapter 5, but at this stage it is only important to know that the lens at early stages of its development contains just one type of cell: the epithelial cells. In the adult lens, two cell types are found: the epithelial cells and fiber cells. The mitotic or cell division region of the lens is located within the epithelial cell layer. When an epithelial cells divides, the new cells either remain epithelial or become fiber cells. How is this differentiation process regulated? This system is also convenient for the study of

transdifferentiation: a cell, originally meant to become a retinal cell, can "transdifferentiate" into a lens fiber cell if placed in contact with the dividing lens epithelial cells. How does this transdifferentiation work? Up to what level of specialization can a specializing or differentiating cell transdifferentiate into another developmental track? Though these questions are very general and extremely complex to answer, one point is clear: the **individual cell** has to be studied. It is still an unresolved question whether cell differentiation is controlled mostly by factors intrinsic to the differentiating cell itself or by local variations in the ambient conditions to which the cell is exposed. We feel **MLLSS** can be very valuable in helping to address some of the aspects of this very fundamental issue by **probing changes in the absorption properties and diffusivity of intracellular components in differentiating cells.** It is capable of following one single cell throughout the differentiating process in a non-invasive way.

How special is MLLSS? Recently, biochemistry has developed a large number of fluorescent probes that specifically mark one certain molecule and, in some cases, specifically one conformation of the molecule. Because the presence and the conformation of the molecule inside a cell are sometimes directly related to the function of the cell, **fluorescent microscopy** and related **cell sorting techniques** are very important tools in modern biology. Their **spatial resolution is comparable to** the one of **MLLSS,** but **MLLSS** is much **less invasive.** Indeed, the implantation of a fluorescent probe always raises questions about the usefulness and validity of conclusions under physiologic conditions. Another modern technique is **electron microscopy.** There, the **resolution is very high,** but the **invasiveness is enormous.** It is the **combination of high resolution and non-invasiveness**

that **makes MLLSS special.** Of course, MLLSS has many **limitations.** Biological cells are usually complex systems with very many intracellular components. In such cases, it lacks the specificity of fluorescent tagging techniques. It is fair to say that **MLLSS** is **mostly useful** in **cells** that are either **simple in composition** or that show phenomena such as cytoskeletal melting, that result in **overall changes in cytoplasmic component diffusivity.**

In **MLLSS the scattering volume** is about (2 μm^3) which **is smaller than most biological cells** and smaller by a factor of about 10^5 compared to the conventional dynamic QLS set-ups. This thesis gives the first detailed description of the set-up and demonstrates the feasibility of MLLSS in single biological cells.

Chapter 2 gives a description of the different components of the set-up, a characterization of the set-up and the alignment procedure. It also explains the method for analysis of the data obtained from cells. Chapter 3 explains how we perform single cell absorption spectroscopy incorporating an optical multichannel analyzer into the MLLSS set-up. The most extensive study done with MLLSS was on red cells of normal blood and of sickle cell anemia blood. Chapter 4 shows several experiments on these cells and demonstrates their importance in establishing the utility of MLLSS in biological and medical problems. Another study was done on developing chick embryo lenses and these experiments are explained in Chapter 5. Finally, Chapter 6 gives a brief list of suggested improvements to be made to the set-up and talks about some systems other than red blood cells or chick embryo lens cells that were briefly studied during this early work with the MLLSS set-up.

REFERENCES

[1] G.B. Benedek; Polarization, matter and radiation; Presses Universitaires de France, Paris, 1969

[2] H.Z. Cummins and H.L. Swinney; Progress in optics; Volume 8, Ed. E. Wolf, North Holland Publ.Co., Amsterdam, 1970

[3] Cannell macromolecular motion

[4] R. Finsy et al.; Light scattering study of the diffusion of interacting particles; J.C.S.FaradayII, 76 , 767-775, 1980

[5] N. Ostrowsky et al.; Exponential sampling method for light scattering polydispersity analysis; Optica Acta 28 , 1059-1070, 1981

[6] D. Schaefer et al.; Spectrum of light scattered from tobacco mosaic virus; J.Chem.Phys. 55 , 3884-3895, 1971

[7] Mazer bile salts

[8] T. Tanaka et al.; Blood velocity measurements in human retinal vessels; Science 186 , 830-831, 1974

[9] R. Johnson; Laser Doppler microscopy: especially as a method for studying Brownian motion and flow in the sieve tubes of plants; The application of laser light scattering to the study of biological motion; Eds. J.Earnshaw and M.Steer; Plenum Press, New York, 1983

[10] T. Tanaka et al.; Spectrum of light scattered from a viscoelastic gel; J.Chem.Phys. 59 , 5151-5159, 1973

[11] I. Nishio et al.; First observation of the coil-globule transition in a single polymer chain; Nature 281 , 208-209, 1979

[12] LC Litster

[13] V. Taratuta et al.; Light scattering study of a polymer nematic liquid crystal; Phys.Rev.Lett. 55, 246-249, 1985 Light scattering study of a polymer nematic liquid crystal

[14] D. Schaefer et al.; Spectrum of light quasielastically scattered from tobacco mosaic virus; J.Chem.Phys. 55, 3884-3895, 1971

[15] S. Ishiwata et al.; A dynamic study of F-actin-tropomyosin solutions by quasi-elastic light scattering; J.Phys.Soc.Japan 30, 302, 1971

[16] H. Martindale et al.; Examination of insulin formulations using quasi-elastic light scattering; Diabetes 31, 364-366, 1982

[17] G. Dover et al.; Individual variation in the production and survival of F cells in sickle-cell disease; NewEng.J.Med. 299, 1428-1435, 1978

[18] L. Sewchand et al.; The effect of fetal hemoglobin on the sickling dynamics of SS erythrocytes; Blood Cells 9, 147-160, 1983

[19] D. Powars et al.; Lack of influence of fetal hemoglobin levels or erythrocyte indices on the severity of sickle cell anemia; J.Clin.Invest. 65, 732-740, 1980

[20] M. Stevens et al.; Fetal hemoglobin and clinical severity of homozygous sickle cell disease in early childhood; J.Pediat. 98, 37-41, 1981

[21] J. Piatigorsky; .....; Differentiation 19 , 134-..... , 1981

[22] J. Genis-Galvez et al.; .....; Exp.Eye Res. 7 , 593-...., 1968

[23] j. Piatigorsky et al.; Biology of the epithelial lens cells in relation to development, aging and cataract; Eds. Courtois & Regnault, Inst.Nat.de la Sante et de la Rech.Med. 60 , 85-104, 1976

Chapter 2 :

MICROSCOPE LASER LIGHT SCATTERING SPECTROSCOPY (MLLSS)

2.1 CONVENTIONAL VERSUS MICROSCOPE DYNAMIC LASER LIGHT SCATTERING SPECTROSCOPY; THE GOAL OF MLLSS

Dynamic or quasi-elastic laser light scattering or photon correlation spectroscopy was developed in the early 1960's as a method to detect the movement of macromolecular particles through an analysis of the fluctuations in the intensity of the light scattered by these particles. The principle, underlying theory and some of the applications of this technique can be found in many places. Among these, a stimulating, early overview was written by G.B.Benedek [1] and useful books are written by B.Chu [2] and edited by H.Z.Cummins and E.R.Pike [3] some years later. In this technique, which may well be called conventional because of its wide spread success and application, the volume from which the scattered light is analyzed is typically $(0.1mm)^3$. This is much larger than almost all biological cells.

The main motivation behind the development of microscope laser light scattering spectroscopy (MLLSS) was to diminish this scattering volume to a size smaller than most biological cells. Such a technique would then be capable of detecting macromolecular motion inside single,

intact biological cells. In June 1983, I.Nishio et al. published the first report of such a set-up [4]. The contribution of the author of this thesis is to improve the apparatus in its various functions and to incorporate single cell absorption spectroscopy in the set-up. The scattering volume in MLLSS is smaller than in the conventional set-ups by a factor of 10^5 bringing it to $(2\ \mu m)^3$. This volume is smaller than many biological cells.

In this chapter, the MLLSS set-up is described and characterized in detail. Before that, I wish to mention some earlier work done on single cells using laser light scattering and some other work that was aiming at decreasing the scattering volume. Maeda et al. [5] built a similar set-up to ours, but, due to technical limitations, the scattering volume in that experiment was about $100\mu m^3$, which is larger than most cells. They reported measurements on polystyrene solutions. In 1982, Coletta et al. [6] published data taken on single red blood cells illuminated by an argon laser, which denatures the hemoglobin and causes aggregation. The aggregation was studied through the change of the scattered intensity with time under the argon laser illumination. A few groups [7,8] have performed dynamic laser light scattering on single cells and monitored mostly cytoplasmic flow. The cells under study were however very large (a few mm) and the studied region was of the order of 100 μm^2 in area. An extended feasibility study for detection of intracellular macromolecular motion in $(2\mu m)^3$ is found in Chapter 4 of this thesis.

2.2 MICROSCOPE LASER LIGHT SCATTERING SPECTROSCOPY; THE BLOCK SCHEME

A block scheme of the MLLSS set-up is shown in Figure 2.1. The components that are identical to all photon correlation experiments are the laser, the photo-multiplier tube (PMT), the amplifier-discriminator, the autocorrelator and a computer for data analysis. I will only superficially describe these components. The difference between conventional dynamic laser light scattering and MLLSS lies in the region between the laser and the PMT. It consists of fiber optic guides for the incident and the scattered light, the optics that focus the incident beam onto the sample and the optics that determine the region from which scattered light is picked up for detection and analysis. The last two portions of the set-up are incorporated in the microscope and are the subject of section 2.3. The fiber optic components, however, are discussed here.

2.2.a. The Laser

The laser used in all the MLLSS experiments is a He-Ne laser (Spectra Physics 124A 15 mW). The most important reason for this choice lies in the wavelength (λ=6328Å). Indeed, the cell that was chosen to demonstrate the utility of MLLSS in biology and medicine is the red blood cell. It contains hemoglobin which is red and thus hardly absorbs at the wavelength of the He-Ne laser. The use of an Argon laser (green line λ=5145Å) would result in the immediate cooking of the cells as is illustrated briefly in section 4.7.

It is a necessity to use a laser as the incident light source, because of the constant intensity and coherence of the beam on time

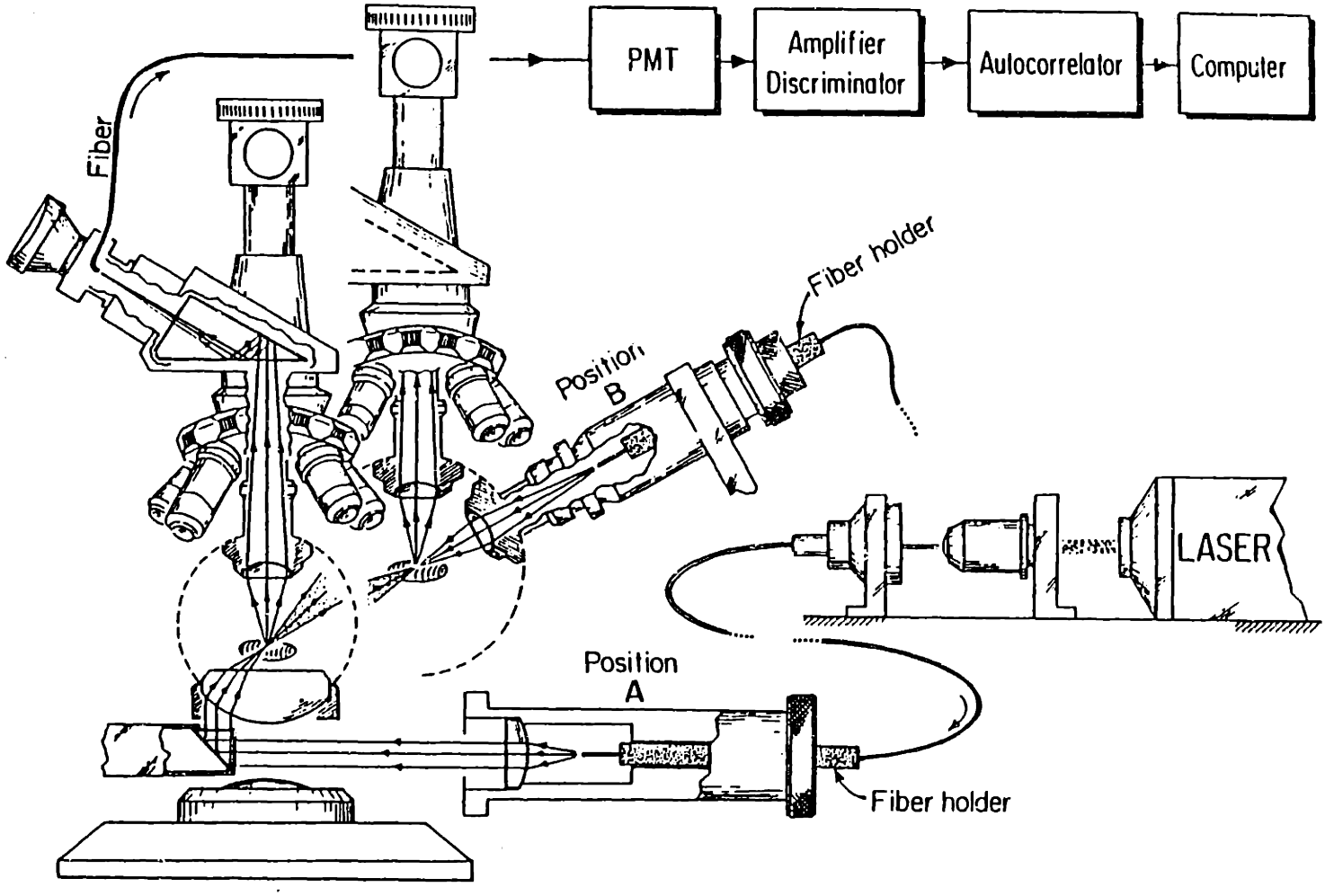

Figure 2.1 Block scheme of the Microscope Laser Light Scattering (MLLSS) set-up

scales larger than the characteristic times of the Brownian motion of macromolecules in suspension. The scattered light intensity fluctuations have to originate entirely from the sample. Diffusion coefficients for such scatterers vary roughly between 10^{-7} and $5x10^{-10}$ cm^2/sec at temperatures around room and body temperature and in solvents that have viscosities close to that of water. The scattered intensity fluctuations caused by a suspension of such particles have different characteristic life times. The characteristic wavelength of detected fluctuations depends on the probe size of the experiment which records the intensity fluctuations (see below for more details). In typical dynamic light scattering experiments, this life time varies between 50 μsec and 1 sec. The scattered intensity fluctuations result from interference between the light scattered by individual particles and the incident beam therefore has to be coherent over times on the order of 1 sec or more. The average intensity of the incident beam has to be constant over times of the order of the measurements, which is on the order of 1 minute in most of our experiments. If the incident intensity has an erratic behavior on this time scale, or if it is incoherent over times of the order of 1 second, it becomes impossible to tell which portion of the fluctuations in the scattered light intensity originates from movement of the macromolecules. Lasers have the required coherence and stability.

2.2.b. The Photo-Multiplier Tube (PMT)

The PMT is the retina of the light scattering experiment: it transforms the electric field (photons) scattered by the sample under

study into electric pulses. The number of pulses per unit time is proportional to the scattered intensity in that unit time. This sequence of pulses is called the photocurrent. An incident photon hits the photo-cathode and a photo-electron is emitted, which is attracted towards the anode. This is the principle of the photo-electric effect. The PMT has a built in amplifier: the photo-electron is attracted onto a series of electrodes called dynodes, between the photo-cathode and the final anode. At each dynode, secondary electrons are emitted. When the voltage on the dynodes is well regulated, this mechanism can yield an amplification of up to 10^{10}. It is called the gain of the PMT.

In this work the PMT was an EMI model 9863B-350 which has a cathode diameter of 9 mm. The housing for the PMT contains the circuit that regulates the different voltages required for each electrode in the PMT. It also provides shielding from external electro-magnetic radiation. We used a Pacific model 3262RF housing. The light scattered from biological cells is usually sufficiently intense so that the dark count level of the PMT is not a concern.

2.2.c. The Amplifier-Discriminator

The amplifier-discriminator is a Pacific model AD6. It transforms the photo-current which is the output of the PMT, into a sequence af short (order of 10 nsec) block pulses. These pulses can be counted during a time ΔT centered around a time t. This yields a number $n(t,\Delta T)$ which is proportional to the average scattered light intensity $I(t)$ during ΔT centered at t:

$$n(t,\Delta T) = C\ \Delta T\ I(t) \qquad 2.1$$

where C is an instrumental constant that reflects the quantum efficiency and the sensitivity of the detector.

2.2.d. The Autocorrelator

The autocorrelator is next in the blockscheme: it is fed the sequence of pulses, all of the same height and length, that are the output of the PMT-amplifier-discriminator system. Two 4-bit correlators were used in this work. One is a 64 channel Nicomp correlator and the other a 136 channel Malvern-Brookhaven Instruments correlator. The output of this instrument is an intensity autocorrelation function which I will call $c(\tau)$. The scattered intensity fluctuations are analyzed in the form of functions $c(\tau)$, which constitute the "raw" data of the light scattering experiments. The functions $c(\tau)$ are constructed from the pulse count:

$$c(\tau) = \langle n(t,\Delta T).n(t+\tau,\Delta T)\rangle_t \qquad 2.2$$

and are proportional to the intensity autocorrelation functions $c_I(\tau)$ defined as

$$c_I(\tau) = \langle I(t)I(t+\tau)\rangle_t \qquad 2.3$$

Here $\langle\ \rangle_t$ indicates an average over the total time of the experiment, ΔT is the time span centered around t, during which the pulses are counted and τ is a multiple of ΔT. ΔT is called the clocktime or sampling time. It varies between 2μsec and 200μsec in this work. In a correlator with

N channels, $\tau = \Delta T, 2\Delta T, \ldots, N\Delta T$. In practice one always works with correlation functions that are normalized by their value at $\tau=0$. From now on, I will drop the subscript I and refer to the intensity autocorrelation functions as $c(\tau)$. Section 2.5 is devoted in part to $c(\tau)$.

2.2.e. The Computer

The computer used for all data analysis is a Charles River Data MF-211 with a PDP 11-73 processor under VENIX operating system. All programs, some of which are extensive, are written by Dr. Gerry Swislow (especially the "doit" program for the analysis of the autocorrelation functions and the "plot" program for various kinds of plotting) and by Dr. Izumi Nishio (especially the "spec" program for analysis of the absorption spectra (see Chapter 3)).

2.2.f. The Optical Fiber Components

The optics that determine the scattering volume of the experiment are all incorporated in the microscope at the center of the set-up. The incident laser light is led into that region by a single mode optical fiber and the scattered light picked up by an optical fiber bundle that directs it to the PMT. I wish to briefly discuss these two fiber components.

The incident beam in a dynamic light scattering experiment should be coherent on the time scales discussed in the section on the laser source (section 2.2.a). Moreover, the wavevector of both the incident

and the scattered field should be well defined in order for the quantitative analysis of the data to be possible. The incident beam should be as close as possible to a plane wave

$$\vec{E}_i(\vec{r},t) = \vec{n}_i\, E_o \exp i(\vec{k}_i\cdot\vec{r}-\omega_i t) \qquad 2.4$$

where $\vec{n}_i$ is a unit vector in the direction of polarization of the incident beam, E_o is the amplitude of the incident electric field, $\vec{k}_i$ the incident wave vector and ω_i the frequency of the incident light. $\vec{r}$ is a position vector inside the scattering volume. This electric field is scattered from inhomogeneities in the dielectric constant at the location $\vec{r}$. The single mode optical fiber guaranties that the desired properties of the incident laser beam are conserved as well as possible. Figure 2.2.a shows the cross section of an optical fiber. The inner part or "core" has an index of refraction n_1 which is higher than the index n_2 of the mantel or "cladding": $n_1 > n_2$. Appendix II-1 gives the derivation of the elementary results that are mentioned ahead. In this context, I found reference [9] very useful *. Any ray that hits the core-cladding interface at an angle $\theta_1 > \theta_c$, where $\theta_c = \mathrm{Arcsin}(n_2/n_1)$, undergoes total internal reflection. The numerical aperture NA of the

---

* Some optical fibers, not the one we used in this experiment, have a parabolic refractive index profile which compensates for multimode distortion in multimode fibers. In these fibers, called graded index fibers, the core refractive index decreases parabolically with distance from the core center. To go from one point on the core axis to another, a ray that crosses the core axis and is bent back to the axis, travels a longer distance than an axial ray. The time of travel is however the same for both rays in a parabolic profile fiber since the propagation speed is higher in the lower refractive index regions. Though such graded index fibers could be used for this experiment, the single mode fiber is more perfect in yielding a Gaussian beam profile and since it is not a problem here to work with small core diameters, we used a single mode fiber.

fiber is determined by the maximum angle θ_0 at which an incident ray undergoes total internal reflection. It is related to n_1 and n_2 through $NA = (n_1^2-n_2^2)^{1/2}$. A single mode fiber is typically one with a small numerical aperture and a small core diameter d (see Appendix II-1). In order to focus the laser beam onto the core of such a fiber, one has to use a lens that forms a small focal spot. In our case, the focusing lens is a Nikon 40DL 0.65 and the single mode fiber is the only Corning Glass commercial grade fiber available up to 1984. (see Appendix II-1 for more details). The beam at the exit of the optical fiber, has a Gaussian profile with one maximum as illustrated in Figure 2.2.b. This means that the intensity I(r) of the incident beam should have a Gaussian profile with respect to the distance r from the center of the beam:

$$I(r) = I_0 \exp(-2r^2/w_0^2) \qquad 2.5$$

where $r=w_0$ is the position where the intensity is $1/e^2$ times the maximum value I_0 at the center. This beam can be used to form the small focal spot size required for the MLLSS experiment as is explained in section 2.3. If the optical fiber were not a single mode fiber, the laser light at its exit would have several maxima and it would be extremely difficult to align the system in such a way that all beam fractions (the different Gaussian regions in the beam) would interfere constructively after being refocussed by the microscope lenses onto the sample.

The scattered light is collected by a single fiber embedded in the eyepiece of the microscope. This fiber is then connected to a optical fiber bundle that directs the scattered light to the PMT. The bundle does not maintain the Gaussian beam profile at all, but since photon correlation spectroscopy detects photocurrents proportional to the

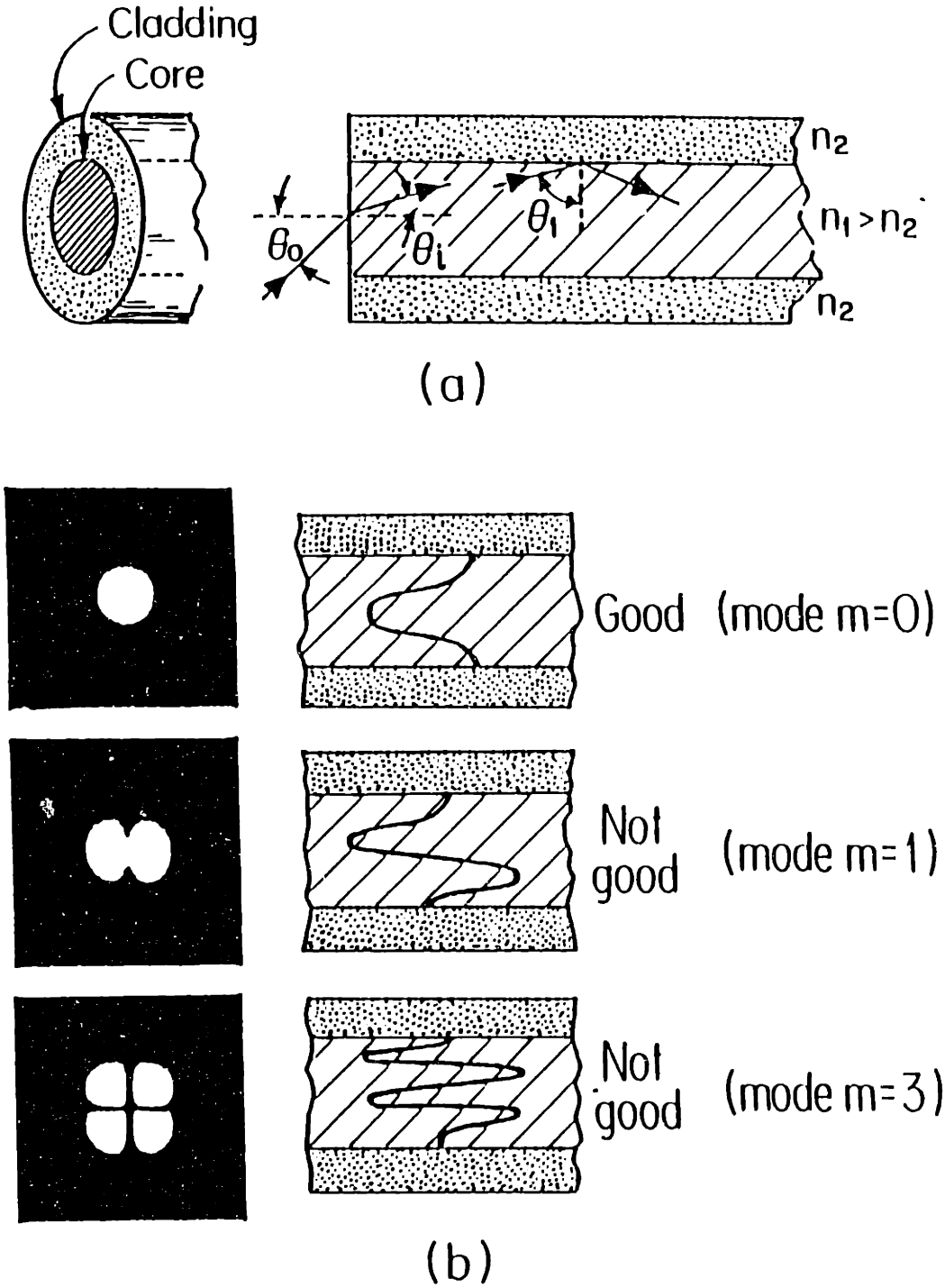

Figure 2.2 (a)Diagram of Optical Fiber (b)Beam profiles of a few Modes in an Optical Fiber

scattered field intensity, this is not a problem. The output of the bundle is placed very close to the PMT's photo-cathode. The photo-cathode is large enough to generously match the area of the fiber bundle. The reason for the use of fiber bundle is that it is much stronger than the very thin single mode fiber. A fiber bundle always contains a fraction of dead fibers (fibers that are interrupted between the ends of the bundle). Therefore bundle is not useful in experiments in which the scattered intensity is weak. This is not usually the case in MLLSS on biological cells however.

2.3 MICROSCOPE LASER LIGHT SCATTERING SPECTROSCOPY: THE CENTRAL REGION

2.3.a. The Optical Components

The exit of the single mode fiber that guides the laser beam from the laser to the central region of the MLLSS set-up is fixed in the center of a cylindrical tube. This fiber holder can slide into position A or B as shown in Figure 2.1. In both positions the beam is focussed onto the sample which sits on the microscope stage. Light is scattered in all directions. Picked up for analysis is the scattered light that comes into the microscope objective lens vertically above the sample. This lens makes either a real image on the photographic film of a camera mounted on top of the microscope tube or it forms a virtual image seen through the eyepieces. This is illustrated in Figure 2.3. The pick-up optical fiber which is connected to the fiber bundle as discussed above, has its inlet at the real image plane in front of the eyepiece (the real

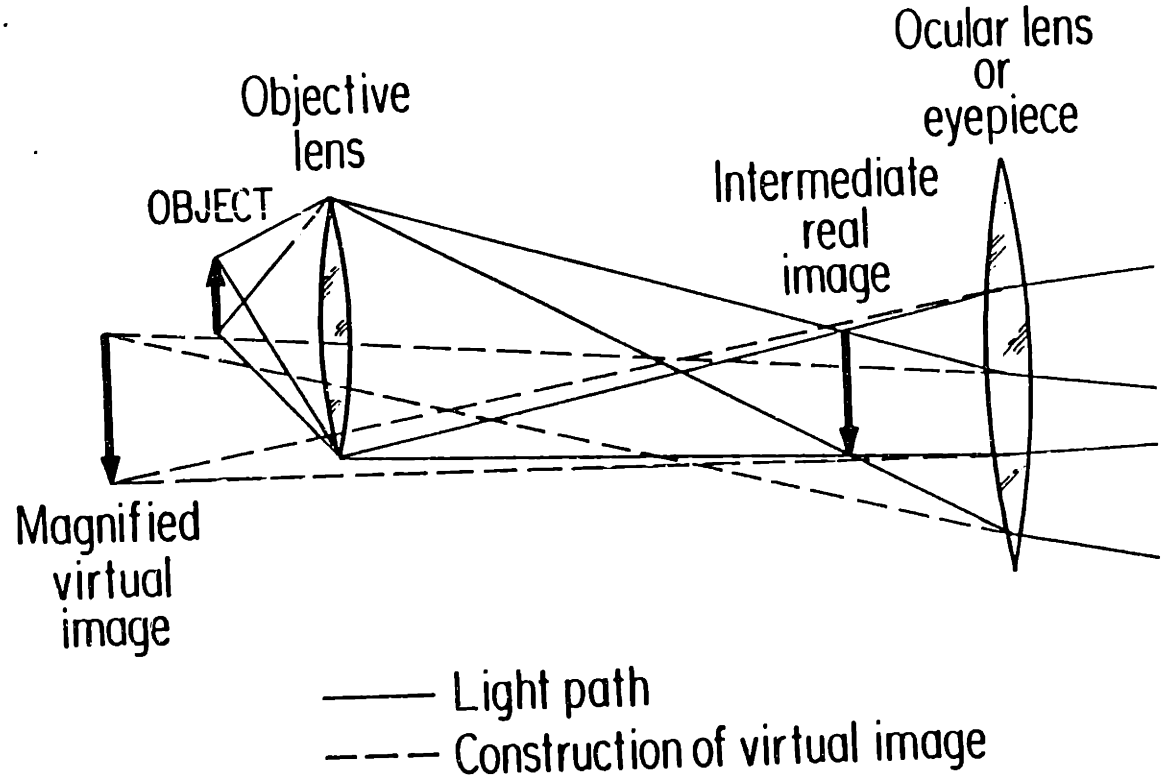

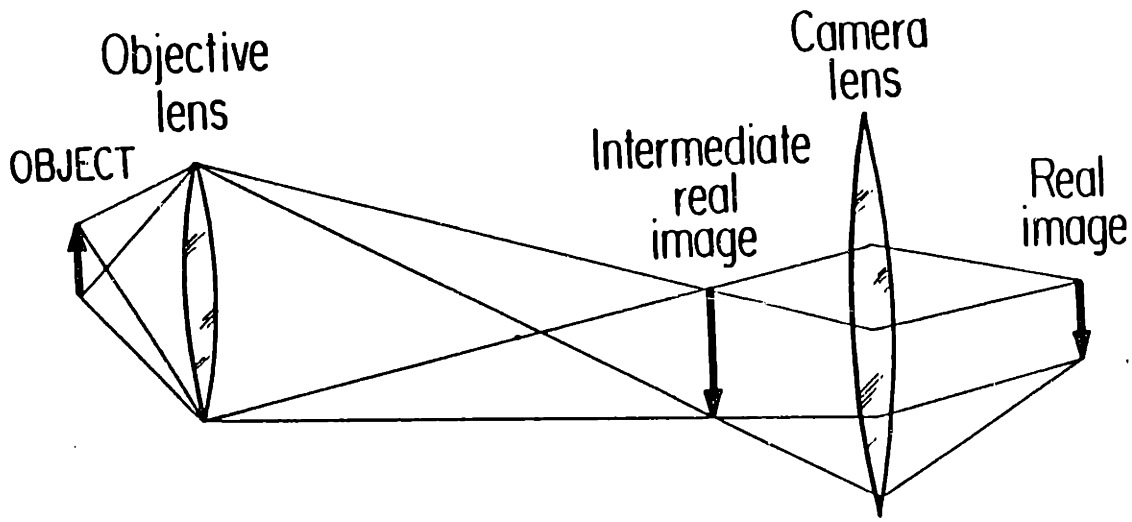

Figure 2.3 (a)Image formation in the use of eyepieces (Virtual Image) and (b) in the use of a photographic device (Real Image) in a microscope

intermediate image transferred into the eyepiece tube by a prism as shown in Figure 2.1). Below, I give some more details on the sample illumination in position A (contains the condenser lens) and in position B, respectively illumination from the bottom and from the top, on the pick-up objective lens and on the eyepieces. The microscope used in this work is an upright Nikon Optiphot. Some references that I found useful in the study of microscopy are [10-12].

In the illumination from the bottom the scattering angle θ between the incident beam direction and the scattered beam direction, is small. Therefore this position will also be referred to as the small angle configuration of the set-up. After coming out of the single mode fiber, the diverging beam is collimated by a first lens so that the expanded beam size is about 1 cm in diameter. The beam is then reflected vertically up onto the condenser lens by a prism which is attached to an X-Y-Z-translator. The condenser (Nikon Abbe 1.25) is used to focus the beam onto the sample. In order to avoid that the direct incident laser beam comes into the objective lens, the prism is placed below the edge of the condenser as shown in Figure 2.1.

The position of the condenser lens is of course crucial in MLLSS, because it determines the location of the focal spot in the small angle configuration. I will discuss the positioning of the condenser again in the section on the alignment of the MLLSS set-up. The correct position for MLLSS is, however, close to the one that is optimal for high resolution white light microscopy. It is thus advisable to place the condenser at this position before starting the alignment with the laser illumination. This position is called Kohler illumination. It is illustrated in Figure 2.4.

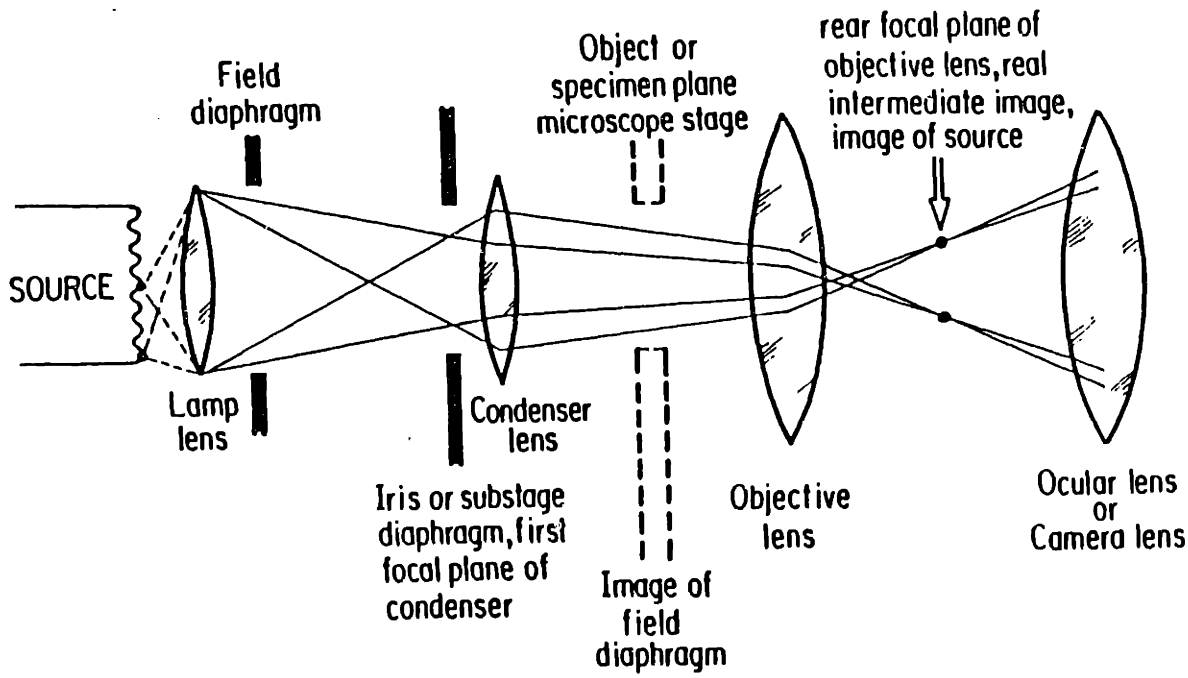

Figure 2.4 Positioning of the Condenser lens in Kohler Illumination

An image of the source is formed by the lamp lens at the first focal plane of the condenser and an image of the field diaphragm is formed in the specimen plane by the condenser. In this position the condenser collimates the light beam originating from the microscope lamp. In order to totally avoid direct laser light (not scattered) coming into the collection objective lens, the prism should be placed very close to the edge of the condenser. Thus the iris of the condenser should be left open. This is not the optimal setting for white light microscopy, because it does not give contrast to the image. Figure 2.5 illustrates this feature. The condenser is often closed somewhat when making photographs of the sample or simply inspecting it visually.

In the illumination from the top, the diverging beam coming out of the single mode fiber is collected by the focusing lens without first collimating the beam (the collimation is not necessary in this configuration since the beam does not have to travel a long distance before hitting the focusing lens). The focusing lens is a Leitz L20 0.32. It is held in position B (see Figure 2.1) and has X-Y-Z translational freedom. The arm on which it is mounted can also rotate about an axis in the plane of the sample. It is clear that the focal region formed by the objective lens in the large angle configuration is much nicer than the one formed by the edge of the condenser lens in the small angle configuration. A suggested improvement of the MLLSS set-up relates to this point in Chapter 6.

The focal spot diameter should be as small as possible in MLLSS experiments in order to avoid unwanted scattered light from parts of the biological cells that one is not interested in. When a parallel beam of

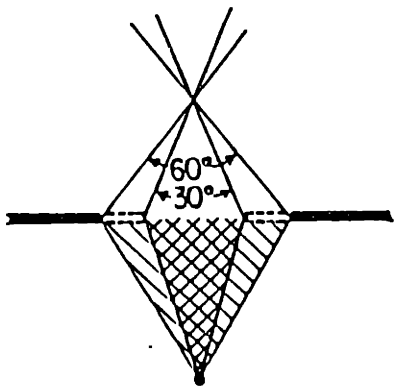

Background

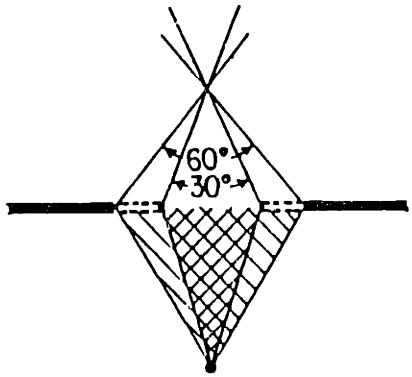

Specimen

Cone of 95% transmitted light (5% scattering)
" " 90% " " (10% scattering)

Cone of 90% transmitted light (10% scattering
" " 60% " " (40% scattering

Figure 2.5 Contrast enhancement by closing the iris aperture: for incident intensity I_o, a non-absorbing background and a 5% absorbing specimen, the collected light intensities are respectively I_B and I_S:

60° aperture $I_B = 0.95 \times I_o$
$I_S = 0.95 \times I_o \times 0.90 = 0.855 \times I_o$

30° aperture $I_B = 0.90 \times I_o$
$I_S = 0.95 \times I_o \times 0.60 = 0.570 \times I_o$

Thus contrast $100(I_b - I_s)/I_b$ at:

60° aperture is $100(0.95 - 0.85)/0.95 = 10\%$
30° aperture is $100(0.90 - 0.57)/0.90 = 37\%$

Closing the aperture enhances scattering differences, not absorption differences between background and specimen

diameter d is focussed by a lens of focal length f, the diameter s of the spot is given by

$$s = \frac{\lambda f}{d} \qquad 2.6$$

where λ is the wavelength of light. Both in the bottom and the top illumination, the laser beam diameter d, before hitting the focusing lens (condenser or objective lens) is expanded compared to the beam size at the exit of the laser. The maximum useful diameter d is the diameter of the lens that is used to focus the beam onto the sample. Obviously, this lens diameter is very different in both illuminations. The diameter of the beam when it hits the condenser lens, is chosen to be such that the spot size of the focal region is comparable in top and bottom illumination. In the large angle configuration, f ~ 8.6 mm and the available diameter of the lens is d ~ 6 mm. Thus the HeNe laser beam is focussed to a spot size s ~ 1.03 μm. In the small angle configuration, f ~ 15 mm (the working distance is only about 4 mm, the condenser is a very thick lens) and the diameter of the illuminated region is d ~ 10 mm. This yields a focal spot size diameter s ~ 1 μm. Both spot sizes are smaller than most biological cells.

With the focal spot smaller than the biological cells under study, the next important factor is the focal region of the collection optics. The intersection of the incident focal region and of the collection optics focal region, determines the scattering volume and it is this volume which has to be smaller than most cells. The scattered light is collected and focussed onto the entrance of the pick-up fiber by the objective lens. We use two objective lenses on the MLLSS set-up: a low magnification one (Nikon 4x 0.1) for rough alignment and a high

magnification one (long working distance Leitz L32 0.40) to perform MLLSS. The spatial resolution z of the latter lens should be smaller than most biological cells. It is given by

$$z = \frac{0.61\ \lambda}{NA} \qquad 2.7$$

where λ is 6328A in our case and NA is the numerical aperture of the objective lens (here NA=0.40). NA is defined as sin $\alpha/2$ where α is the angle subtended by the lens aperture d viewing a point in the specimen plane at object distance l:

$$NA = \sin\alpha \sim \frac{d}{2l} \qquad 2.8$$

High resolution corresponds to large NA because small z means small diameter of the focal region of the optical system, here the collection optics. Optimally, this focal region is a delta function $\delta(\vec{r})$ in the object plane. A delta function is the superposition of an infinite number of plane waves:

$$\delta(\vec{r}) = \int d\vec{k}\ e^{i\vec{k}\vec{r}}. \qquad 2.9$$

The larger the NA of a lens, the more wavevectors $\vec{k}$ are formed when a plane wave hits the lens and the sharper the focal point. Figure 2.6 shows a magnified image of the sample region. The light cones are drawn approximately on scale using the specifications of the particular lenses used in our MLLSS experiment. The figure is otherwise only an off scale sketch. It does not show the refraction of light. The focal spot size in the MLLSS set-up is about 2μm in diameter.

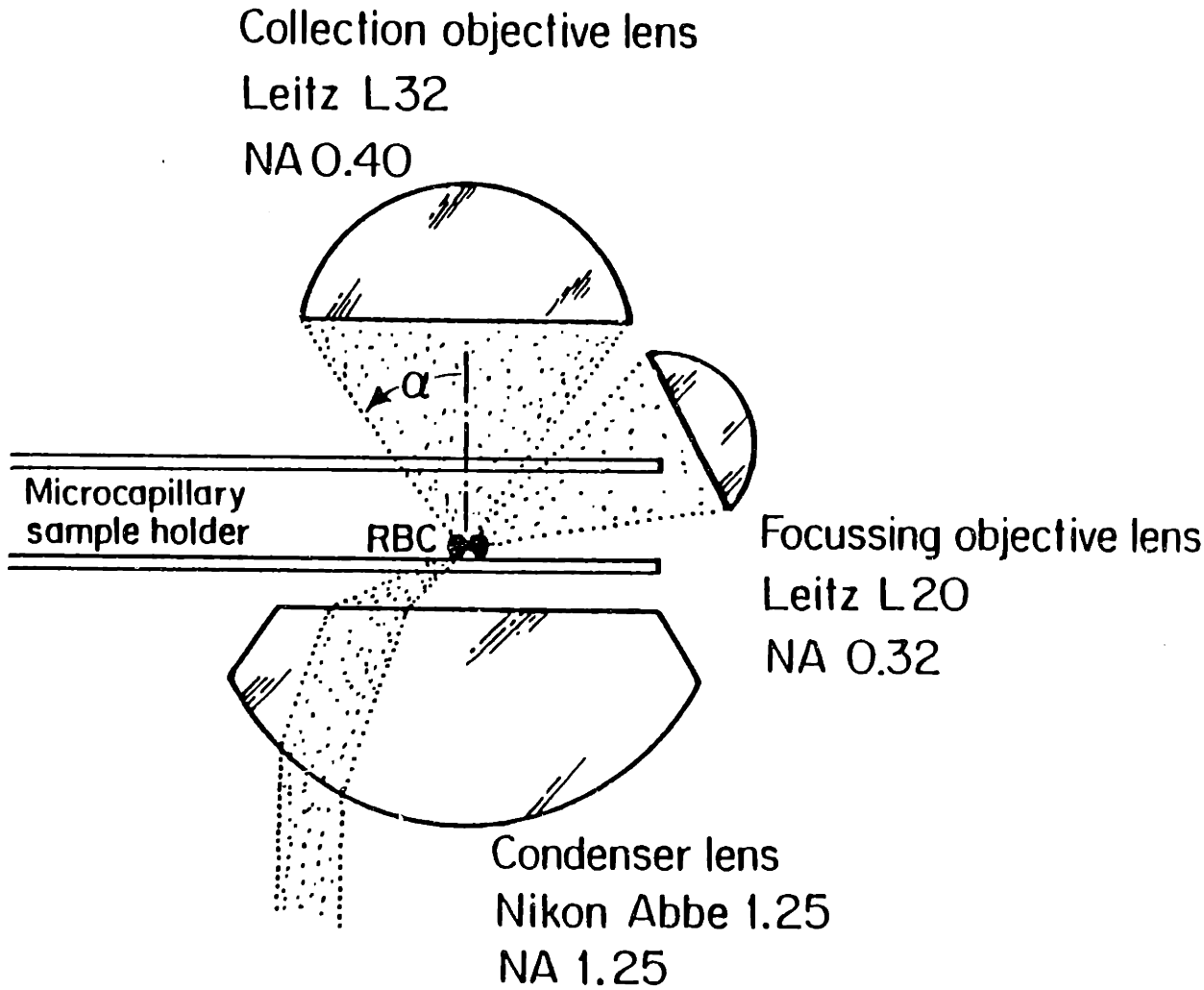

Figure 2.6 Central region of the MLLSS set-up showing the Sample, the Condenser and Objective lenses used for focussing the incident laser beam in respectively the small and large angle configuration, and the Objective lens used for collecting the scattered light

2.3.b. The Microscope Stage

The microscope stage was specially designed for the MLLSS experiments. The working distance of the lenses used to focus the incident beam, is small and thus it has to be possible to come very close to the cell under study. Figure 2.7 gives a sketch of the stage and the temperature control. Two slots are made in the stage: one for standard microscope slides and the other for a flow cell which was used in many experiments. Details on the sample holders are given in section 4.3. The stage is temperature controlled using a thermo electric device (TED). Because the sample itself is located rather far from the stage, temperature controlling the stage is not enough to temperature control the sample. Therefor, air channels flow through the stage and blow warm air onto the top and the bottom of the sample. The air is preheated by passing through a jar that contains heating wire. The current through the heating wire is turned on or off by a simple feed back switch (Thermistemp YSI Model 74) hooked up to a thermistor. The temperature is measured at the location of the sample by a thermistor attached to a digital temperature readout (Thermometer Keithley Model 866).

2.4 CHARACTERIZATION, CALIBRATION AND ALIGNMENT OF THE MLLSS SET-UP

2.4.a. Numerical Aperture and Polydispersity

In the analysis of light scattering data, it is essential to know the scattering vector $\vec{k}$. This vector is defined as the difference

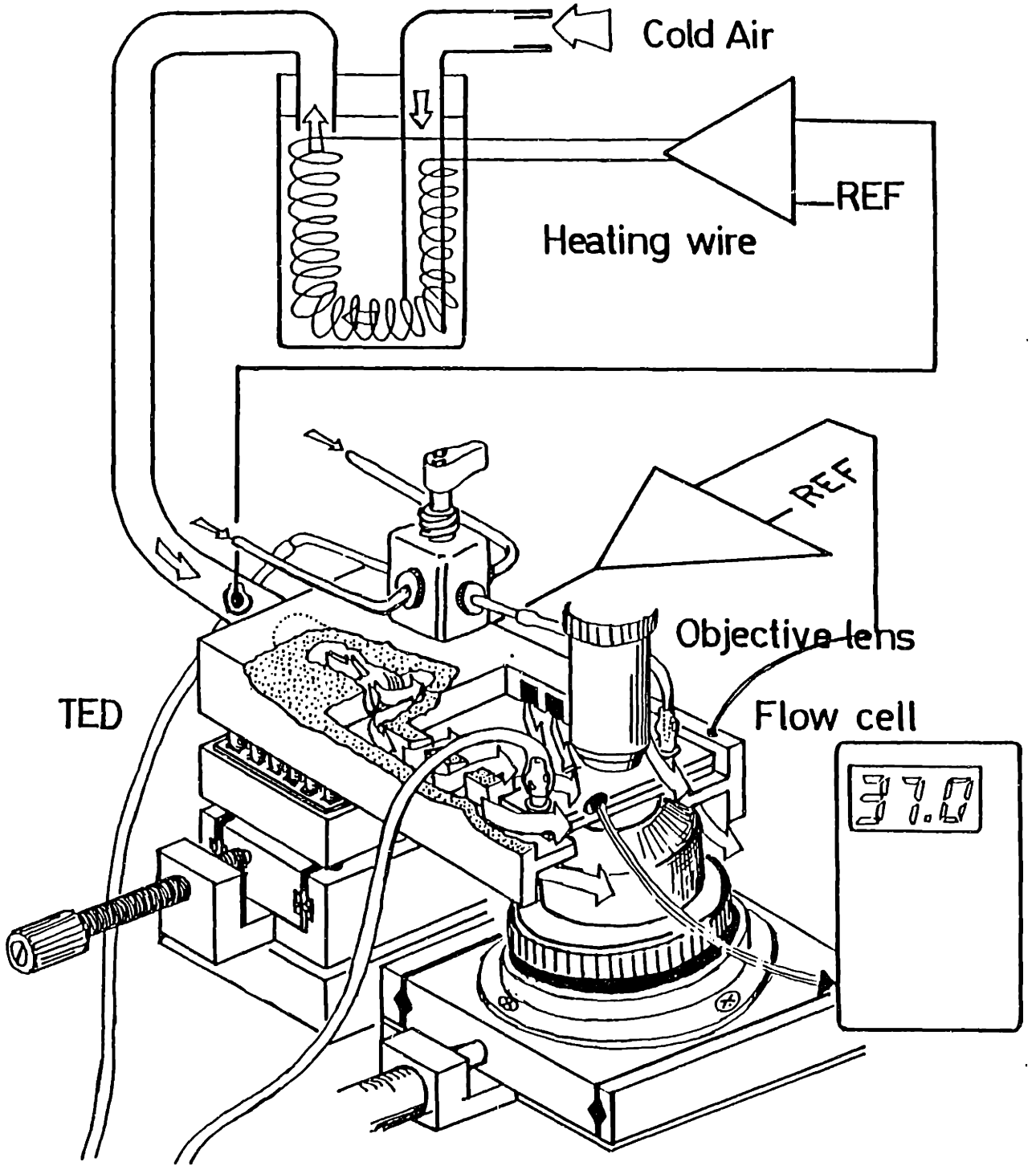

Figure 2.7 The microscope stage and its temperature control

between the incident and the scattered wavevectors $\vec{k}_i$ and $\vec{k}_s$. If θ is the angle between $\vec{k}_i$ and $\vec{k}_s$, the amplitude of the scattering vector is given by

$$|\vec{K}| = \frac{4\pi n}{\lambda}\sin\frac{\theta}{2} \qquad 2.10$$

where n is the refractive index of the suspension medium in which the scatterers move. The characteristic length at which the light scattering probes is $1/|\vec{K}|$. This means that the light scattered at an angle θ results from inhomogeneities in the dielectric constant on the scale of $1/|\vec{K}|$. These inhomogeneities could for example be particles with a diameter of approximately $1/|\vec{K}|$. An important quantity determined from the analysis of the intensity autocorrelation functions (see Eq.2.3), is the diffusion coefficient D of the scatterers. In order to extract D from the correlation functions, the scattering number $1/|\vec{K}|$ has to be known. It is clear that this number can be determined precisely only when the scattering angle θ is well defined. This is less so when lenses with a large NA are used. When light is scattered from a monodisperse sample of standard polystyrene spheres on a set-up with sharply defined scattering vector such as is the case in the conventional dynamic or quasi-elastic light scattering (QLS) experiments, the normalized intensity autocorrelation functions $c(\tau)$ are single exponential functions of time (see Eq.2.20 below):

$$\begin{aligned} c(\tau) &= A\, e^{-\tau/T} + B \\ &= A\, e^{-2Dk^2\tau} + B \end{aligned} \qquad 2.11$$

where $k=|\vec{K}|$, A is a constant and B is the baseline. In QLS, the NA of the lenses is smaller than in MLLSS and pinholes block off all but a

small central region of the lenses. If there is a large spread on the scattering number k, a distribution function P(k) has to be introduced and $c(\tau)$ is given by

$$c(\tau) = A\left(\int P(k) e^{-Dk^2\tau} dk \right)^2 + B. \qquad 2.12$$

Figure 2.8.a shows semi-logarithmic plots of the correlation function measured on the same monodisperse sample of polystyrene standard beads taken with conventional QLS and with microscope QLS or MLLSS. It is clear that the deviation from a single exponential is almost absent with conventional QLS and is appreciable with microscope QLS (MLLSS), both at small and large scattering angle. The next table gives the variance on the fitted value of the diffusion coefficient in both methods. The conventional QLS values are typical and the microscope QLS values are in excellent agreement with the spread on the scattering vector. Indeed, a NA of 0.40 corresponds to $\Delta\theta \approx 18°$ and thus $\Delta k^2 \approx 9 \times 10^9$ and a variance of 16% on the fitted diffusion coefficient.

angle	technique	variance	k^2	$\Delta k^2 / k^2$
small angle (~ 25°)	conventional QLS	5%	3.26×10^9	< 0.014
	microscope QLS (or MLLSS)	18%	''	0.707
large angle (~ 150 °)	conventional QLS	3%	6.50×10^{10}	< 0.001
	microscope QLS (or MLLSS)	14%	''	0.042

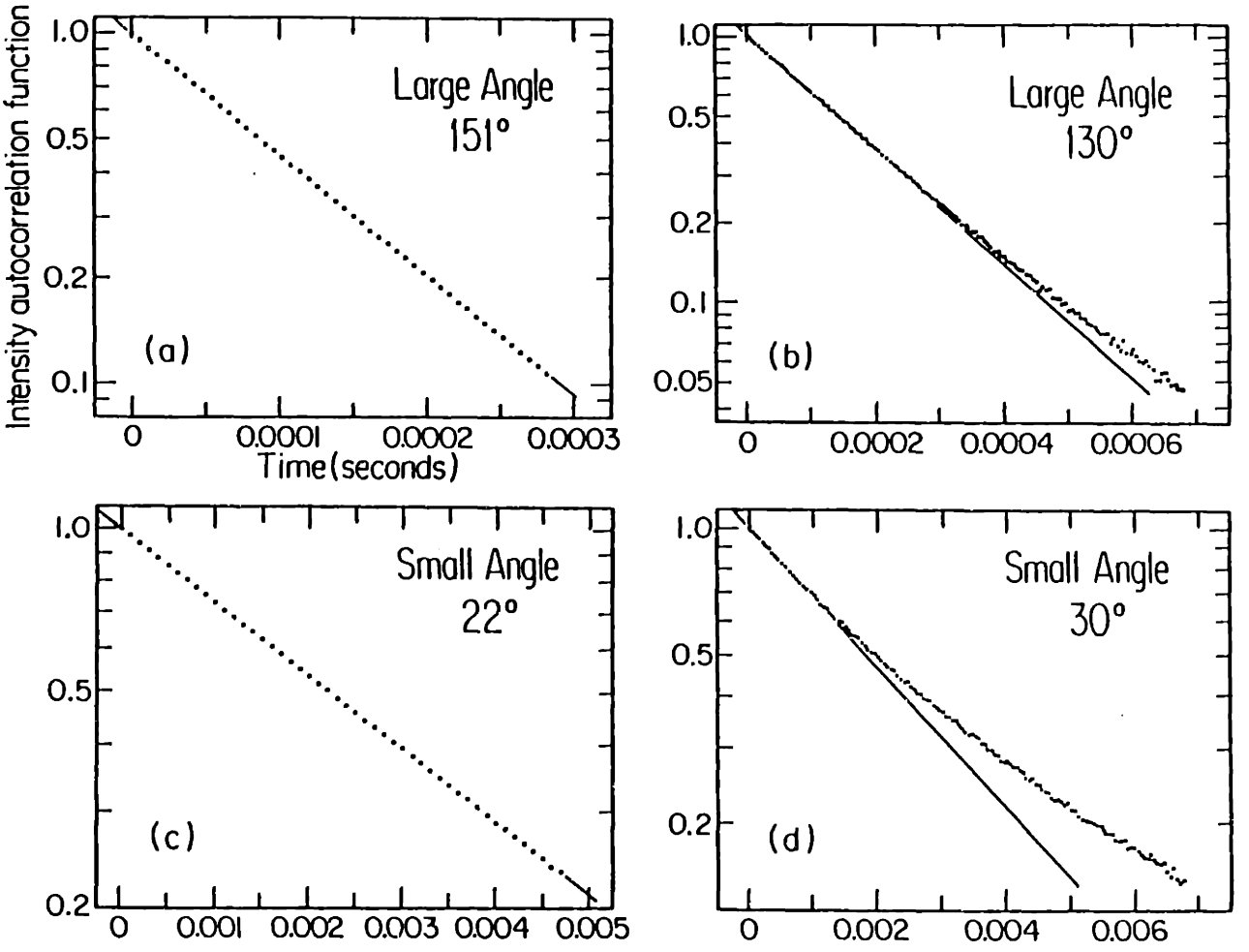

Figure 2.8 Apparent Polydispersity induced by the large Spread on Scattering Vectors in MLLSS: intensity autocorrelation functions taken at small and large scattering angle on identical polystyrene samples in MLLSS (microscope QLS) and conventional QLS

2.4.b. Scattering Angles: Calibration and Available Range

Standard polystyrene samples are used for calibrating the averaged scattering angles. After the set-up is aligned, correlation functions are collected from monodisperse samples of polystyrene beads. The functions are fitted to a single exponential and the characteristic decay time T is determined. An estimate θ_e for the scattering angle is used to extract a diffusion coefficient D_e. The scatterers radius a, in the non-interacting concentration range, is related to D by

$$D = \frac{k_B T}{6\pi\eta a} \qquad 2.13$$

where k_B is the Boltzman constant, T is the absolute temperature and η is the viscosity of the medium in which the particles move (water in the case of the standard polystyrene solutions). Using D_e yields an estimated radius a_e. The real scattering angle θ is then determined from

$$\frac{1}{a}\sin^2\frac{\theta}{2} = \frac{1}{a_e}\sin^2\frac{\theta_e}{2} \; . \qquad 2.14$$

The range of available angles is practically from 115° to 150° in the illumination from the top and from 27° to 33° in the illumination from the bottom. In position B they result from rotating the arm that holds the fiber (rotation axis in the plane of the sample) and from moving the X-Y-Z position of the fiber holder. In position A they result

from the X-Y-Z position of the prism and the condenser A (see Figure 2.1).

2.4.c. Coherence Areas

The scattered field, as was already pointed out earlier, is the superposition of the fields scattered from a large number of scatterers. A detector thus receives a total scattered field which fluctuates in time around an average value. I already discussed the necessity to have a temporally and spatially coherent incident beam. Here I discuss the spatial coherence of the scattered field. At one point in time, different positions on the detector surface receive scattered fields that have a different phase because the optical path difference between different points in the scattering volume and different positions on the detector surface varies. The finite extend of the scattering volume thus causes non-coherent illumination of a large area of the detector. However, when two points on the detector surface are sufficiently close together, the received scattered fields are almost in phase (and identical when the two points coincide). The area over which the total scattered field remains coherent is called the coherence area. Obviously, this area is a function of the distance R between the scattering volume and the detector. For a scattering volume of width a and detected length L at the scattering angle $\theta=90°$, the coherence area at scattering angle θ and at a distance R from the scattering volume is derived in Appendix II-2 and is given by

$$A_{coh} = \frac{\lambda^2 R^2}{a(L\sin\theta + a|\cos\theta|)} \qquad 2.15$$

$$= \Omega_{coh} R^2$$

where Ω_{coh} is the coherence solid angle. Figure 2.9 shows clearly the meaning of a coherence area and it demonstrates how the ratio of the wavelength of light to the linear dimensions of the scattering volume affects the coherence solid angle. The pictures are the superposition of the circular wavefronts radiated by two scattering centers (scatterers). Figure 2.9 illustrates the influence of the separation between the two scatterers on the coherence angle of the scattered light (angular width between successive intensity minima). The number of coherence areas in the area of the detector is essential for the signal to noise ratio of all QLS experiments. Optimally, the detector area should be one coherence area (case N=1 in Eq.2.19 below).

The large difference in coherence solid angle may constitute the most important difference between conventional and microscope QLS. In conventional QLS, the scattering volume dimensions L and a are typically 0.1 mm. In MLLSS, they are approximately 1 μm as was calculated in the section on focal spot size and resolution. The resulting coherence solid angle for He-Ne laser illumination for conventional and microscope QLS are given in the table below. Thus, in order to collect one coherence solid angle, conventional QLS can work with very narrowly determined scattering angles (using pinholes and small NA lenses). In MLLSS, however, one has to collect at least 17° á 18° of spread on the scattering angle. In practice, one usually collects the scattered signal over a few coherence areas, because one then has more signal and the statistical noise level thus decreases faster. The objective lens used to collect the scattered light in MLLSS has a NA of 0.40 which corresponds to

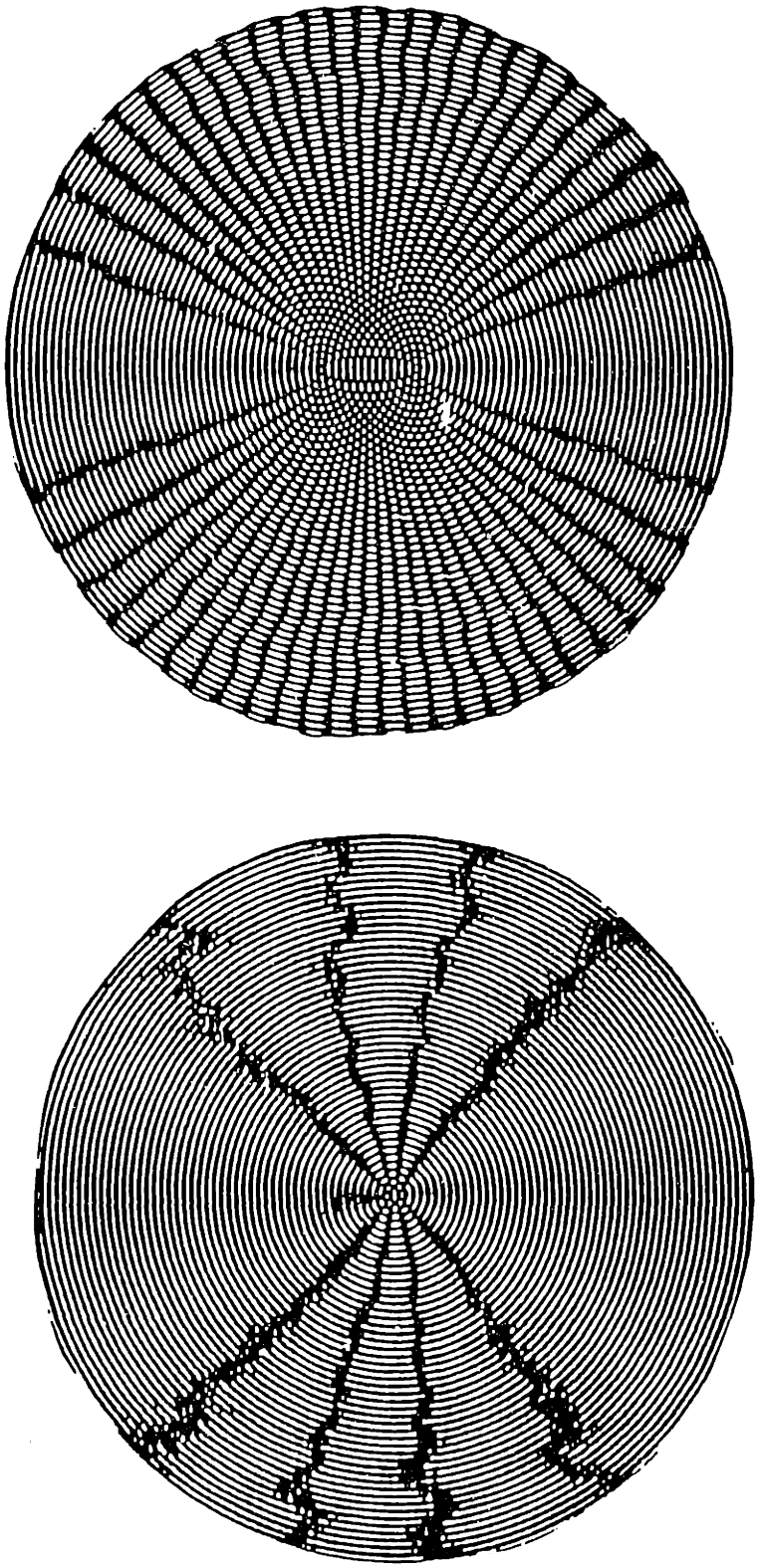

Figure 2.9 Illustration of the influence of the Scattering Volume on the Size of Coherence Areas. In the top illustration, the maximum separation between scatterers is about 12 wavelengths which is much less than in conventional QLS where the scattering volume is about 200 wavelengths in linear dimension. In the bottom illustration, the maximum separation between scatterers is on the order of 5 wavelengths of the incident light which corresponds to the situation in MLLSS.

	conventional QLS L≈a≈0.1mm	microscope QLS L≈a≈1μm
scattering angle	coherence solid angle Ω_{coh}	
30°	2.93×10^{-5}	0.293
130°	2.84×10^{-5}	0.284

47.2° of spread on the scattering angle and thus to a collection solid angle of 2.014. The MLLSS set-up thus collects typically 6 7 coherence solid angles. The collection objective lens has a built in diaphragm. Though closing it could reduce the collected cone of light to one Ω_{coh}, this would too much reduce the resolution of the system. Instead, choosing different diameter optical fibers embedded in the eyepiece, can decrease the number of collected coherence areas. The diameter of the pick-up optical fiber located at the real intermediate image is 50 μm, 150 μm or 450 μm (Gamma Scientific eyepieces models 700-10-36A, -37A and -34A). The one we used for MLLSS is the 50 μm one, which corresponds to a roughly 1.25 μm diameter region in the object or sample plane. In other words, it covers the image of the focal region. The 450 μm diameter optical pick-up fiber covers even the largest of red blood cells and is used for absorption spectrometry (see Chapter 3).

The distance R between the sample and the collection objective is exactly the object length l used in Eq.2.8 and is approximately 6.6 mm. The coherence area is thus about 1.26×10^7 μm^2 at the entrance of the collection objective.

2.4.d. Alignment of the MLLSS set-up

I will go through the alignment procedure of the MLLSS set-up in a step-by-step fashion. It is obvious that not all of these steps need to be repeated every time one does an experiment. The alignment is performed in the order in which I present it here only rarely, namely when some drastic changes were made to the set-up so that the alignment was completely lost. For the daily fine adjustments, one typically goes through the alignment procedure in reverse order.

Step one is to introduce the laser beam into the single mode fiber so that the laser beam at the exit is a nice single mode spot (see Figure 2.2.b). Both ends of the fiber should be as smooth as possible (this is controlled by the breaking of the fiber, it requires some experience and inspection of the fracture under a dissection microscope) and the cladding should not obstruct the core. The working distance of the objective lens that focuses the laser beam onto the entrance of the fiber is very short. The fiber holder is itself held in a special fiber positioner (NRC model FP-1) of which the three screws should be moved around till the laser beam at the exit of the fiber has a nice single Gaussian intensity profile. The cylinder that holds the exit end of the fiber is positioned as shown in Figure 2.1 (close to the focusing lens

in large angle configuration and to the collimating lens in the small angle configuration).

The next step is to focus the incident beam. For this purpose a microcapillary is filled with a solution of standard polystyrene beads (as used for calibrating the scattering angles). The capillary is placed in the approximately correct position using regular white light microscopy. In the large angle illumination, the arm that positions the fiber holding cylinder, is first placed at approximately the desired angle. The exact location of the cylinder is found by moving the X-Y-Z-translator on which the axis, about which the arm rotates, is mounted. This is done using the low magnification objective lens at first and afterwards the 32x objective used for MLLSS. The path of the laser beam through the polystyrene is distinguished from possible stray light because the Brownian motion of the polystyrene is clearly visible in the laser path. The Z-position of the stage-condenser-unit usually needs some adjustment (the focusing screw of the microscope). When the alignment is completed, the focal region of the laser should look like in Figure 2.10.a. It corresponds to the situation shown in Figure 2.10.b. The focal point is placed at the tip of the pick-up optical fiber, which is clearly seen in the field of the eyepiece, by moving the X-Y-position of the condenser.

In the small angle configuration, the alignment procedure is appreciably more complicated. The stand that holds the collimating lens and the fiber holding cylinder, should be parallel to the plane of the condenser lens and should have its axis in a plane that extends vertically below the center of the condenser. The prism should be placed with its

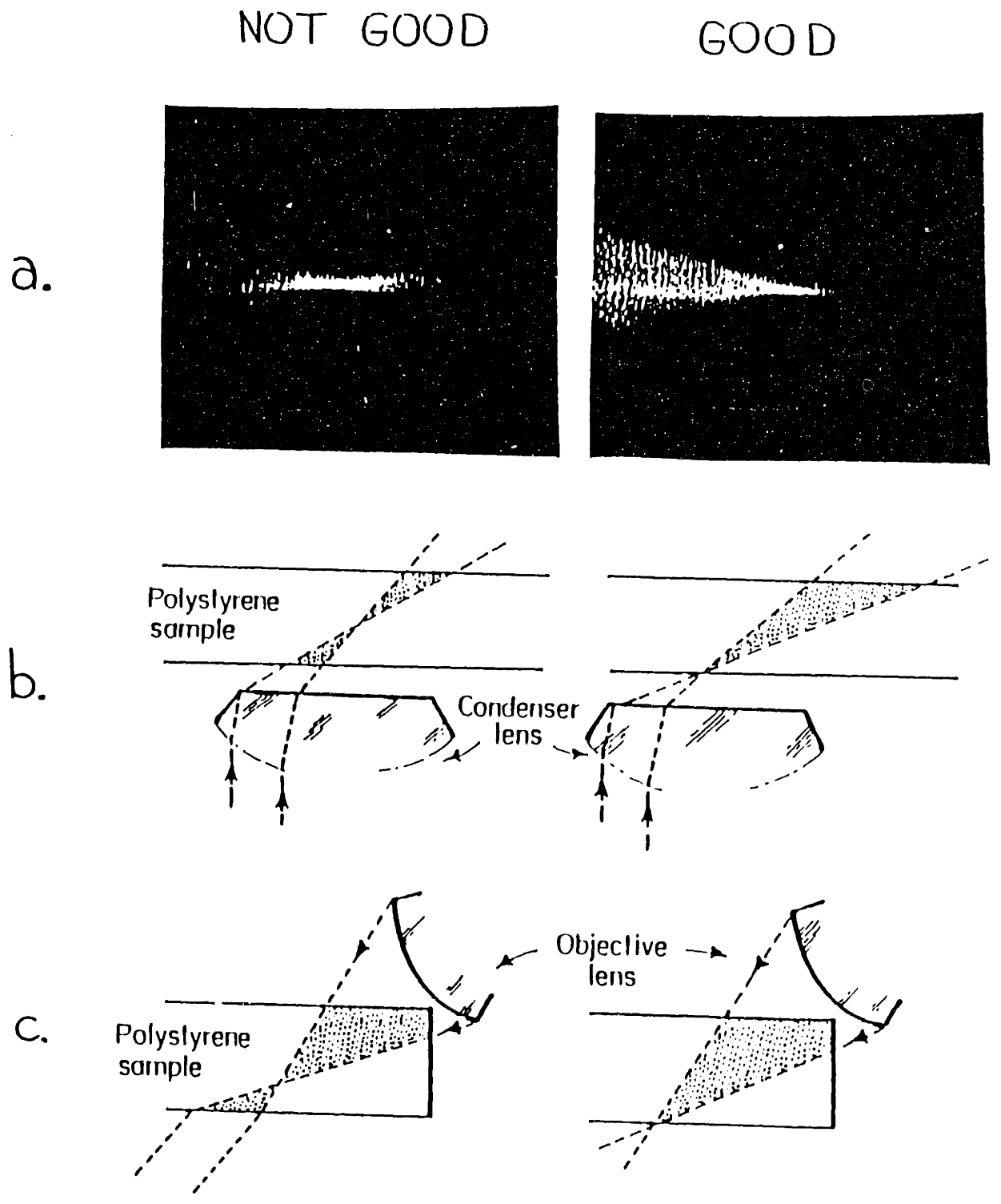

Figure 2.10 (a)Image of the laser focal region in a polystyrene sample and explanation of the image in (b)illumination from the bottom and (c)from the top

top surface as horizontal as possible. The X-Y-Z-translator positioning the prism has one of its horizontal axis perpendicular to the collimated laser beam. That axis and the vertical axis are adjusted so that the laser beam is centered on the prism. The axis parallel to the laser beam is left unadjusted up to this point. It should place the prism below the edge of the condenser, which is centered underneath the collection objective lens. At this point, the path of the laser beam through the polystyrene should be visible at low magnification. The condenser lens, is moved so that the focal point of the beam is coincident with the tip of the pick-up fiber. Next, one switches to the high magnification objective. The Z-positioning of the condenser and of the stage-condenser-unit should be adjusted so that the focal region of the laser beam is in focus and looks like in Figure 2.10.a. The situation is then as shown in Figure 2.10.c. During the alignment procedure, it should never be forgotten that one sees the mirror image of the sample.

2.5 MLLSS ON SINGLE BIOLOGICAL CELLS

2.5.a. Alignment of the MLLSS set-up on a cell

The cells under study should always be suspended in a buffer that keeps the cells metabolically alive and that is clear for light scattering purposes. If possible, molecules that are large enough to scatter light, should be avoided in the buffer. The cells on which most MLLSS was done are red blood cells. The preparation of these cells is discussed in Chapter 4. One of the components in the buffer is bovine serum albumin (BSA) which does scatter light. It is important to keep

the concentration of such molecules in the suspension buffer as low as possible. In the case of biconcave red blood cells the set-up can be sufficiently well aligned so that scattering from the buffer can be avoided. In the case of experiments on other types of cells, this may not be the case and particular attention should be paid to the scattering properties of the suspension medium.

The reason why the alignment is easier on red blood cells than on most other biological cells lies in the smoothness of their membrane. Indeed, the biconcave red blood cell surface is very smooth. Therefore, it is easy to recognize the places where the laser beam goes in and out of the cell. This is illustrated in Figure 2.11. When red blood cells are moved into the laser beam which is well aligned on a polystyrene sample, usually only one fine adjustments needs to be made: the focal position of the cell. The stage-condenser unit should be moved in the Z-direction till the two laser spots (they appear as lines) on opposite sides of the cell, are focussed. Occasionally, the condenser has to be moved a very tiny bit in the horizontal direction.

When doing MLLSS on less smooth cells, the fine tuning of the alignment once the cells are placed in the focal region of the laser, is almost impossible. The more irregular cells tend to appear as cities at night: they are covered with small bright spots. These result from the laser beam reflecting of irregularities on the cell surface. It is therefore very important to place a microcapillary filled with polystyrene as close as possible to the microcapillary that contains the cells. In this fashion one can switch from the one sample to the other without having to move the stage over a large distance. This minimizes

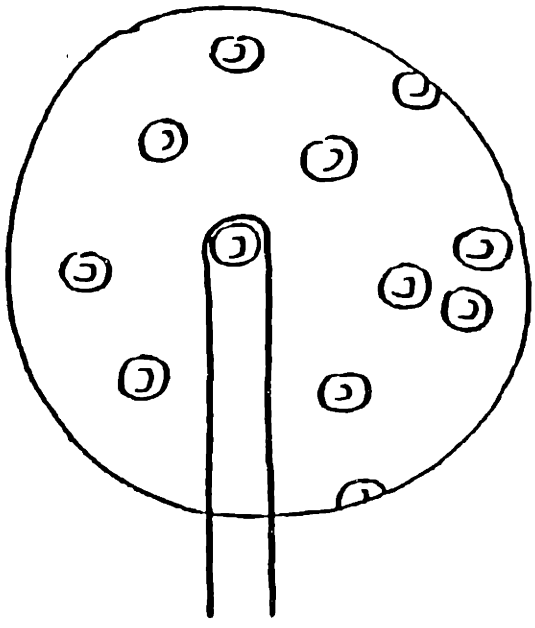

450 μm pick-up fiber

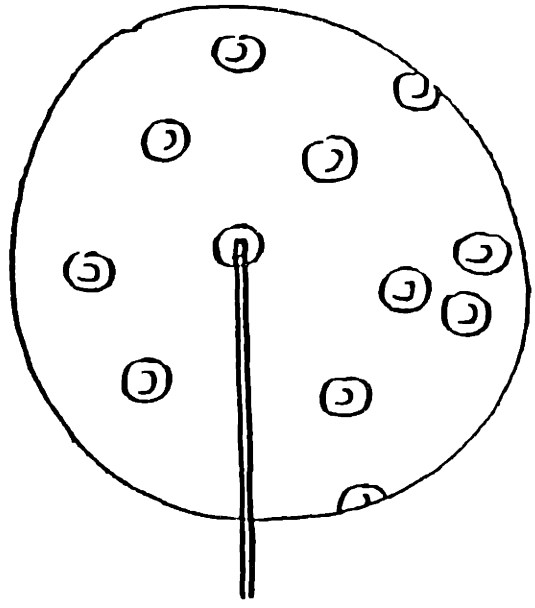

50 μm pick-up fiber

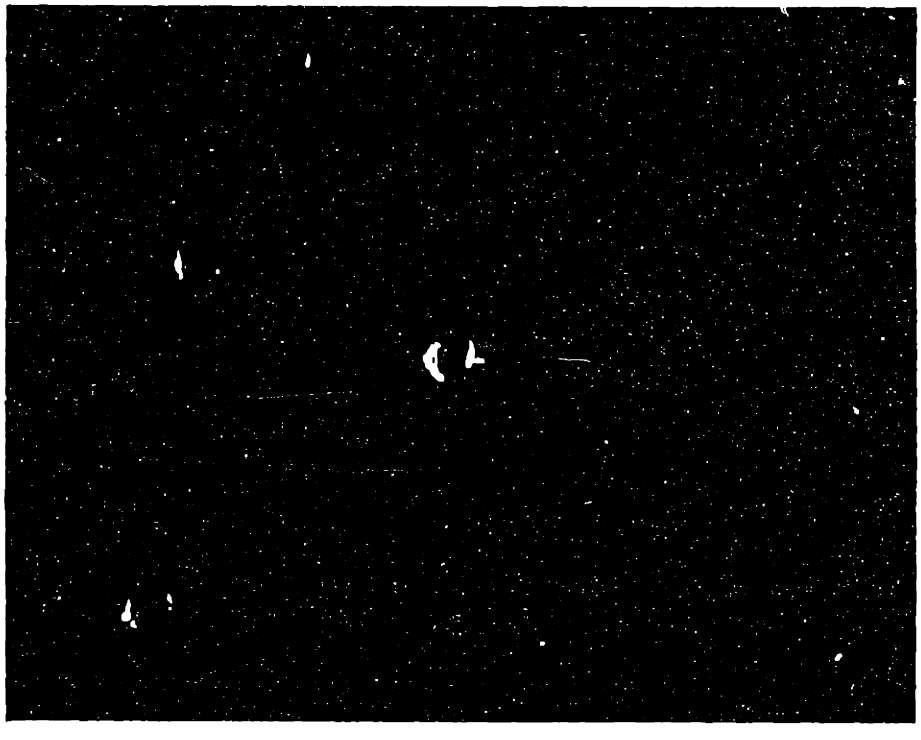

Figure 2.11 (a)Sketch of red blood cells (RBCs) in the field of view of the microscope with two sizes optical fiber embedded in the eyepiece and (b) RBCs under laser illumination through the condenser lens

the loss of alignment in the process of placing the cell in the focussed laser beam.

2.5.b. Analysis of the Intensity Autocorrelation Functions

- The intensity autocorrelation function $c_I(\tau)$ was defined in Eq.2.3. It was pointed out that one works with the correlation functions normalized with their initial value. Yet, before turning to the analysis of these normalized functions, I will discuss the full intensity autocorrelation function $c_I(\tau)$.

The electric field $\vec{E}_s$ scattered from biological cells can always be written as a superposition of the field scattered from moving parts, $\vec{E}_m$, and the field scattered from immobile parts, $\vec{E}_{imm}$:

$$\vec{E}_s = \vec{E}_m(t) + \vec{E}_{imm}(t) \qquad 2.16$$

If I_m and I_{imm} are respectively the average scattered intensity from mobile and immobile scatterers defined as

$$I_m = \langle \vec{E}_m(t) \cdot \vec{E}_m^*(t) \rangle_t \qquad 2.17$$
$$I_{imm} = \langle \vec{E}_{imm} \cdot \vec{E}_{imm}^* \rangle_t$$

and if $g(\tau)$ is the normalized electric field autocorrelation function for mobile scatterers

$$g(\tau) = \frac{\langle \vec{E}_m(t) \cdot \vec{E}_m^*(t+\tau) \rangle_t}{\langle \vec{E}_m(t) \cdot \vec{E}_m^*(t) \rangle_t} , \qquad 2.18$$

then (see Appendix II-3) the intensity autocorrelation function is given

by [13,14]

$$c_I(\tau) = (I_m + I_{imm})^2 + A\,(g(\tau)^2\, I_m^{\,2} + 2\, g(\tau)\, I_m\, I_{imm}) \qquad 2.19$$

where A is an instrumental constant (A=1/(1+N) where N is the number of coherence areas in the detector surface). For particles exhibiting Brownian motion with diffusion coefficient D, the field autocorrelation function is given by [15] (see Appendix II-4)

$$g(\tau) = e^{-Dk^2\tau} \qquad 2.20$$

where k is the length of the scattering vector. As already pointed out, one usually works with the normalized intensity autocorrelation function $c_N(\tau)$ from which I will drop the subscript in the future:

$$c_N(\tau) = c(\tau) = \frac{c_I(\tau)-c_I(\infty)}{A\,(c_I(o)-c_I(\infty))} \qquad 2.21$$

I wish to discuss a few features and special cases of $c(\tau)$.

- Two special cases of Eq.2.19 correspond to so called <u>homodyne scattering</u> and <u>heterodyne scattering</u>. In the homodyne case, most of the scattered light originates from the moving scatterers: $I_m >> I_{imm}$. In the heterodyne case, most of the scattered light originates from immobile scatterers such as the cell wall or very large structures rigidly kept in place inside the cell: $I_{imm} >> I_m$. The difference lies in the initial slope of $c(\tau)$:

$$\left.\frac{dc(\tau)}{d\tau}\right|_{\tau=0} = \frac{d}{d\tau}\left[\frac{I_m^{\,2}g^2(\tau) + 2I_mI_{imm}g(\tau)}{A\,(I_m^{\,2} + 2I_mI_{imm})}\right]\Bigg|_{\tau=0} \qquad 2.22$$

$$= 2 \frac{I_m + I_{imm}}{I_m + 2I_{imm}} \frac{dg(tau)}{d\tau}\Big|_{\tau=0}$$

Thus one finds that the initial slope of $c(\tau)$ for homodyne scattering is twice the one for heterodyne scattering. Using Eq.2.20, one finds

$$\frac{dc(\tau)}{d\tau}\Big|_{\tau=0} = -2 D k^2 \qquad \text{homodyne scattering } I_m >> I_{imm} \qquad 2.23$$

$$\frac{dc(\tau)}{d\tau}\Big|_{\tau=0} = -D k^2 \qquad \text{heterodyne scattering } I_m << I_{imm}$$

- The difference between homodyne and heterodyne scattering becomes particularly important in the determination of the diffusion coefficient D of mobile scatterers. In the purely homodyne case, D is correctly extracted from $c(\tau)$ using

$$D = -\frac{1}{2c(\tau=0)k^2} \frac{dc(\tau)}{d\tau}\Big|_{\tau=0} \qquad 2.24$$

Often, the computer programs that perform the fitting of the experimentally obtained intensity autocorrelation functions to the formal expression for $c(\tau)$, extract D using Eq.2.24. Application of this equation to $c(\tau)$ as given in Eq.2.21 in general, however, yields a fitted value D_f which is not the correct diffusion coefficient D of the mobile scatterers. Indeed,

$$D_f = \frac{I_m + I_{imm}}{I_m + 2I_{imm}} D \qquad 2.25$$

$$= D \qquad \text{for the homodyne case}$$

$$= \frac{D}{2} \qquad \text{for the heterodyne case}$$

In the next chapters, I will always point out which definition was used for reported diffusion coefficients.

- In MLLSS one works with a large spread P(k) on the scattering vector $\vec{k}$ as was pointed out in section 2.4.a. In that section, a very simple intensity autocorrelation function was considered: $c(\tau)$ for $I_{imm}=0$. Eq.2.12 gives that correlation function corrected for the existence of a distribution P(k) of scattering numbers. Figure 2.8 illustrated the effect of a broad P(k). It is simple to introduce P(k) in the more general form for $c(\tau)$ given in Eq.2.21 by modifying Eq.2.20 to

$$g(\tau) = \int dk\ P(k)\ e^{-Dk^2\tau} \qquad 2.26$$

Though all required variables are known to determine P(k) in our MLLSS experiment, I have not corrected for the existence of a significant P(k) in my experiments. In experiments in which one would be interested in the absolute quantitative value of diffusion coefficients, P(k) would need to be worked into the analysis. In my case, however, the emphasis was always on values of D relative to one another so that neglecting P(k) did not affect the results.

- Analogously to the possible spread in k values discussed in the previous paragraph, it is possible and in fact usual for there to be a distribution function G(D) of diffusion coefficients. If this is the case, Eq.2.20 should be replaced by

$$g(\tau) = \int dD\ G(D)\ e^{-Dk^2\tau} \qquad 2.27$$

In particular, G(D) can be a double peaked function with a delta peak at $D=D_1$ and one at $D=D_2$, namely $G(D) = A_1\delta(D_1) + A_2\delta(D_2)$. In this case, the normalized intensity autocorrelation function $c(\tau)$ is given by

$$c(\tau) = \frac{I_m(A_1e^{-D_1k^2\tau}+A_2e^{-D_2k^2\tau})^2 + 2I_{imm}(A_1e^{-D_1k^2\tau}+A_2e^{-D_2k^2\tau})}{I_m + 2I_{imm}} \qquad 2.28$$

$$= (\ A_1e^{-D_1k^2\tau} + A_2e^{-D_2k^2\tau}\ )^2 \qquad \text{for } I_{imm}=0$$

This form is commonly used when the normalized homodyne correlation functions have a clear non-single exponential character and the system under study is suspected to be composed of two particle sizes.

- I wish to comment on the <u>absolute scattered intensities</u> I_m <u>and</u> I_{imm}. In principle, three independent quantities can be extracted from $c(\tau)$: I_m, I_{imm} and D (from $g(\tau)$). Yet, changes in the experimental conditions throughout the experiments make it almost impossible at this stage to compare the absolute scattered intensity recorded at different times in the experiment. One important change lies in the optical alignment which is altered slightly when a cell is moved into the scattering volume. This is of course only a problem when more than one cell is monitored so that one has to move the stage as one observes one cell after the other. Another change in experimental conditions is related to the high voltage across the PMT. We operate the PMT anywhere between 1500V and 1700V depending on the brightness of the scattered light. This has mostly been an issue in the study of sickled red blood

cells. Their shape is very irregular and it is sometimes unavoidable to collect light from bright reflections on the cell surface. Rather than to scale the autocorrelator by a very large number, we then decrease the PMT voltage. The sensitivity of the PMT changes as shown in Figure 2.12. This curve can be used to normalize the scattered intensity measurements at all PMT voltages so that this is not a problem. The absolute scattered intensity is then computed using

$$I_T = \left(\frac{c(\infty) \text{ x scale ratio}}{\Delta T \text{ x time on}} \right)^{1/2} \qquad 2.29$$

and scaling to the PMT sensitivity at one chosen voltage. Here the baseline $c(\infty)$, sometimes called the calculated baseline, is given by

$$c(\tau=\infty) = n \times n_s \times \frac{\Delta T}{\text{time on}} \qquad 2.30$$

and n and n_s are the total number of respectively unscaled and scaled counts, ΔT is the clocktime and "time on" is the total time during which the intensity autocorrelation function is accumulated. The most important change in experimental conditions is in the scattering volume in experiments in which the cells drastically change shape under variable conditions. This is certainly the case in experiments on sickle cell anemia red blood cells as they change between the sickled and the biconcave shape (see Chapter 4). Therefore, the absolute scattered intensities are not usually presented. Instead, the relative intensity of the mobile scatterers was often used:

$$R = \frac{I_m}{I_m + I_{imm}} \qquad 2.31$$

In contrast with the absolute value of the scattered intensities, the ratio R of intensities is relatively insensitive to scattering volume

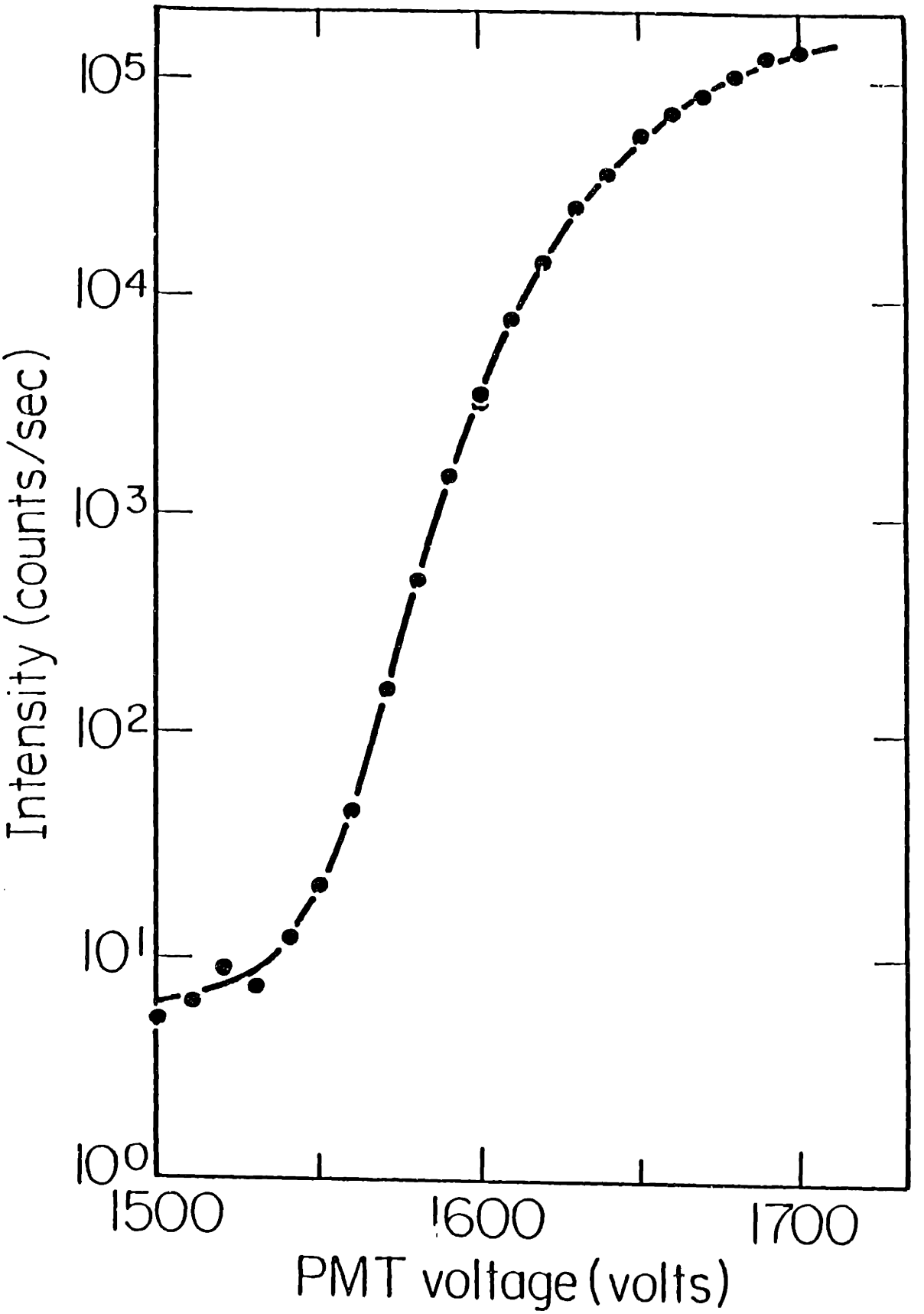

Figure 2.12 Measured intensity (counts/second) by our photo multiplier tube (PMT) as a function of PMT voltage taken on one polystyrene sample at one illuminating laser intensity and using the 50 μm optical fiber

and alignment changes, because these factors affect the numerator and denominator in the same way.

One feature of the absolute scattered intensity, however, is worth mentioning. It is particularly important in polymerizing systems. The scattered intensity corresponding to an n-mer, I_n, depends strongly on both n and the scattering angle. The scattering angle dependence is itself a function of the dimensions of the scatterers and thus of their diffusion coefficient. This is expressed in the form factor f(k,D). The n dependence is quadratic and as a result the total scattering intensity from a solution of aggregates is proportional to the weight averaged aggregation size $\bar{n}_W$. One obtains:

$$g(\tau) = \frac{\sum_{n=1}^{N} P_n I_n \exp(-D_n k^2 \tau)}{\sum_{n=1}^{N} P_n I_n} \qquad 2.32$$

$$I(k) = \sum_{n=1}^{\infty} f(k,D_n) P_n I_n \propto \sum_{n=1}^{\infty} n^2 P_n \propto \frac{\sum_{n=1}^{\infty} n^2 P_n}{\sum_{n=1}^{\infty} n P_n} = \bar{n}_W \qquad 2.33$$

where P_n is the number of n-mers and D_n is the diffusion coefficient of an n-mer. The quantity $\sum_{n=1}^{\infty} nP_n$ gives the total number of monomers and is a constant for a given concentration. From the above equation it is clear that the scattered light intensity usually increases with polymerization and decreases with depolymerization.

- Finally, I will briefly talk about the signal to background ratio or AC to DC ratio. They are computed from the value of $c(\tau)$ at $\tau=0$ and at the calculated baseline $c(\infty)$ (see Eq.2.30) and the delayed baseline. The delayed baseline is a feature on most correlators. It measures the value of $c(\tau)$ at a position far from the decaying part between $\tau=0$ and $\tau=N\Delta T$ (N = number of channels in the correlator). In our case, the delayed baseline is at $1024 \times \Delta T$. The AC/DC levels are given by

$$AC/DC_{delayed} = \frac{c(\tau=0) - c(\tau=1024 \times \Delta T)}{c(\tau=1024 \times \Delta T)} \qquad 2.34$$

$$AC/DC_{calculated} = \frac{c(\tau=0) - c(\tau=\infty)}{c(\tau=\infty)} \; . \qquad 2.35$$

The delayed AC/DC ratio records all fluctuations on time scales no longer than $1024 \times \Delta T$ and the calculated AC/DC ratio, all fluctuations on time scales no longer than the accumulation time of the experiment (time on). The $AC/DC_{delayed}$ is thus always smaller than the $AC/DC_{calculated}$ because the calculated baseline $c(\infty)$ is always larger than $c(1024\Delta T)$ (see for example Figure 4.8).

REFERENCES

[1] G.B. Benedek; Polarization, matter and radiation; Presses Universitaires de France, Paris, 1969

[2] B. Chu; Laser light scattering; Academic Press, New York, 1974

[3] H. Cummins and E. Pike; Photon correlation and light beating spectroscopy; Plenum Press, New York, 1974

[4] I. Nishio et al.; Hemoblobin aggregation in single red blood cells of sickle cell anemia; Science 220 , 1173-1175, 1983

[5] T. Maeda et al.; Quasielastic light scattering under optical microscope; Rev.Sci.Instrum. 43 , 566-567, 1978

[6] M. Coletta et al.; Kinetics of sickle hemoglobin polymerization in single red cells; Nature 300 , 1982

[7] R. Mustacich et al.;.....; Rev.Sci.Instrum. 47 , 108-111, 1976

[8] S. Newton et al.; Laser light-scattering analysis of protoplasmic streaming in the slime mold physarum polycephalum; Biochim. Biophys.Acta 496 , 212-224, 1977

[9] M. Young; Optics and lasers; Springer-Verlag, Berlin, 1984

[10] R. Barer; Lecture notes on the use of the microscope; Blackwell & Davis Publ.Comp., Philadelphia, 1959

[11] L.C. Martin; The theory of the microscope; Blackie Press, Glasgow, 1966

[12] E.M. Slayter; Optical methods in biology; John Wiley & Sons, Interscience Publ.Comp., New York, 1970

[13] W. Davenport and W. Root; Random signals and noise; Mc Graw Hill Book Comp., New York, 1958

[14] M. C. Wang et al.; On the theory of Brownian motion; Rev.of Modern Phys. 17 , 323-342, 1945

[15] B. Berne and R. Pecora; Dynamic light scattering; John Wiley & Sons, New York, 1976

Chapter 3 :

SINGLE CELL ABSORPTION SPECTROSCOPY

3.1 SINGLE CELL VERSUS SOLUTION ABSORPTION SPECTROSCOPY

The MLLSS set-up described in Chapter 2 is obviously very useful for monitoring phenomena that happen inside single biological cells. Unlike most samples that are studied in chemical physics, the composition of the sample can change appreciably in the course of a biophysics experiment such as MLLSS on a single cell. In a sense, the sample holder of a MLLSS experiment inside biological cells is the cell membrane (though the membrane itself is part of the system under study in some MLLSS experiments). This "sample holder" is not closed: it contains channels for various components to come into and go out of the cytoplasm. Moreover, cell content can change due to internally regulated breakdown or synthesis of certain intracellular proteins. Both mechanisms result in a potentially strong change of the content of the scattering volume. One example is the oxygen content of red blood cells when the oxygen content of the medium in which the cells are suspended, changes in time. Another example is the protein composition of eye lens cells when some of these cells differentiate. It is usually easy to control the composition and state of the cell suspending buffer. However, it is often impossible to relate these extracellular conditions to intracellular conditions in a direct way. Therefore, it is important to

measure the variable of any single cell experiment directly at the single cell level. Absorption spectroscopy is a useful means to this end. The absorption of radiation by molecules is very sensitive to the composition and the structure or conformation of the molecule. When the absorption properties of a certain molecule are known as a function of a variable X from absorption spectroscopy on bulk suspensions of that molecule, then MLLSS could study the motion of these molecules inside a cell as a function of X by combining MLLSS and absorption spectroscopy on that same cell.

A clear example is found in the oxygenation and deoxygenation of hemoglobin in red blood cells. It is easy to control the partial oxygen pressure pO_2 of the buffer in which red blood cells are suspended by blowing a gas mixture of known pO_2 onto the surface of the buffer (stirring the buffer to speed up the process of replacing the solubilized air by the given gas mixture) till the buffer is saturated with the gas mixture. Red blood cell membranes are porous to oxygen [1] so that the pO_2 inside and outside the cell should be at all times identical. The important parameter in the study of hemoglobin aggregation is, however, not ambient pO_2, but the degree to which the hemoglobin is oxygenated. This is called the oxygen saturation level of the hemoglobin. Now the absorption spectrum of oxygenated and of deoxygenated hemoglobin are very different and well known from absorption measurements on hemoglobin solutions. Though there is a one to one relation between pO_2 and oxygen saturation of hemoglobin in solution, this may not be the case inside red blood cells (see absorption experiment in section 4.4.f). Therefore single cell absorption spectroscopy is very useful in the study of hemoglobin motion inside single cells. The normal red blood cell is used in this chapter to illustrate the technique which makes use of an optical multichannel analyzer (OMA).

3.2 THE OPTICAL MULTICHANNEL ANALYZER

Figure 3.1 shows a schematic diagram of the single cell absorption spectroscopy set-up. The most important component in the set-up is the array of intensified detectors. It consists of 512 photodiodes. In the unintensified version, the detector sensitivity at 500 nm is about 2500 photons/count. We found this to be insufficient for the small amount of light that we analyze. The microscope white light is picked up in the intermediate real image with a 450 μm diameter optical fiber embedded in one of the eyepieces (Gamma Scientific eyepiece model 700-10-34A). This light is lead to a narrow slit in front of a grating inside a monochrometer (EG&G PAR Model 1229). The grating splits the light into its different wavelength components and portions of this spectrum fall onto the photodiodes. By the time it reaches this stage, the light intensity is weak and we found we needed the intensified version of the photodiode arrays. They are built by Reticon and built into an OMA by Princeton Applied Research (EG&G PAR Model 1451-3). Its sensitivity at 500 nm is about 100 photons/count. The sensitivity is very non uniform as a function of wavelength, but this does not affect our results as will become clear in the next section.

The most important property of the OMA used for single cell spectrometry is that the spectrum (intensity as a function of wavelength) is measured simultaneously for all wavelengths. Indeed, all the photodiodes in the array are illuminated at the same time. The output signal of each diode is accumulated during a time set by the operator (typically 3 seconds in our red blood cell experiments) after which the array is read out sequentially and the information is stored in the multichannel analyzer.

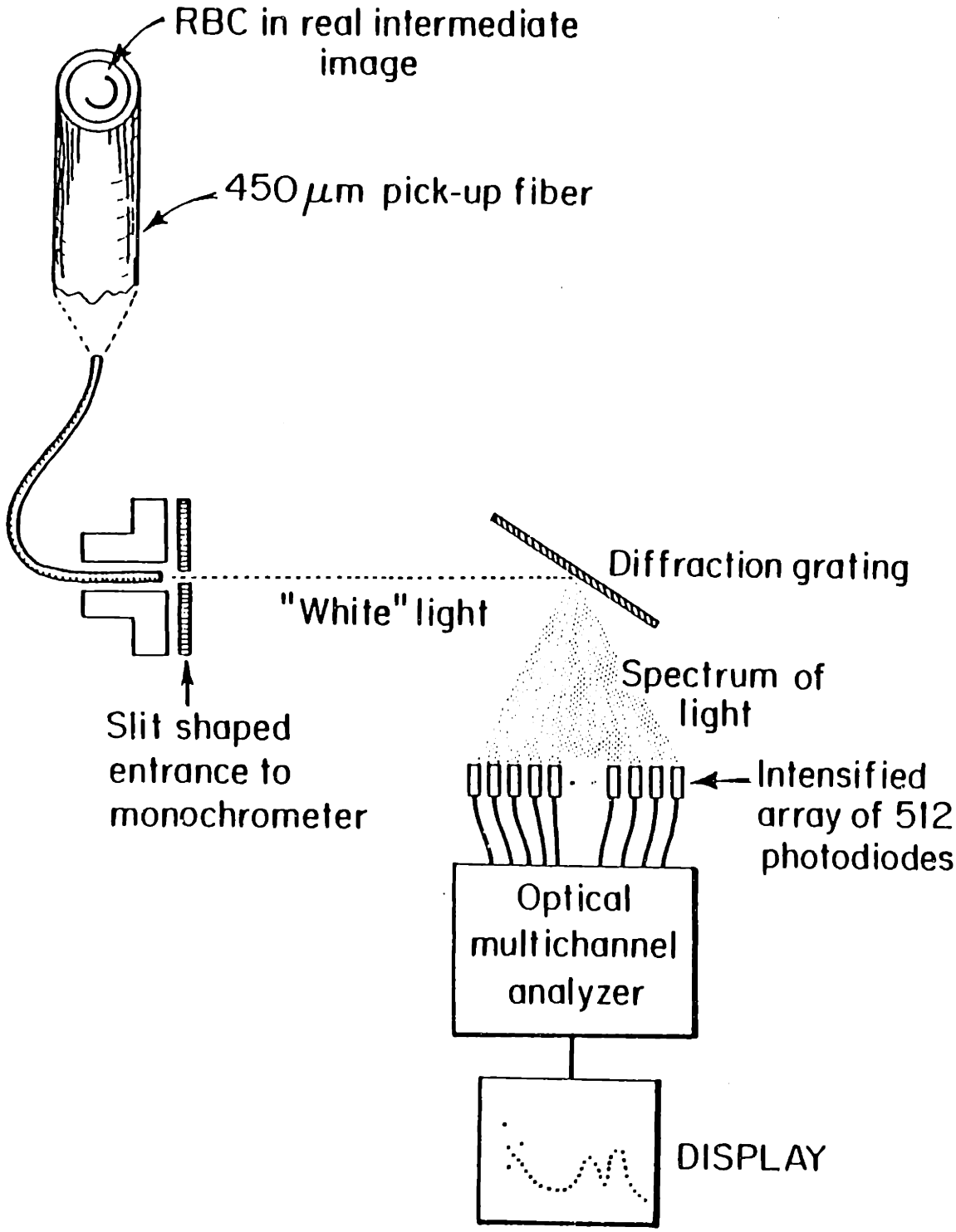

Figure 3.1 Schematic diagram of the Single Cell Absorption Spectroscopy using an Optical Multichannel Analyzer

Details on these so called self-scanned arrays can be found in [2]. During the accumulation time, it is possible for the cell to move or deform slightly so that the amount of light collected can vary during the build-up of the spectrum. This, however, affects the intensity at all wavelength by the same amount and thus the spectrum is not distorted by this cell motion. The intensity of the microscope light may also fluctuate during the accumulation of the spectrum, but that will not affect the spectrum either since it is measured simultaneously for all wavelengths. For these reasons, we feel the photodiode array spectrum analyzer has a big advantage over the more traditional scanning spectrometer.

3.3 ANALYSIS OF SINGLE CELL ABSORPTION SPECTRA ON RED BLOOD CELLS

The absorption spectrum of light transmitted through any cell is constructed as follows. First one records the dark spectrum of the detector. Even without the sample illuminating light on, stray light from the surroundings of the experiment and some darkcount of the detector itself give rise to a non-zero spectrum when the light source is off. We call this spectrum Dark(λ) where λ is the wavelength. Then one turns on the light source, in our case the unmodified 15 W halogen lamp of the microscope. One collects two spectra: one through the suspension medium of the cells and one through a cell (see Figure 2.11.a. for the 450 μm optical fiber placed in between cells and on a cell). The spectra are called respectively Background(λ) and Throughcell(λ). These three curves are stored in the OMA which then computes the spectrum that contains all the interesting information and which I will call CELL(λ):

$$CELL(\lambda) = \frac{Background(\lambda) - Throughcell(\lambda)}{Background(\lambda) - Dark(\lambda)} .$$

The numerator is the spectrum absorbed by the cell and the denominator is the spectrum of the microscope lamp alone. It reflects the spectral sensitivity of the detector and the characteristics of the light source. Figure 3.2 shows all of these components over the entire spectral range of the detector.

The wavelength range over which our detector functions is from approximately 375 nm to 640 nm. The resolution in wavelength is about 0.5 nm considering there are 512 channels illuminated by a 265 nm wide spectrum. The dead area between the adjacent photodiodes is very small. The spectral sensitivity is however too low at the low wavelengths. This is clear from the noise level in the lower window of Figure 3.2. Therefore, in the case of red blood cells, we usually only use the spectrum between 500 nm and 600 nm. We wish to extract from these spectra the oxygen saturation level of the hemoglobin inside the red blood cell from which the spectrum is taken. This is done by fitting the spectrum to a linear combination of two standard spectra. One is the oxy-standard. It is taken on a fully oxygenated cell, a cell from a suspension that is saturated with a 95% O_2 + 5% CO_2 mixture. The other one is the deoxy-standard. That one is taken on a cell from a suspension that contains 2% Sodium-Meta-Bisulfite which is a strong reducing agent. Figure 3.3 shows such a fit. It shows the experimental curve $CELL(\lambda)$, the oxy-standard, the deoxy-standard and the fitted curve, all of them smoothed. The result of the fit on this particular spectrum was 51% oxygen saturation.

It is obvious that not all experiments on single cells will have an important variable that is as readily measured through absorption

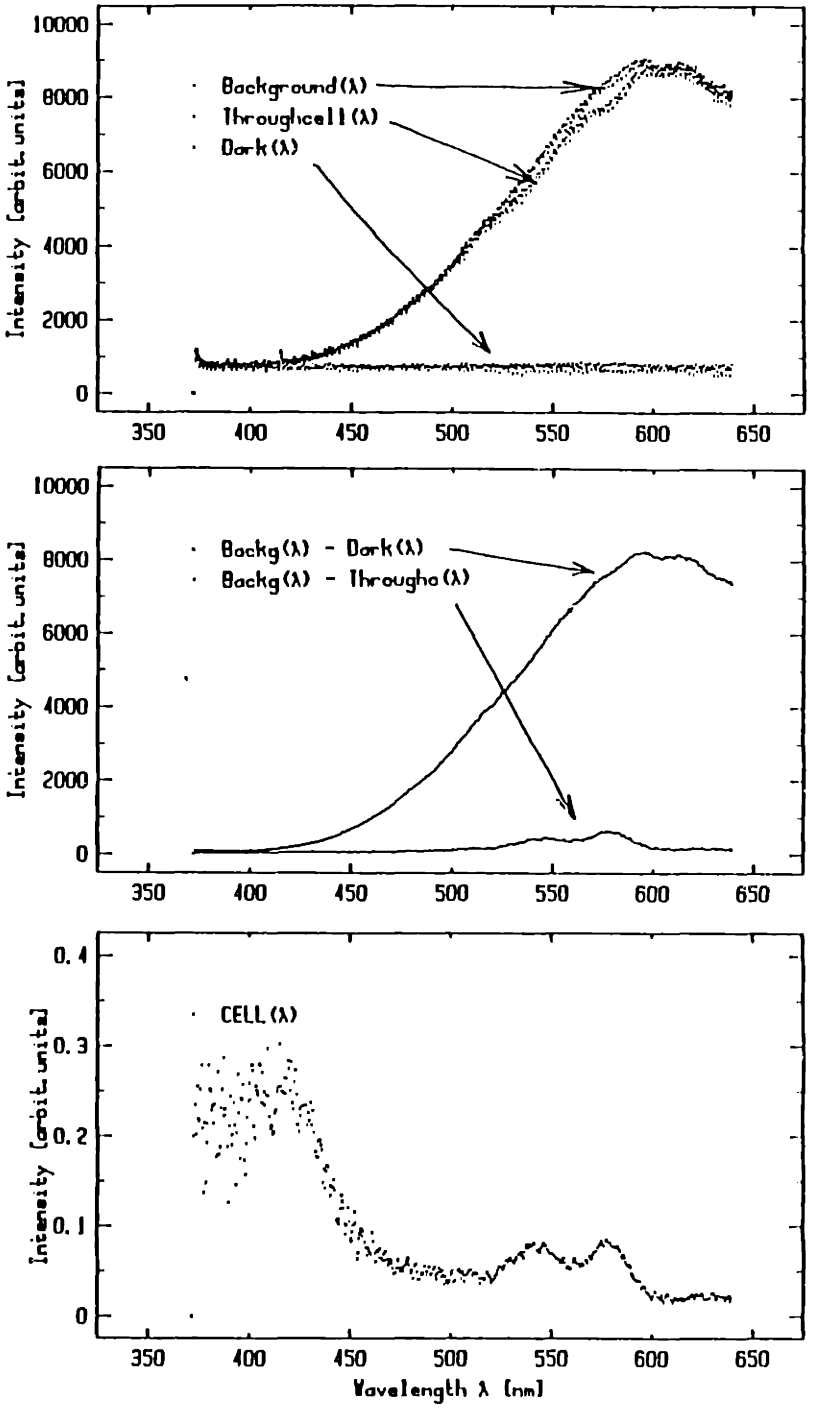

Figure 3.2 The formation of the absorption spectra: Intensity as a function of wavelength is recorded for the darkcount of the array of photodetectors (Dark), for the light transmitted through the cell suspension fluid (Background) and through a cell (Throughcell). They are shown in the top window. The middle window shows the differences Background-Dark and Background-Throughcell. The bottom window shows the absorption spectrum in the form

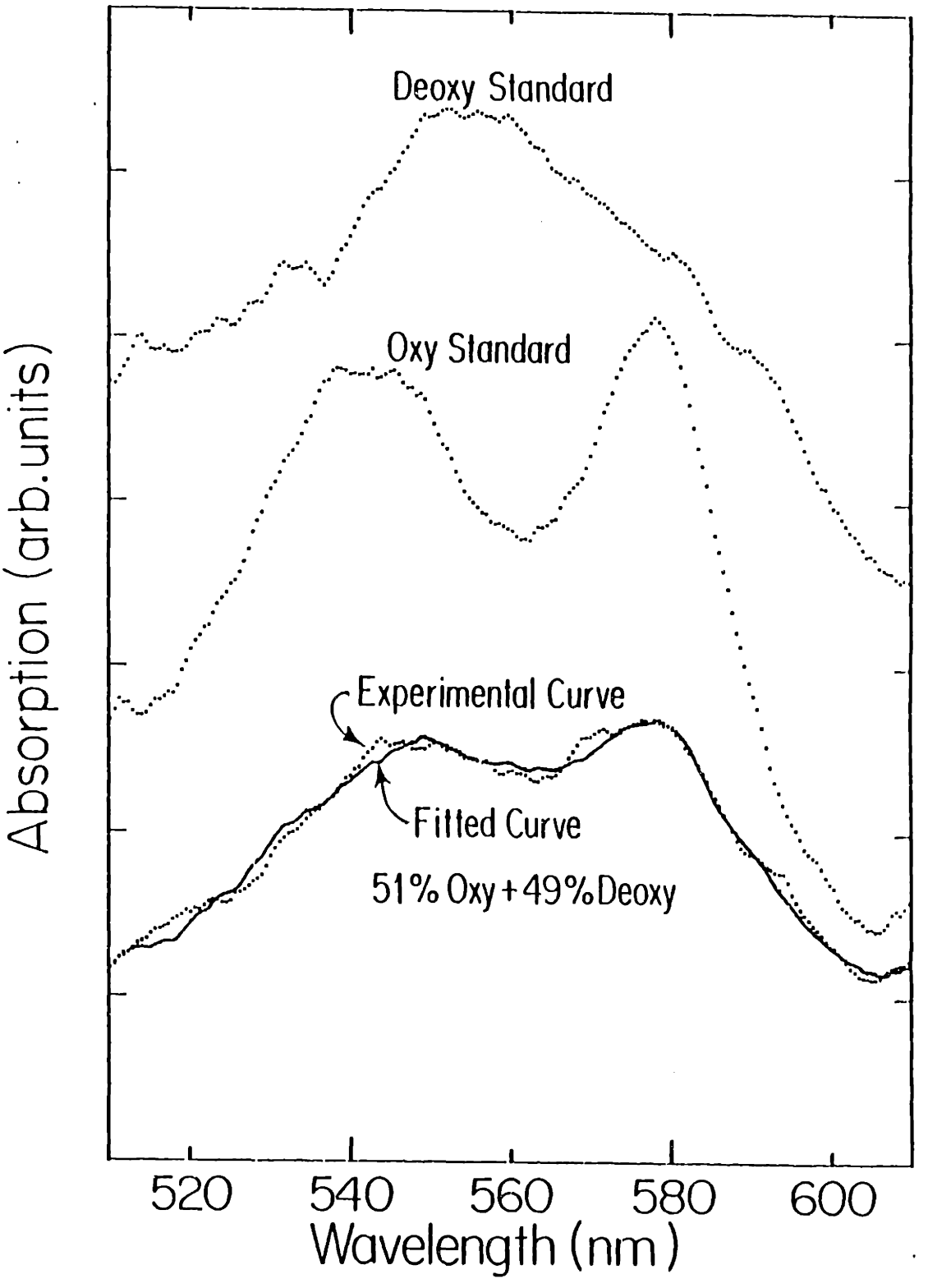

Figure 3.3 An experimental absorption curve constructed as shown in Figure 3.2 taken on a fully deoxygenated, on a fully oxygenated and on a intermediately oxygenated red blood cell. The fitted curve is a linear superposition of the fully oxy and fully deoxy curves and yields the intermediate oxygen level of 51% (which corresponds to 76.5 mmHg)

spectroscopy as is the case for red blood cell experiments. Yet, a large amount of intracellular phenomena are associated with a specific absorption picture. Moreover, biochemistry is getting better and better (for example [3,4]) at tagging specific molecules on cell membranes and inside cells, with fluorescent labels that fluoresce only under specific conditions. The single cell absorption spectroscopy technique described here, could of course be used in the study of any such fluorescence experiment.

REFERENCES

[1] porosity of RBC membrane to air

[2] Y. Talmi et al.; Self-scanned photodiode array: a multichannel spectrometric detector; Applied Optics 19 , 1401-1414, 1980

[3] R. Nairn; Fluorescent protein tracing 4th Ed. Churchill Livingstone, New York (1976)

[4] M. Spencer; Fundamentals of light microscopy Cambridge University Press, Cambridge (1982)

Chapter 4 :

NORMAL AND SICKLE RED BLOOD CELLS: HEMOGLOBIN AGGREGATION AND MEMBRANE FLEXIBILITY

4.1 RED BLOOD CELLS AND SICKLE CELL ANEMIA

Red blood cells (RBCs) or erythrocytes are mostly bags of hemoglobin (Hb). As such, their main function is the oxygenation of tissue as the intracellular Hb is oxygenated when the RBCs pass through the lungs and deoxygenated when they reach the capillaries in oxygen requiring tissue. Hb constitutes 97.5% of the cytoplasmic protein weight in the erythrocytes and its concentration is about 5mM. Other proteins are responsible for regulating the cell function and for maintaining the integrity of the cells. Na^+ and Ca^{++} are present at concentrations lower and K^+ at concentrations higher than inside the cytoplasm. Actin and spectrin are found below the cell membrane and form a cytoskeletal network. Despite the very high concentration of Hb and the existence of a cytoskeleton, the Hb of normal blood cells, Hb-A, stays in solution in both the oxy and the deoxy state and the cells are extremely deformable. The largest diameter of the RBC is approximately 8μm. Yet it has no problems traversing the 2 to 3 μm diameter capillaries. This deformability decreases with cell age and is probably the criterion by which they are selected for destruction in the spleen after roughly 120 days in the circulation.

In the case of patients with sickle cell anemia, the situation is very different. In this case the Hb has a defect and is called Hb-S. This was first demonstrated in electrophoretic mobility studies by Pauling et al. in 1949 [1]. In 1956 Ingram [2] showed that the defect consists of the substitution of a valine residue for the normal glutamic acid at the sixth position of each β-chain. The chemistry and detailed structure of Hb can be found in [2] or in just about every biochemistry handbook. Here I wish only to briefly discuss the consequences of this substitution. The defect causes a loss of two negative charges per hemoglobin molecule resulting in Hb-S aggregation when it is in the deoxy state. The structure of the Hb-S aggregates is very well known (for example [3]), but, once again, I will not go into details. For the purpose of this study, the important features of these aggregates are that they are rigid and can grow up to lengths larger than the diameter of the RBCs. Such long Hb polymers stretch the cell and deform it into "sickled", hardly deformable cells. Figure 4.1 shows both normal and sickled eryhtrocytes. Up to a certain point, which is not yet well determined, the sickling is reversible upon reoxygenation of the cell. Some cells are, however, irreversibly sickled (ISC). ISCs are denser than the other erythrocytes of the same person and have a higher intracellular Ca^{++} concentration. Some claim they are the older cells, but this is the subject of controversy [4,5]. Clinically, sickle cell anemia is associated with insufficient oxygenation of tissue due to blood flow stagnation in the capillaries in which sickled RBCs can get stuck. This results in severe painful crises for the patient. Other symptoms of the disease are chronic hemolytic anemia and dangerously high iron levels in the bloodplasma, both a result of exaggerated RBC breakdown. Long-term organ damage often causes death.

Figure 4.1 Normal red blood cells (top) and Sickled red blood cells (bottom) - taken from reference [17] p.147 and p.242

It is an interesting issue why sickle cell anemia persists [6-9]. People with the mutant gene from only one parent have sickle cell trait. About 40% of their Hb is Hb-S and, except in very unusual circumstances, their are no pathologic effects associated with this level of Hb-S. One fourth of the children of parents with sickle cell trait have sickle cell anemia. The average age of sickle cell anemia patients varies widely with the availability of medical care and therefore with region. Yet, some of the regions with the worse medical facilities have the highest percentages of the population with sickle cell anemia. This is the case in parts of Africa where as much as 20% of the black population has the disease. There, many children with sickle cell anemia die before the child bearing age. Why then does sickle cell anemia persist? The reason is that the sickle cell gene provides a benefit, namely it provides some protection against the most severe form of malaria (malaria due to the parasite Plasmodium Falciparum). This works as follows. The parasite is killed in RBCs infected by the parasite when the cells sickle. Infected cells attach themselves to the blood vessels in a low oxygen environment about halfways through the reproductive cycle of the parasite. The pH is lowered in these infected cells by about 0.4 pH units, thus increasing sickling. As a result, up to 40 % of the cells of people with sickle cell trait will sickle in this environment, thus killing the parasites inside. Only 2% to 3% of non-infected RBCs would sickle in sickle cell trait blood at the same oxygen pressure. Thus, though not completely protective, the presence of Hb-S in RBCs lessens the severity of malaria and gives people with Hb-S a relatively increased survival rate. This is why sickle cell anemia has remained stable at about 20 % in African populations.

Why normal and sickle red blood cells are a good system for a feasibility study on MLLSS ? Sickle cell anemia is certainly one of the best studied and best understood human diseases. Already about 30 years ago, Linus Pauling called sickle cell anemia a "molecular disease". Since, a vast amount of clinical and biochemical studies have been performed. Few experiments though were done at the single cell level. In fact, morphologic studies of sickle RBCs under different conditions may be the only single cell experiments performed in the context of sickle cell anemia. It is thus not surprising that some questions still remain unanswered in this field. This is why normal and sickle RBCs have formed an ideal system for demonstrating the feasibility and utility of single cell dynamic laser light scattering spectroscopy, MLLSS. Enough is known about these cells so that, at least on average, the state of the intracellular Hb is known as a function of condition. Indeed, the effect of variables such as temperature, pH, intracellular Hb concentration and concentration of chemicals that affect Hb oxygenation are well documented from studies on suspensions of many cells or on cell free Hb solutions. Therefore, on the one hand we were not working in the dark when doing MLLSS on single RBCs and, on the other hand, we have provided information that is of interest and, in some instances, surprising to the sickle cell anemia researchers.

In this chapter, I will discuss the experiments we performed on RBCs, the method for data analysis and the significance of the experiments. I present them approximately in the order in which they were done, because I feel it adds to the understanding of the development and difficulties of our single cell work. Data and data analysis of MLLSS and/or single cell absorption spectroscopy are presented on

a. Brownian motion of Hb in osmotically swollen and shrunken normal RBCs (Hb-A)

b. Motion of Hb monomers and polymers in sickle RBCs as a function of ambient partial oxygen pressure (Hb-S)

c. Possible aggregation of Hb under extreme conditions in normal blood (Hb-A)

d. Irradiation damage on normal RBCs (Hb-A)

e. Kinetics of Hb depolymerization in sickle BRCs (Hb-S)

f. Cell-to-cell variability in oxygenation saturation as a function of partial oxygen pressure (Hb-A and Hb-S)

g. Reversible oxygenation and deoxygenation of RBCs in a flow cell (Hb-A and Hb-S)

h. Possible induction of irreversibly sickled cells by repeated oxygenation-deoxygenation cycling of sickle RBCs (Hb-S)

i. Membrane flexibility in normal and sickle RBCs (Hb-A and Hb-S)

4.2 SAMPLE PREPARATION COMMON TO ALL RBC EXPERIMENTS

4.2.a. Sickle and normal blood

Sickle blood was collected from a single donor (31 years old female) using heparin as an anticoagulant and storing it with CPD (citrate phos-

phate dextrose - adenine) solution. It was reported [10] that this method allows sickling experiments for more than 10 days after collection of the blood. All the data on sickle cell anemia blood presented were taken within 6 days after withdrawal of the blood. Normal blood was usually taken from ourselves by pricking our finger and mixing one or two drops of blood with CPD in a heparinized tube. All normal RBC experiments reported were done on blood taken on the day of the experiment.

4.2.b. The suspension buffer and washing the RBCs

RBCs are always "washed" in preparation of a MLLSS or an absorption experiment. This means the RBCs are isolated from other blood cells (white cells and platelets) and from the blood plasma. The non-red blood cells would not hinder any of the single cell experiments presented in this work, because individual cells are selected for any given experiment. The blood plasma, however, contains a variety of proteins, some of which scatter or absorb light in the regime of the MLLSS or Hb absorption experiments.

The cells are washed in buffer of which a stock solution is made and stored in the freezer. In order to fully solubilize all components of this buffer, it is fastest to thaw it while stirring it and warming it up. Attention should be paid not to heat it over about 50°C, because some precipitation will occur at higher temperatures. The amount of buffer needed for the sample preparation is taken out of the stock solution, which is immediately put back in the freezer. In this way, I have found that the buffer can be kept for two months (it may be good for longer, but I never tried). The recipe for the buffer is the following:

110 mM sodium chloride (NaCl)

5 mM potassium chloride (KCl)

27 mM sodium bicarbonate ($NaHCO_3$)

2.4 mM sodium phosphate (Na_2HPO_4 and $NaH_2PO_4.H_2O$ in a ratio of 31 to 138 by weight)

1 mM magnesium chloride ($MgCl_2$)

30 mM glucose ($C_6H_{12}O_6$)

1 mM adenine ($C_6H_5N_5$)

1 mM inosine ($C_{10}H_{12}N_4O_5$)

This buffer is saturated with a 95% air + 5% CO_2 gas mixture (all gas mixtures were obtained from Med-Tech, Medford, Mass.) by bubbling the gas through the buffer while stirring it for about 20 minutes for 100 ml of buffer. (Any gas used is humidified by passing it through water at one point between the gas tank and the sample. This is done to avoid the possibility that the gas would partially dry the sample which would alter the osmolarity of the suspension buffer.) Then, 0.5% of bovine serum albumin (BSA) is added and gently stirred into the buffer while continuing to blow the air-CO_2 mixture onto the surface of the buffer. Bubbling the gas through the solution with BSA will form bubbles and denature the BSA. The BSA is necessary for the cells to maintain their shape. In the absence of BSA the RBCs develop little spikes all over their surface; this state is called "crenated". I have often washed the cells in buffer + 2% BSA and then suspended them in buffer + 0.5% BSA after the last wash to give the

cells a more gentle transfer from the blood plasma to the buffer, but this may not be necessary. At this point, the buffer + BSA should have a pH of between 7.35 and 7.40. It is essential for the pH to be in this range because the oxygenation of Hb is a sensitive function of pH [11]. If the pH has not equilibrated to this value, it should be adjusted by gently adding 100 mM HCl or NaCl. The buffer is now ready for washing and resuspending the RBCs. It can maintain the metabolism of the RBCs for 24 hours at 37°C [10].

Preparation of the cells is done at room temperature, but experiments are all performed at 37°C. Usually, 0.2 ml of whole blood is added to 4 ml of suspension buffer, mixed well and spun in a fixed angle table top centrifuge at 2000 rpm for about 3 minutes. The RBCs form a dense pellet at the bottom of the centrifuge tube. The supernatant is poored off and the procedure is repeated 3 times, i.e. the RBCs are washed three times. After the last wash, the cells are resuspended in 0.5 ml of buffer and 0.02 ml of this suspension is added into about 0.5 ml of buffer. The final concentration of RBCs determines the density of cells on the bottom surface of the sample holder after they have settled and are ready for MLLSS or absorption spectroscopy. The concentration for the figures gives above yields an average separation between cells of roughly 7 cell diameters. In some experiments, this concentration was raised or lowered. It will be mentioned explicitly. The final RBC suspension is equilibrated with gas of a certain partial oxygen pressure (usually 0 mmHg (95% N_2 + 5% CO_2 mixture) or 150 mmHg (95% air + 5% CO_2 mixture)), by blowing the gas onto the surface of the sample while gently stirring the cells. After about 30 minutes the sample is ready to be transferred into the sample holder.

4.2.c. Separation of RBCs by density

In some experiments, RBCs of a given concentration were used. This was the case mostly when cell-to-cell variation in a certain cell property were investigated or when the study was related to the formation of irreversibly sickled cells. Figure 4.2 shows a photograph of normal blood and sickle cell anemia blood on a continuous density gradient with density varying from 1.06 to 1.08. It is striking that the normal RBCs bunch together in a narrow density region and that the sickle RBCs, in contrast, spread over a much wider density range. The most important difference is that normal blood does not contain the very dense cells found in sickle blood. The irreversibly sickled cells, that can make up to 30% of the total RBC population in sickle cell anemia [5], are a portion of these densest cells. The wide spread in RBC density in sickle cell anemia blood has been known for a very long time and we wanted to rule this factor out in the analysis of cell-to-cell variations in some of the studied quantities. This is why cells were sometimes separated according to density. It will be explicitly mentioned when this is the case.

The continuous density gradient is made in the following way. Start with a 0.9% NaCl solution and a stock of Percoll (density gradient solution, Pharmacia) that is pH adjusted to 7.38. Their density is 1.0046 and 1.13 respectively. Mix them in the appropriate amounts to form two mixtures, one of density 1.06 and one of density 1.08. These densities were determined by trial and error and seem a good choice for the patients from whom we received our blood samples. For other patients or even for the same patient under very different conditions, these densities may have to be changed. Put 5 ml of the density 1.06 mixture in one 15 ml test tube

Figure 4.2 Normal (left) and Sickle cell anemia blood (right) on identical Percoll continuous density gradient. The "major" band and "densest" cell region were used for experiments

and 5 ml of the density 1.08 mixture in another 15 ml test tube. Place a mini stirring bar in each and connect the test tubes with a syphon tygon hose. Keep the test tubes at the same level above a magnetic stirrer. Connect the high density tube with another tygon syphon hose to a 15 ml corex test tube at a lower level. (I usually put 0.5 ml of 100% percoll in the bottom of this corex tube to fill the rounded section. In this way the density in the corex tube is linear with height above the rounded bottom.) This makes a density gradient which varies continuously between 1.06 and 1.08. Figure 4.3 illustrates the little set-up. A small amount of blood is carefully placed on top of this gradient (0.75 ml for the photographs of Figure 4.2 and about 0.1 ml for experiments) and the tube is spun in a fixed angle centrifuge at 4000 rpm for 20 minutes. Cells of a certain density are taken out of the corex tube with a glass pipet (it takes some practice to do this without mixing the layers or picking up cells from several levels). Usually about 0.3 to 0.5 ml of sample is taken out. 1ml of suspension buffer is added and the cells are spun as done for the cell washing described above. The cells are washed a total of three or four times.

4.3 SAMPLE HOLDER

Two sample holders were used in this work. One is a microcapillary (Vitro Dynamics, #5010, 50mm long, 0.1mm path length), the other is a flow cell (Hellma Cells #136/OS, 0.5mm path length); both are commercially available. The microscope stage accommodates for both sample holders as was described in section 2.3.b. It will be stated with each experiment

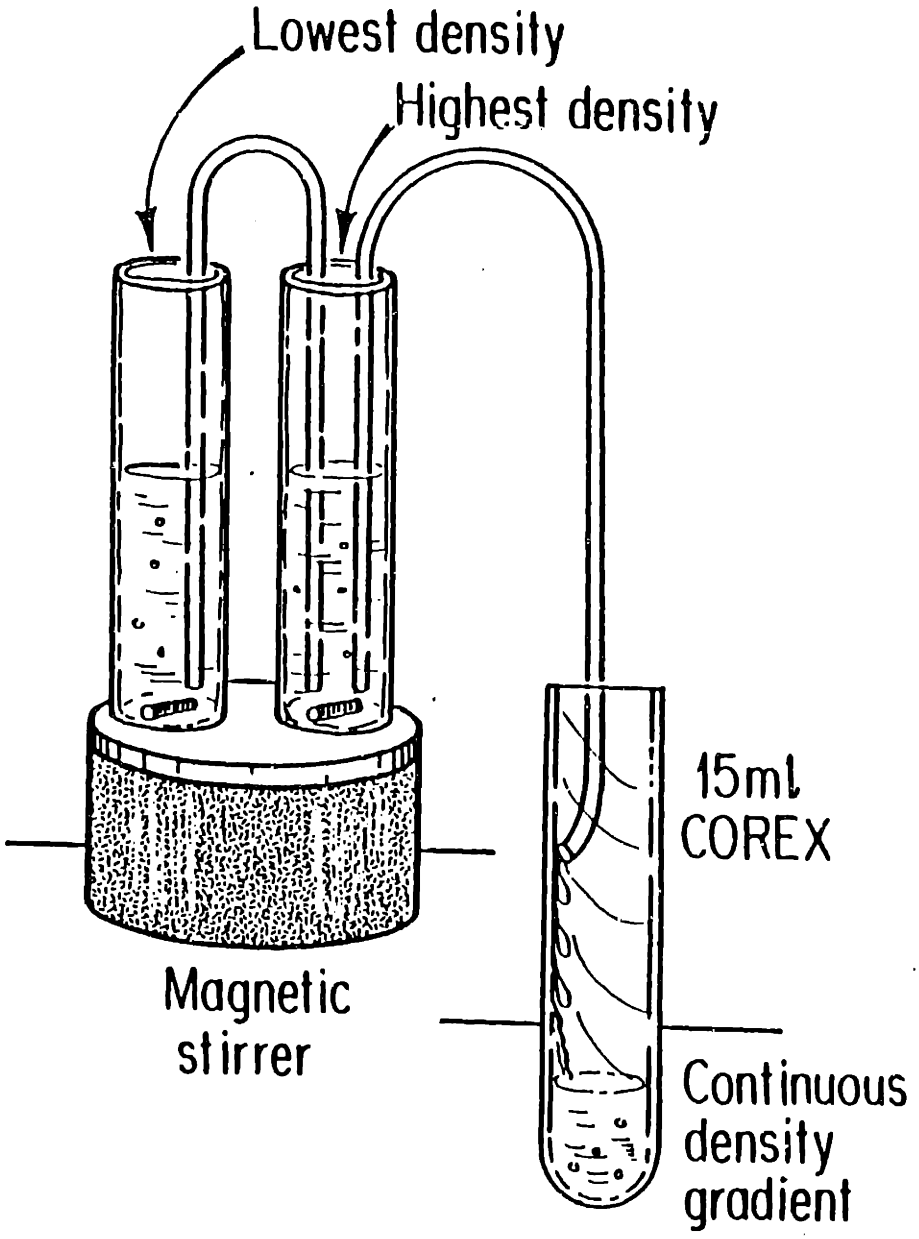

Figure 4.3 Set-up for making a continuous density gradient in a 15ml Corex test tube

which sample holder was used.

4.3.a. The microcapillary sample holder

The microcapillary sample holder is much easier to use than the flow cell, but is does not allow for a change of buffer while monitoring one same RBC. It is therefore always used for quick inspection of the sample, but it was used for real experiments too. Figure 4.4a. shows the microcapillary holder. The capillary is preflushed with the gas mixture that the RBCs are equilibrated with. Then the sample is aspirated into the capillary by capillary action. Both ends are dipped in a putty (Critoseal, Lancer) and the capillary is placed between two microscope cover glasses with a drop of silicone oil for optical matching. This is done to improve the quality of the sample holder surface; the microcapillary tubes are rather irregular which causes high levels of stray light scattering. After a few minutes on the microscope stage, the cells have settled to the bottom of the sample holder were they sit still rather well due to the large area of contact between the RBCs and the glass and the absence of flow inside the capillary. The thickness of the sample holder is roughly 50 times the thickness of a RBC so that there is plenty of buffer around to provide the nutrients needed to keep the cells metabolically active for many hours.

4.3.b. The flow cell

The flow cell is appreciably more complicated to set-up. Figure 4.4b. shows the cell with its connections to the buffer containers. In order for the RBCs to stay attached to the bottom of the flow cell when buffer is pushed through, a drop of a 0.1% solution of poly-l-lysine in water (Sigma Poly-l-lysine-hydrobromide, MW 150000-300000) is placed in the center of

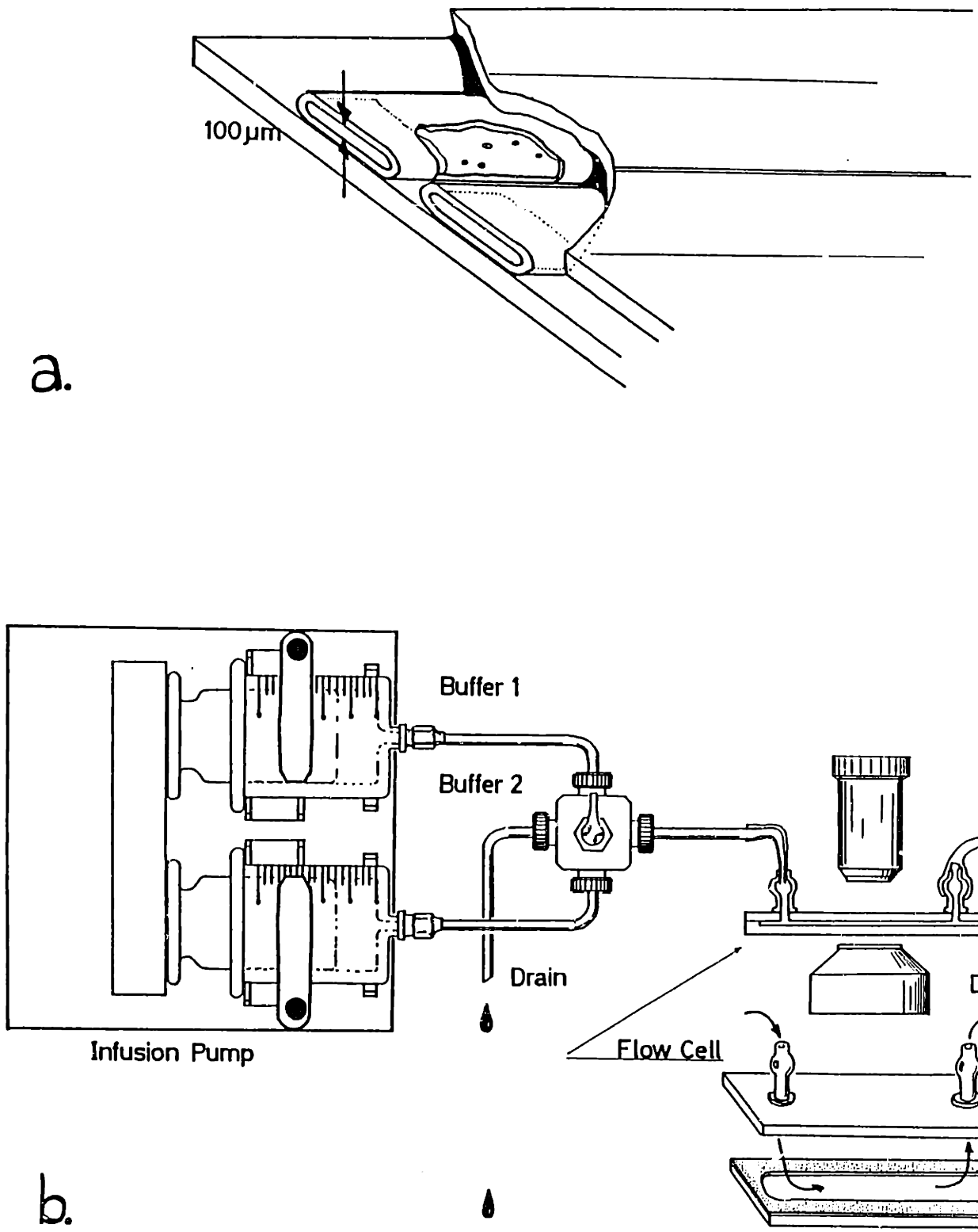

Figure 4.4 Sample Holders: (a)the Microcapillary and (b)the Flow Cell

the bottom part of the flow cell and left there for about 10 minutes after which the excess poly-l-lysine is rinsed off with distiled water. Poly-l-lysine has positive end groups and sticks strongly to the glass; there is no risk for washing it away. It is used commonly in biology for anchoring biological cells, which almost always have negatively charged membranes [12,13]. After the experiment is finished, washing the cell with soap and soaking it in cleaning solution overnight removes the poly-l-lysine. The bottom of the cell is then rinsed with some suspension buffer and about 0.5 ml to 1 ml of the RBC suspension is placed on it. After 15 minutes the cells have settled to the bottom and gotten anchored to the glass. The sample cell can be closed and mounted onto the microscope stage. In flow experiments, there were always two different buffers that are alternatively flown through the sample cell. These buffers sit in 50 cc syringes that are mounted on an infusion pump, which is basically a box of gears that drive a the plungers of the syringes at variable speeds. The infusion pump we used (Harvard Apparatus Compact Infusion Pump) can be set to rates from as low as 0.0027 cc/min to 46 cc/min on 50 cc syringes. To avoid diffusion of air into the buffers, glass syringes and stainless steel leads are used to connect the syringes to the flow cell. The two leads are attached to a small two way stainless steel valve: one way leads to a dump and the other to the flow cell. It takes some practice to put together this system without trapping air bubbles inside the flow cell. The syringes are kept at room temperature and the flow cell is at 37°C. If the buffers are prepared at room temperature, we found that bubbles will develop inside the flow cell after a while. This is due to the decreased gas solubility at the higher temperature. Because the buffers are really saturated with gas before being put into the syringes, they start degassing when they reach

the 37°C chamber. Therefore, the buffers, constantly stirred, are kept between 37°C and 43°C while the gas mixture that they are equilibrating with, is blown onto their surface. The valve, though mounted on the temperature controlled microscope stage, is thermally insulated from it. This is because the stage reaches temperatures up to 45°C to 50°C in order for the sample to be kept at 37°C (see section 2.3.b). If the valve warms up to these temperatures, higher than the ones inside the flow cell, the buffers will degas and bubbles will eventually be pushed into the flow cell. For all flow cell experiments, the cell is flushed at a rate of 0.15 cc/min for about 10 minutes or until loose cells seem to have been flushed away. At this flow rate, the velocity difference across the RBCs is

$$\Delta u = u_{top} - u_{bottom} \qquad 4.1$$

$$= u_{top} - 0$$

$$= 1.5 \times 10^{-2} \ \mu m/sec$$

for typical RBC dimensions (see Appendix VI-1 for derivation and details). This velocity gradient makes some of the cells slightly tear-shaped, but they immediately regain their smooth biconcave shapes when the flow is turned down. The selection of the final flow rates depends on the experiment. Typically, if a comparison is made between cells in two different buffers, the switching from the one buffer to the other, from the one syringe to the other, is done at 0.15 cc/min and, once flushed with the new buffer, a low rate of 0.01 cc/min or less assures the maintenance of the new buffer conditions. If the cells are to be monitored throughout the change from the one to the other buffer, the flow rate is 0.056 cc/min or

0.078 cc/min which is appropriate to collect about 10 MLLSS or absorption data points between the one and the other condition. The specific settings of the flow cell set-up will be mentioned for each reported experiment.

4.4 EXPERIMENTS ON NORMAL AND SICKLE RED BLOOD CELLS

4.4.a. BROWNIAN MOTION OF HEMOGLOBIN IN OSMOTICALLY SWOLLEN AND SHRUNKEN NORMAL RBCs (Hb-A)

These experiments were reported as an illustrative example of the applicability and sensitivity of the MLLSS set-up in a paper which presents a fairly detailed description of the technique (I.Nishio, J.Peetermans and T.Tanaka; Microscope Laser Light Scattering of Single Biological Cells; Cell Biophysics, 7, p.91-p.105, 1984). Hb is present in the RBCs at a very high concentration (approximately 34 mg/ml). Interactions between the Hb molecules are not negligible and the diffusion coefficient of the Hb is a sensitive function of the intracellular Hb concentration and thus of the RBC volume. A study on osmotically swollen and shrunken RBCs provides a simple demonstration of this feature.

Sample Preparation and Sample Holder

Cells from two normal donors are washed three times in the suspension buffer described previously. The ionic strength of this buffer is 300 milli-osmoles, which is very close to that inside the RBCs. The buffer is mixed with various amounts of water to decrease the osmolarity and make a

buffer in which the cells swell. To shrink the cells, the buffer was mixed with various amounts of 0.3M NaCl. The ionic strength in this study ranged from 175 to 450 milli-osmoles. All the experiments were done at atmospheric partial oxygen pressure (150 mmHg). The sample holders were always the microcapillary cells.

Data and Data Analysis

Intensity autocorrelation functions are taken at the small angle and the large angle configuration on 10 RBCs at each ionic strength studied. At the time of this experiment, the flow cell was not yet incorporated in the MLLSS set-up. Therefore, measurements were made on many cells at each osmolarity and the average value of these measurements is presented. The more elegant way to do this swelling and shrinking experiment would be by following individual RBCs as they are exposed to buffers of different osmolarity in the flow cell. Yet, the results of this study seem conclusive and worth discussing.

Figure 4.5 shows a typical set of correlation functions. These particular data were taken at the forward scattering angle. It is clear that the correlation functions are not single exponentials. They were analyzed with a double exponential analysis, namely the correlation functions $c(\tau)$ were fitted to an expression of the form (see Eq.2.28)

$$c(\tau) = \left[A_1 \exp\left(-\frac{\tau}{T_1}\right) + A_2 \exp\left(-\frac{\tau}{T_2}\right)\right]^2 + B \qquad 4.2$$

Here T_1 is assigned to the Brownian motion of the Hb molecules and T_2 is assigned to much slower motion such as elastic deformation of the RBCs. The time independent term B is the baseline of the autocorrelation function. In this experiment, the quantity of interest is the diffusion

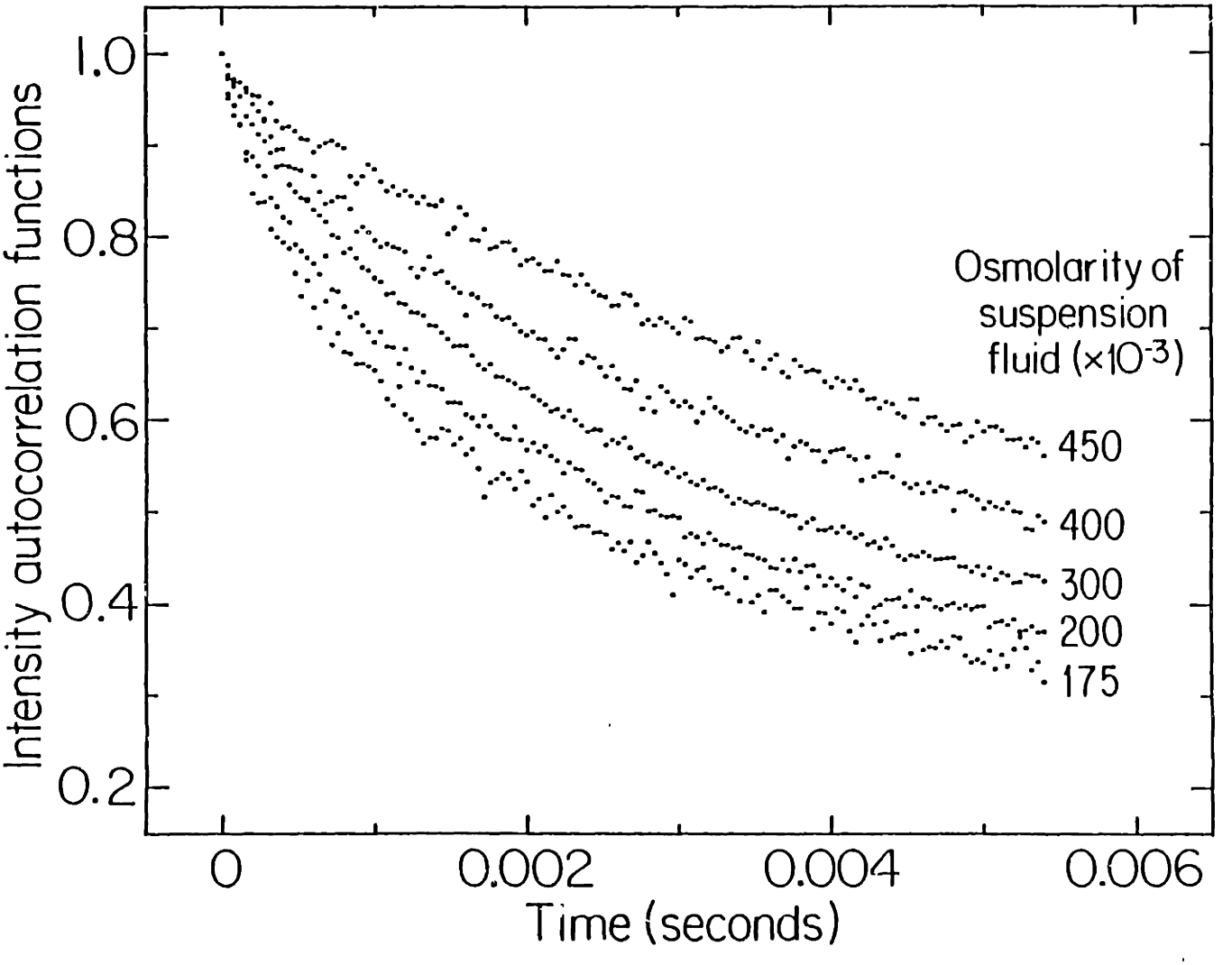

Figure 4.5 Intensity Autocorrelation functions taken on red blood cells suspended in different osmolarity buffers

coefficient D_0 of the intracellular Hb and its dependence on osmotic volume changes of the RBCs. This quantity is simply extracted from the fast decay constant T_1 through (see Eq.2.13)

$$D_0 = \frac{1}{T_1 k^2} \qquad 4.3$$

where the inverse wavevector 1/k is approximately 1400Å at the small angle configuration ($\theta \approx 31°$) and 400Å at the larger angle ($\theta \approx 139°$). Density fluctuations cause variations in the interaction between Hb molecules. Hence, it is possible that local density fluctuations give rise to different effective diffusion coefficients. Especially at the higher osmolarities, it is possible that small fractions of the Hb forms small Hb aggregates. Both processes lead to a distribution g(D) of the fast diffusion coefficient D_0 with width ΔD around its average value $\langle D \rangle$. Moreover, the intensity scattered by Hb aggregates could show angular dissymmetry which depends both on the scattering angle and on the diffusion coefficient through the form factor f(k,D). Thus, the experimental value of the diffusion coefficient D_0 can be written as

$$D_0(k,\langle D\rangle,\Delta D) = \frac{\int_0^\infty D\, g(D)\, f(k,D)\, dD}{\int_0^\infty g(D)\, f(k,D)\, dD} \qquad 4.4$$

If one has at least good guesses for g(D) and for f(k,D), the average $\langle D \rangle$ and polydispersity ΔD can be extracted from the experimental value D_0 at two scattering angles. In this case, we did not have such guesses and limited ourselves to reporting the experimental values for D_0. Besides D_0, the cell-to-cell variability between the 10 cells measured is presented in %.

Figure 4.6 shows the diffusion coefficient corresponding to the fast decaying part of the correlation functions as a function of osmolarity for measurements at the small and the large scattering angle. Figure 4.7 shows the cell-to-cell variability in the diffusion coefficient for 10 RBCs as a function of osmolarity of the suspension buffer.

Results and Discussion

Osmotic swelling causes dilution of the Hb in the cytoplasm. As the cells are swollen further and further, the the diffusion coefficient D_o approaches the diffusion coefficient for dilute Hb monomers, 9.95×10^{-7} cm²/sec. At the lowest osmolarity, the fastest diffusion coefficient measured is 4.58×10^{-7} cm²/sec. It is not possible to swell the cells further, because they lyse at osmolarities below 175 milli-osmoles. At the backward scattering angle, both the diffusion coefficient D_o and cell-to-cell variability are constant with changes in cell volume. At the forward scattering angle, however, D_o decreases and cell-to-cell variability increases with cell swelling. These trends can be easily understood.

At the larger scattering angles, the fast decaying signal originates from the small Hb monomers. This smallest size particle is present in the swollen and shrunken cells and constitutes the fastest component under all conditions. On the other hand, at the small scattering angle, the scattered light corresponds to density fluctuations at larger length scales and the experiment is more sensitive to Hb aggregates. Their existence is a strong function of Hb concentration and as a result, the diffusion coefficient D_o measured at the small scattering angle is slower in the shrunken cells. This induced aggregation is however expected to be sensitive to the physical condition of the cell in which it occurs. For example the cell's

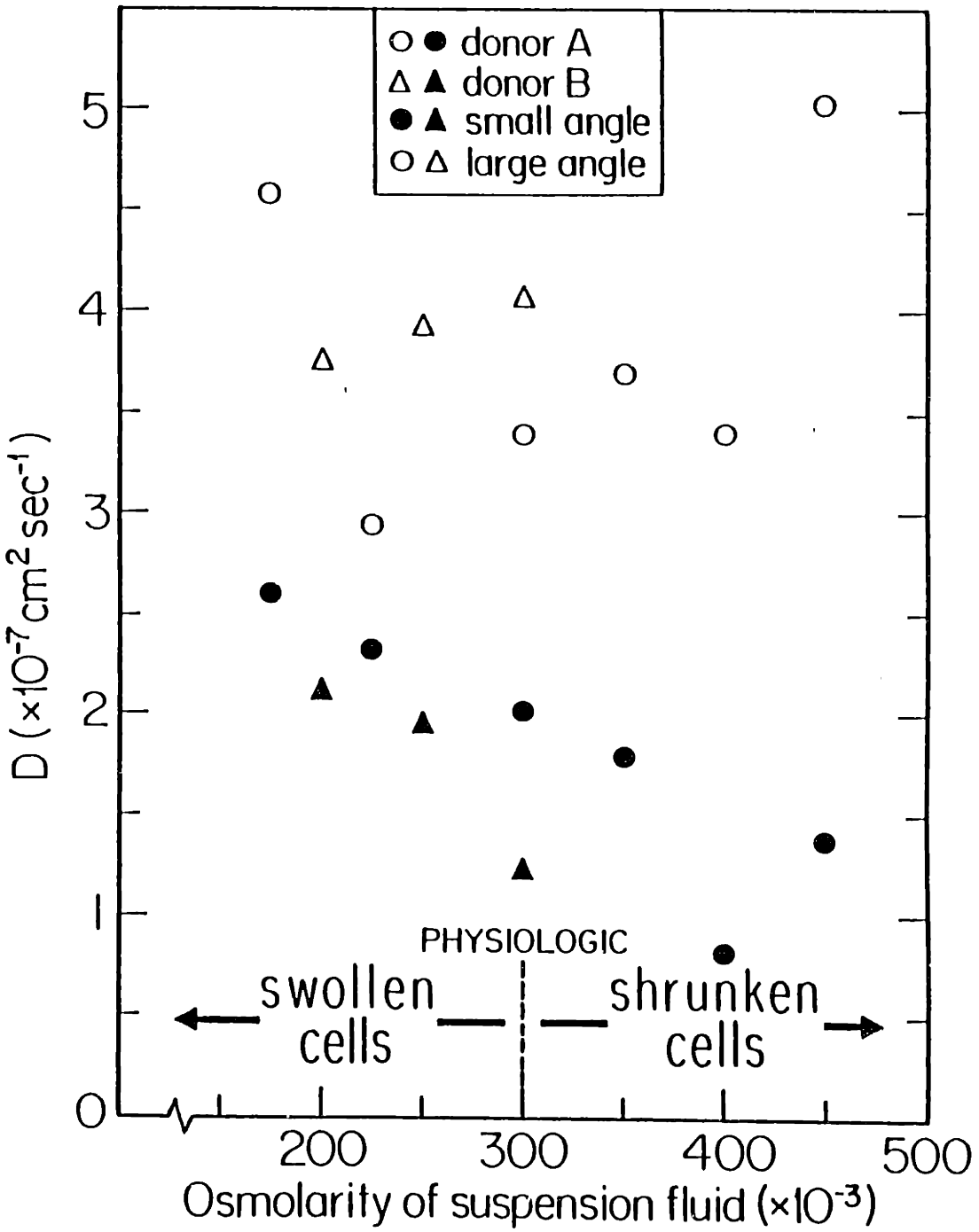

Figure 4.6 Fast Diffusion Coefficient determined by a double exponential fit on correlation functions such as the ones in Figure 4.5 plotted as a function of osmolarity of the suspension buffer. Each point is the average of measurements on 10 cells.

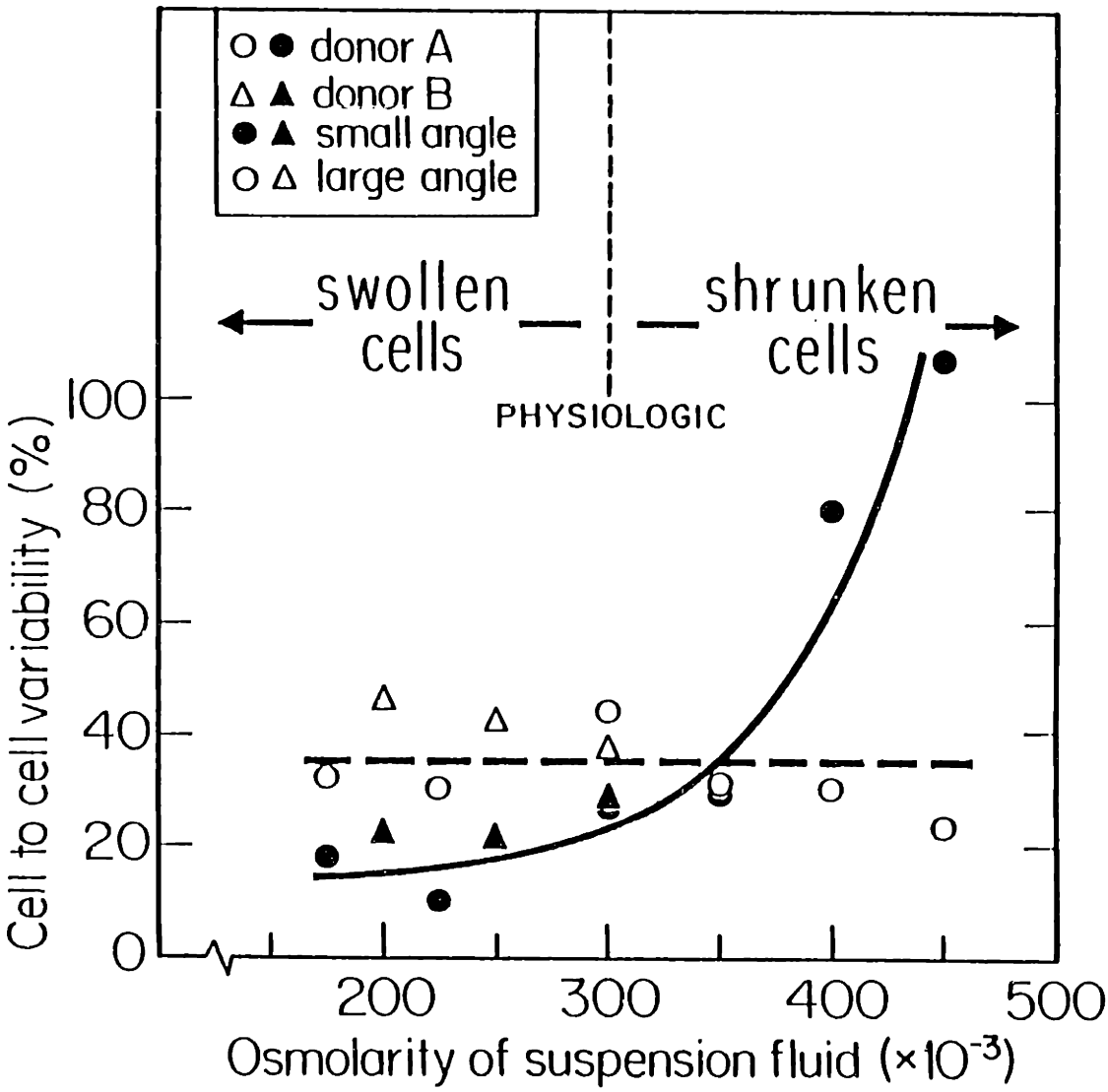

Figure 4.7 Cell-to-cell variability as a function of osmolarity of the suspension fluid for the measurements presented in Figure 4.6

age may affect the intracellular Hb concentration at physiologic condition, the membrane elasticity and membrane permeability. This is believed to be the reason why the cell-to-cell variability increases rapidly with cell volume decrease.

It is of interest to point out at this stage that the fast relaxation time of the correlation functions does not depend on the cellular shape, which was either normally biconcave or, in a small fraction of the cases, slightly crenated. This gives supporting evidence to the statement that membrane motion does not interfere with the fast component of the signal from the RBCs.

4.4.b. MOTION OF HEMOGLOBIN IN SICKLE RBCs AS A FUNCTION OF AMBIENT PARTIAL OXYGEN PRESSURE (Hb-S)

This experiment is no doubt the least sophisticated of all the RBC experiments reported is this thesis. It really was supposed to be the first physiologically relevant study, but it never yielded very clean results as the RBCs showed a much higher degree of cell-to-cell variability than was expected when this experiment was first planned. Nevertheless, I wish to report these experiments, because it does serve as a good illustration of the extend of scatter one obtains on data taken on unselected RBCs. Moreover, the data of this study are not by any means featureless.

The experiment is one in which RBCs are exposed to different mixtures of the two standard gasses: 95% air + 5% CO_2 and 95% N_2 + 5% CO_2. At the time, we did not have the optical multichannel analyzer so that no

measurement was made of intracellular Hb oxygen saturation. The purpose of the experiment was to determine the diffusion coefficient as a function of ambient partial oxygen pressure (pO_2) for sickle RBCs.

Sample Preparation and Sample Holder

Cells of a sickle cell anemia patient are washed three times in the buffer + BSA and resuspended. A mixture of 95%air+5%CO_2 and of 95%N_2+5%CO_2 is passed through water as usual for the humidification of the gas mixture. Immersed in this water container is also a pO_2-electrode. Its output varies linearly between the "nitrogen state" and the "air state". In this experiment, RBCs were equilibrated at 150 mmHg (air), 0 mmHg (N_2) and 8 intermediate partial oxygen pressures for 30 to 45 minutes at 37°C (in later experiments the sample preparation was done at room temperature). The cells were regularly stirred (not continuously like in the later experiments). Measurements were made on about 10 cells in each preparation.

Data and Data Analysis

All reported measurements were done at the small scattering angle. Both single and double exponential analysis was performed on the intensity autocorrelation functions using the delayed and the calculated baseline. The spread on the diffusion coefficient values was very large and much better data were taken later on. Yet, the AC/DC ratio using the delayed and calculated baselines form an interesting picture. They are defined in Eq.2.34 and Eq.2.35 and are rewritten here for easy reference:

$$AC/DC_{delayed} = A_d = \frac{c(\tau=0) - c(\tau=1024x\Delta T)}{c(\tau=1024x\Delta T)} \qquad 4.5$$

$$AC/DC_{calculated} = A_c = \frac{c(\tau=0) - c(\tau=\infty)}{c(\tau=\infty)} \qquad 4.6$$

Results and Discussion

Figure 4.8a. and Figure 4.8b. show the AC/DC ratios for the delayed and calculated baselines respectively as a function of pO_2. Contour lines inclose most of the experimental points and emphasize the main feature of these graphs, i.e. the change in the range over which the AC/DC ratio varies between 45 mmHg and 65 mmHg. In a later section 4.4.f evidence will be presented for cell-to-cell variability in the kinetics of intracellular Hb-S oxygen saturation as a function of a continuously changing pO_2. Occasionally such curves show a very sharp rise at the point of the morphologic change of the sickle RBCs. This is probably related to the prompt change in the AC/DC ratio which was found in this experiment at equilibrium. I will refer back to this result when I discuss this feature in section 4.4.f. At this point, however, it is already clear that a threshold pO_2 and thus oxygen saturation seems necessary for Hb-S to start its polymerization from the biconcave state to the sickled state or its depolymerization in the reverse process.

4.4.c. POSSIBLE AGGREGATION OF HEMOGLOBIN UNDER EXTREME CONDITIONS IN NORMAL RBCs (Hb-A)

There have been reports of the non-ideality and suggestions of possible aggregation of Hb-A in cell free Hb solutions at very high concentration [14,15]. Yet, there was never any evidence for the existence of Hb-A aggregates inside the RBC. Even if Hb-A can form oligomers, it does not aggregate into long rods under normal conditions, though it is known to

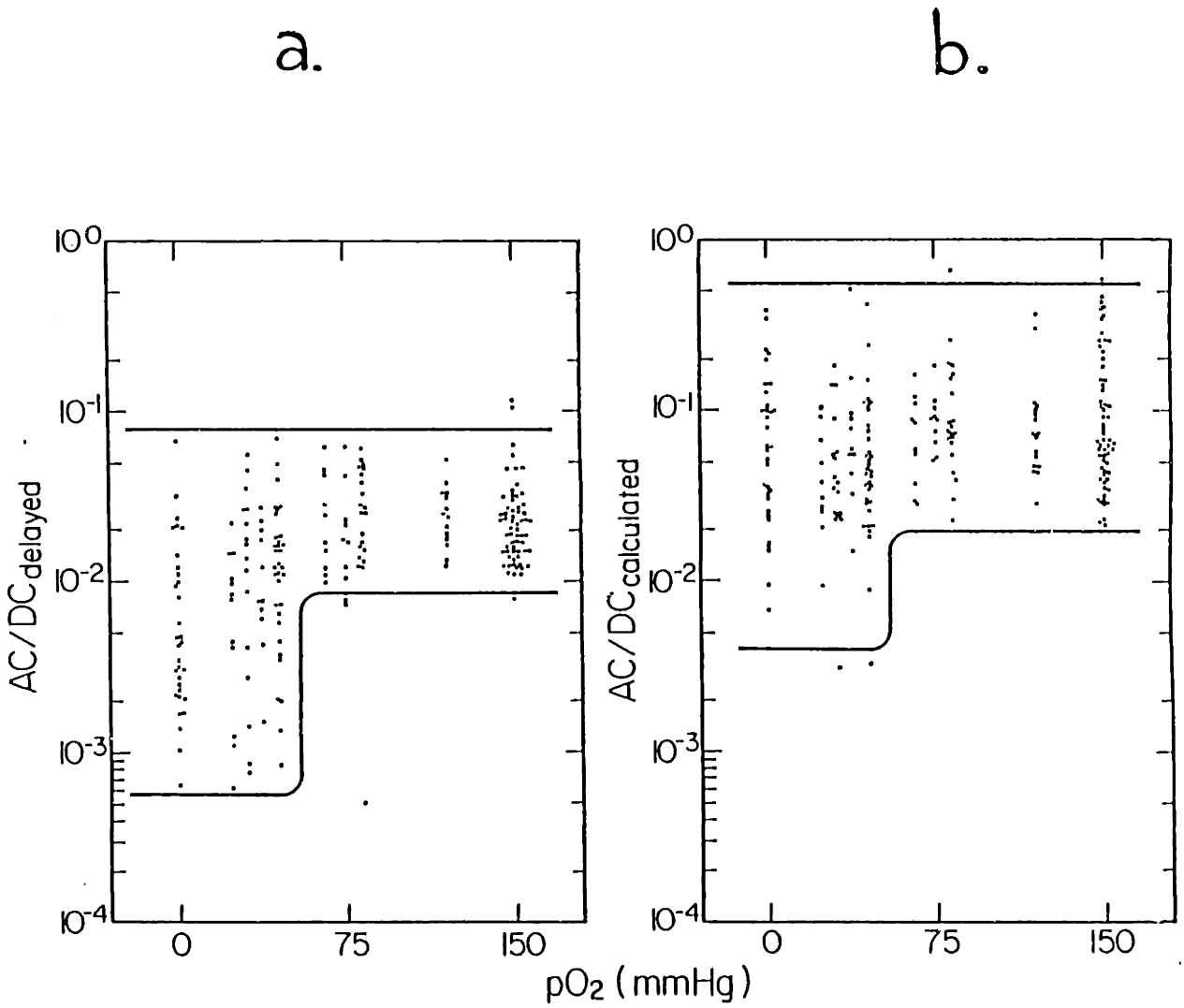

Figure 4.8 AC/DC ratio as a function of the partial oxygen pressure pO_2 of the suspension fluid using the (a)delayed baseline and (b)calculated baseline. Each point represents a different sickle red blood cell. Cells were studied at pO_2 levels of 150mmHg, 120mmHg, 82mmHg, 75mmHg, 66mmHg, 45mmHg, 38mmHg, 31mmHg, 24mmHg and 0mmHg

crystallize under harsh experimental conditions [16]. In the case of Hb-S, the formation of the long Hb-S rods happens via an intermediate nucleation of the Hb-S into small oligomers [17]. We investigated the existence of such small aggregates in normal RBCs.

Sample Preparation and Sample Holder

Normal RBCs are washed and equilibrated with either 95% air + 5% CO_2 or 95% N_2 + 5% CO_2. While MLLSS is being performed on cells from this first preparation, the cell suspension is equilibrated with the other gas mixture. In some cases, this change of oxygen pressure is reversed one more time. Cells from suspensions equilibrated with 95% air + 5% CO_2 are here called "oxy cells", the ones from suspensions equilibrated with 95% N_2 + 5% CO_2 are called "deoxy cells". The cells that are cycled from oxy to deoxy and back to oxy are called "reoxy cells". Samples are exposed to respective gas mixtures for 30 minutes to 3 hours. The sample holders were microcapillary tubes. The blood was taken from 3 normal donors.

Data and Data Analysis

MLLSS was done on 138 normal RBCs. The average diffusion coefficient $\bar{D}$, the fast diffusion coefficient from a double exponential fit D_f and the AC/DC ratio were analyzed in single exponential fits from intensity auto-correlation functions measured at the small and the large scattering angle. The small scattering angle varied between 30° and 33° and the large angle between 134° and 141° depending on the alignment of the day. I feel it is not worth giving a table of all the values. Rather, I present the average values for $\bar{D}$ and D_f and the distributions $\Delta\bar{D}$ and ΔD_f taken over all cells prepared in a certain way. The results are grouped in the table displayed

Cell Type	# of cells	$\bar{D}$ large angle (cm^2/sec) $x10^{-8}$	$\bar{D}$ small angle (cm^2/sec) $x10^{-8}$	D_f large angle (cm^2/sec) $x10^{-7}$	D_f small angle (cm^2/sec) $x10^{-7}$
OXY	52	3.3 ±0.3	3.3 ±0.6	4.2 ±1.5	1.9 ±0.4
DEOXY	51	3.1 ±0.3	3.2 ±0.6	4.0 ±1.7	1.6 ±0.4
REOXY	35	3.0 ±1.0	2.0 ±0.7	5.4 ±2.2	1.3 ±0.3

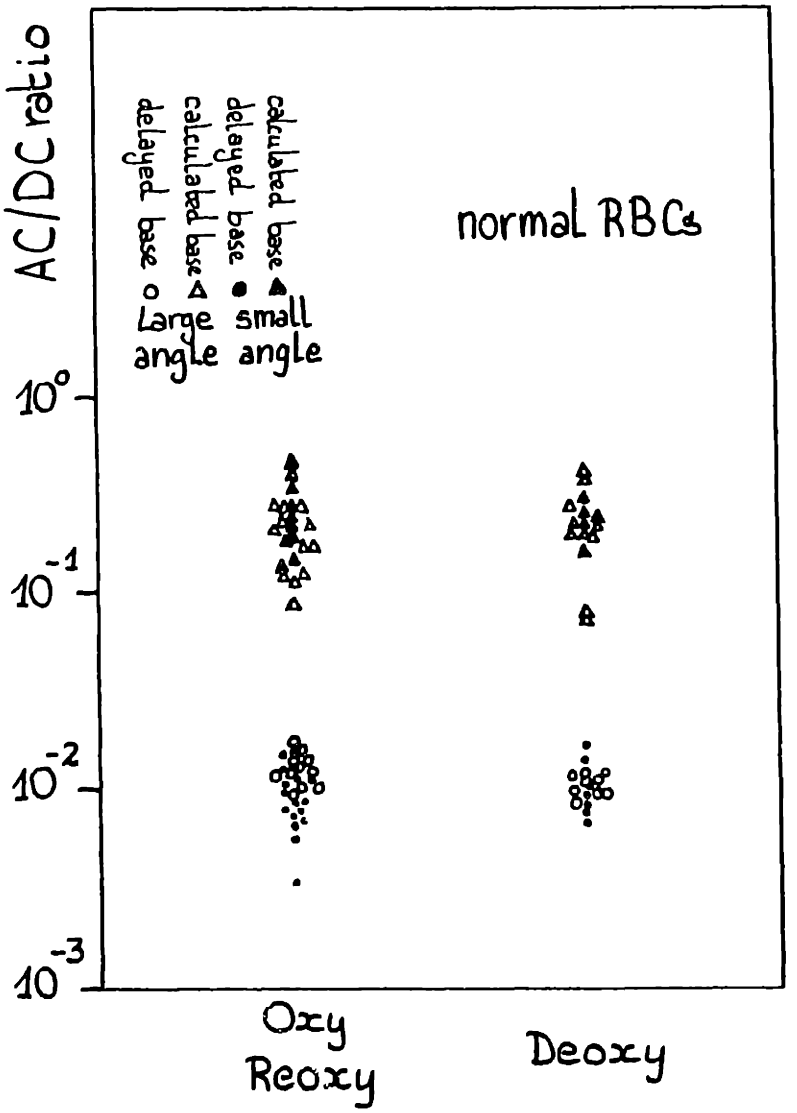

Figure 4.9 (a)Table of the Average Diffusion Coefficient $\bar{D}$ and Fast Diffusion Coefficient D_f and (b)plot of AC/DC ratios determined on fully oxygenated (oxy), fully deoxygenated (deoxy) and reoxygenated (reoxy) Normal Red Blood Cells at forward and backward scattering angle

I also specify the number of cells contributing to the average value. Because we have found, through later experiments, that the AC/DC ratio (see Eq.4.5 and 4.6) is often a more sensitive quantity to the intracellular Hb aggregation, a plot is given of the AC/DC values. This plot is given in Figure 4.9b. Each point corresponds to the average value of AC/DC for one sample preparation (one day, one gas mixture, one equilibration time of the sample with the gas mixture). The ratios are given for both the delayed and calculated DC level (intermediate and far baseline).

Results and Discussion

The data show no significant difference between normal oxy and normal deoxy RBCs, nor on average, nor in the degree of spread about the average. Though some numbers point in the direction expected in the case of the formation of some small oligomers in the deoxy cells, the data are not decisive due to the large spread in data taken on different cells in one sample preparation. The conclusion of this experiment is thus simple: within the accuracy of the MLLSS experiments at this stage, no evidence is found for the existence of small aggregates in normal deoxy RBCs compared to normal oxy RBCs.

4.4.d. IRRADIATION DAMAGE ON NORMAL RBCs (Hb-A)

In the course of the kinetic experiments that are presented below, the RBCs are sometimes exposed to either the He-Ne laser light or to the microscope halogen lamp for extended periods of time. It is therefore necessary

to make sure that the cells are not damaged by the radiation that they receive. Here, I present data demonstrating that the cells are damaged by very strong radiation and other data that prove that the cells are not affected by the radiation levels to which they are exposed during normal experiments.

Sample Preparation and Sample Holder

These experiments were performed on normal RBCs. They are placed in the microcapillary sample holder. The absorption measurements and measurements under the red laser (He-Ne laser 6328 A) are done as described above. The cells that are exposed to the green laser (Argon laser 5145 A) were put into microcapillaries and then slowly passed through the laser beam. After this irradiation, they are placed in the MLLSS set-up for inspection of Hb aggregation.

Data and Data Analysis

A first set of data deals with laser irradiation. Figures 4.10.a and 4.10.b show correlation functions taken on cells irradiated with red and green laser respectively. The approximate amount of irradiation R received is marked on the curves. It is calculated simply by

$$R = \frac{\text{Power of light source x Exposure time x Area of cell}}{\text{Area of illuminated region}}. \qquad 4.7$$

For the green laser, the illuminated region has the area of the unfocussed laser beam and the power was 200 mWatts. For the red laser, the area is about 5 μm^2 and the power is about 3 mWatts. Clearly, the correlation functions are not affected by the red laser illumination. The R values shown correspond to 3 hours of uninterrupted illumination, which is much

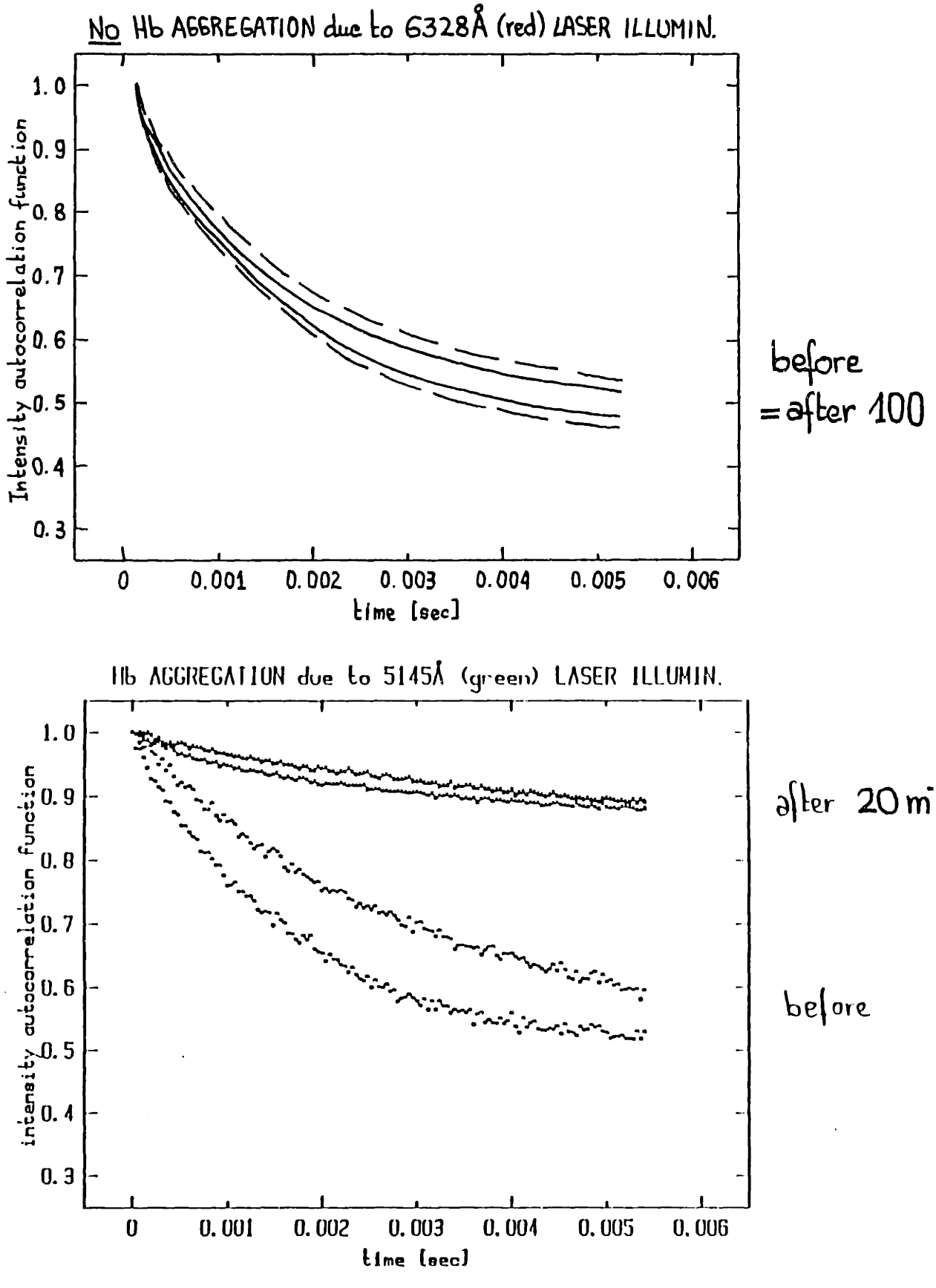

Figure 4.10 Intensity Autocorrelation Functions taken on normal red blood cells before and after irradiation with a He-Ne laser (top) and an Argon laser (bottom). The He-Ne laser does not and the Argon does induce aggregation of the intracellular hemoglobin

longer than the exposure times used in real experiments. In the case of the green laser, however, the correlation functions demonstrate extensive Hb aggregation after exposure times of 20 seconds to the green laser. The big difference is of course due to the strong absorption of the Hb in the green wavelengths; that is why our blood looks red.

A second set of data relate to the effect of the microscope halogen light on the RBCs. The spot size after focusing with the condenser lens onto the microscope stage is about 3 mm^2. The power was 5 Watts, which is higher than in most absorption experiments. Figure 4.11.a gives the absorption curves after 1 to 212 minutes of exposure to this white light. They are very similar. On the other hand, Figure 4.11.b shows absorption curves for cells exposed to 9 Watts for 0 to 73 minutes. The area of the curves clearly decreases. Exposure time and relative area under the curve are marked next to each curve.

Results and Discussion

The doubling of the incident halogen lamp intensity from 5 to 9 Watts obviously makes a big difference. I did not investigate the decrease of the area of the absorption curves any further, but I assume that the membranes of the cells become leaky when exposed to light that is too bright or too hot. In this case, Hb slowly leaves the cell and the absorbed intensity decreases thus making the Hb specific portion of the absorption curves disappear.

The irradiation levels that RBCs are exposed to under normal working conditions are not higher than the levels that were shown to be harmless to the RBCs in this study, either because the power of the light source was

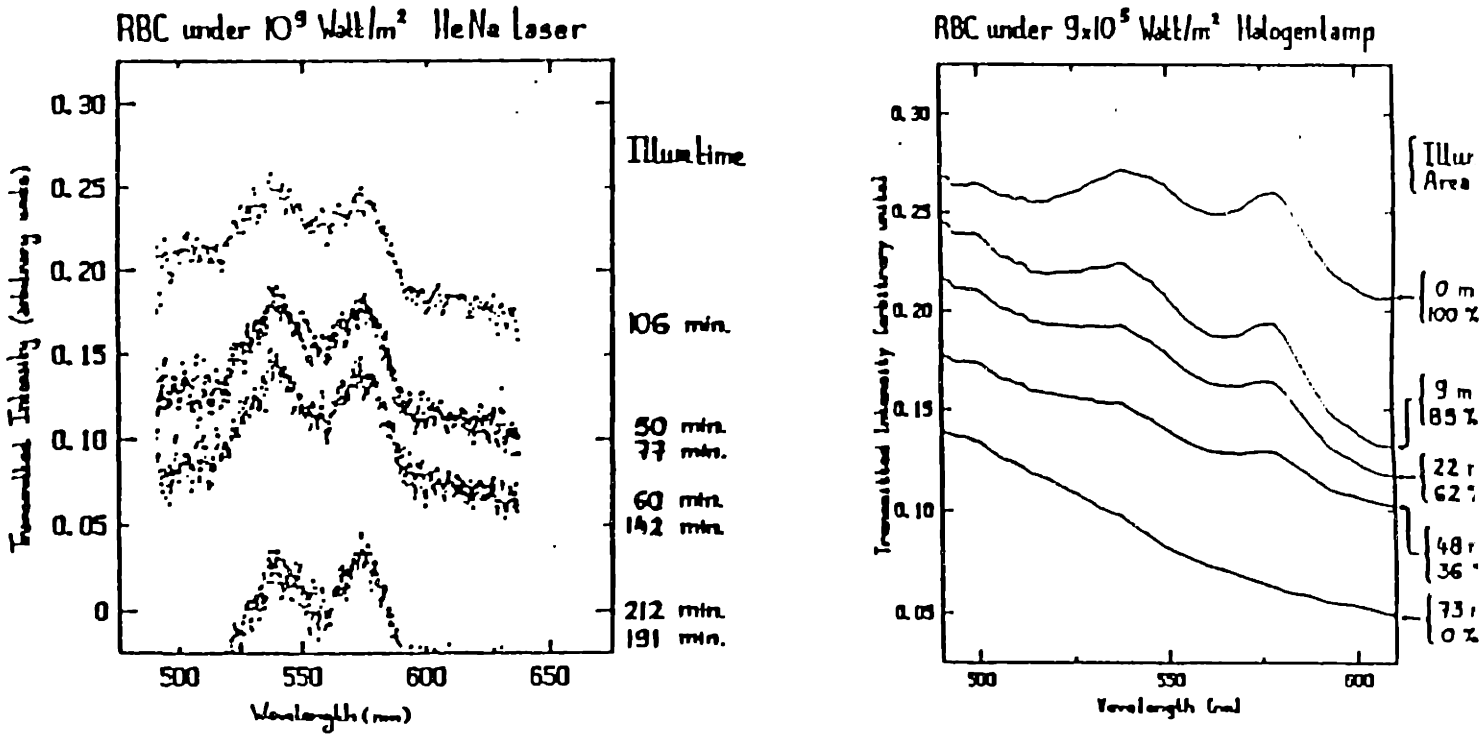

Figure 4.11 Absorption spectra taken on normal red blood cells as a function of the time of exposure to the focussed He-Ne laser (left) and the microscope white light source (right)

lower than the ones proven to be "safe", or because the incident light was blocked off while not performing measurements. All experiments presented in the next sections are thus not detectably affected by the illuminating source. Special attention should always be given to this problem, especially under focussed white light illumination.

4.4.e. THE KINETICS OF HEMOGLOBIN DEPOLYMERIZATION IN SICKLE RBCs (Hb-S)

The time course of intracellular depolymerization of hemoglobin-S aggregates is directly observed using MLLSS in single sickle red blood cells upon slow reoxygenation. The average diffusion coefficient as well as the fraction of hemoglobin aggregates that have intracellular mobility are determined. The oxygen saturation of the hemoglobin of the same cell is measured by single-cell absorption spectrophotometry. Combining the results obtained with these techniques and information on the cellular morphology, a model is proposed for the depolymerization process of hemoglobin inside single erythrocytes as they transform from the fully sickled to the normal biconcave shape upon reoxygenation. Not only is the study of the kinetics of intracellular Hb-S aggregation at the single cell level novel, but moreover are there only very few studies that deal with the deoxygenation of sickle cells. We feel this work shed some new light on the understanding of Hb-S polymerization. This work was accepted for publication and should appear soon (J.Peetermans, I.Nishio, S.Ohnishi and T.Tanaka, Light scattering study of depolymerization kinetics of sickle hemoglobin polymers inside single erythrocytes, Proc.Natl.Acad.Sci.USA, accepted for publication).

Sample Preparation and Sample Holder

Blood was taken from the sickle cell patient and from a normal donor and washing of the cells was done as usual. The cell suspensions were equilibrated with the 95% N_2 + 5% CO_2 humidified gas mixture and placed into the microcapillary sample holder. Soon after we started using these Critosealed capillaries, we realized that the Critoseal is leaky to air. Thus, the enclosed deoxygenated cells are slowly reoxygenated as oxygen molecules from the air diffuse from the edge of the capillary into the sample holder. The cells, originally fully sickled, regain a normal biconcave shape. Near the leaky Critoseal edge of the microcapillary, the morphologic recovery of the cells takes on the order of minutes, whereas in the center of the capillary recovery takes about one day. These time scales are in agreement with the estimates for the time necessary for oxygen molecules to diffuse over the corresponding distances (0.1 mm and 1.5 cm respectively). The distance between the edge of the microcapillary and the position of a cell inside the microcapillary thus determines the time span of the experiment in which we monitor Hb depolymerization upon Hb reoxygenation. In one experiment, all studied cells were chosen in a region of diameter L no more than 100 μm. The diffusion coefficient D of oxygen in water is 2×10^{-5} cm²/sec. Thus it takes $L^2/D = 5$ sec for the oxygen to diffuse across the field of diameter L. The experiments are performed at distances anywhere from 5mm to 3cm away from the leaky edge. The time required for the partial oxygen pressure to reach 50% of the final value (pO_2 for air is 150 mmHg) is thus at least 4 hours. It can therefore be assumed that all cells under study are exposed to the same ambient partial oxygen pressure during the time required for obtaining an intensity autocorrelation function or an absorption spectrum from each cell (about 3

minutes for 5 cells). This is in fact a better and better assumption as time goes on. Appendix IV-2 gives the appropriate diffusion equation and a plot of its solution at 5mm from the edge.

Data and Data Analysis

The absorption spectra are analyzed as described in Chapter 3. Though they are recored from each cell under study in a given experiment, only the spectra taken on one normal and one sickle RBC are shown in Figure 4.12. Section 4.4.f will go into much more detail on absorption data such as these. From series of spectra such as in Figure 4.12, the oxygen saturation as a function of time is derived for the reoxygenation experiment and plotted in Figure 4.13.

Figure 4.14 shows some of the correlation functions taken on an individual normal and on an individual sickle RBC. The functions, all normalized to the first channel, are recorded at different times during the reoxygenation of the sample. Every time a correlation function is taken, the oxygen saturation level of the Hb inside the cell is measured; it is indicated on the correlation functions of Figure 4.14. The functions are analyzed using Eq.2.24 and Eq.2.25. Because there is undoubtedly polydispersity in the samples, I call the diffusion coefficient $\overline{D}$ (average D). $\overline{D}$ and the intensity ratio $R = I_m/(I_m+I_{imm})$ are plotted for four normal RBCs in Figure 4.15.a and for five sickle RBCs in Figure 4.15.b. These cells were not necessarily located at the same distance from the edge of the microcapillary. They were part of different experiments, some close to the edge of the capillary (short recovery times) and some far from the edge (longer recovery times). To plot all the results on one graph with the same horizontal axis, the axis for each experiment was scaled in the

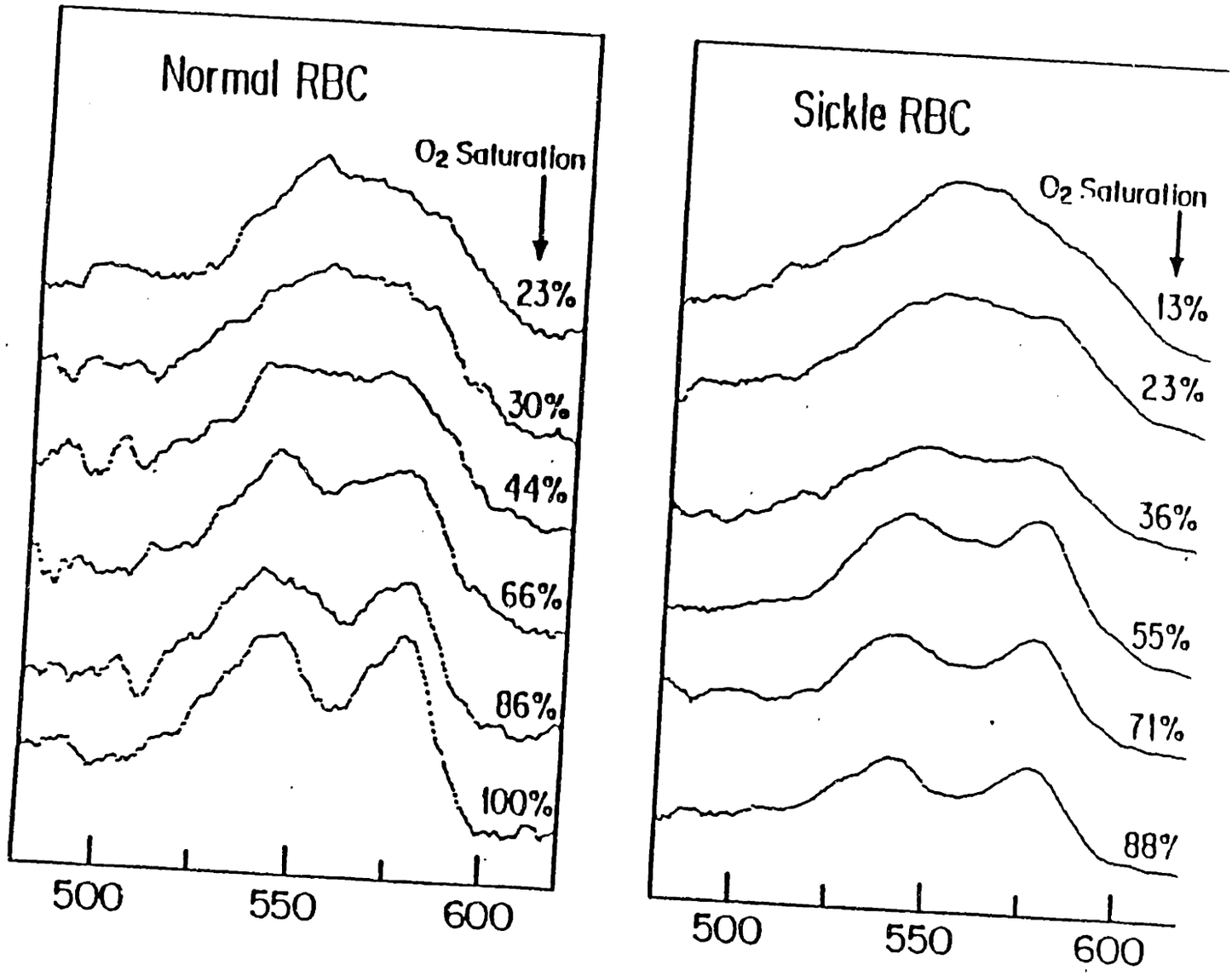

Figure 4.12 Absorption spectra taken on single Normal cells (left) and Sickle cells (right) during a slow reoxygenation experiment (top to bottom). The fitted oxygen saturation value is marked on each curve

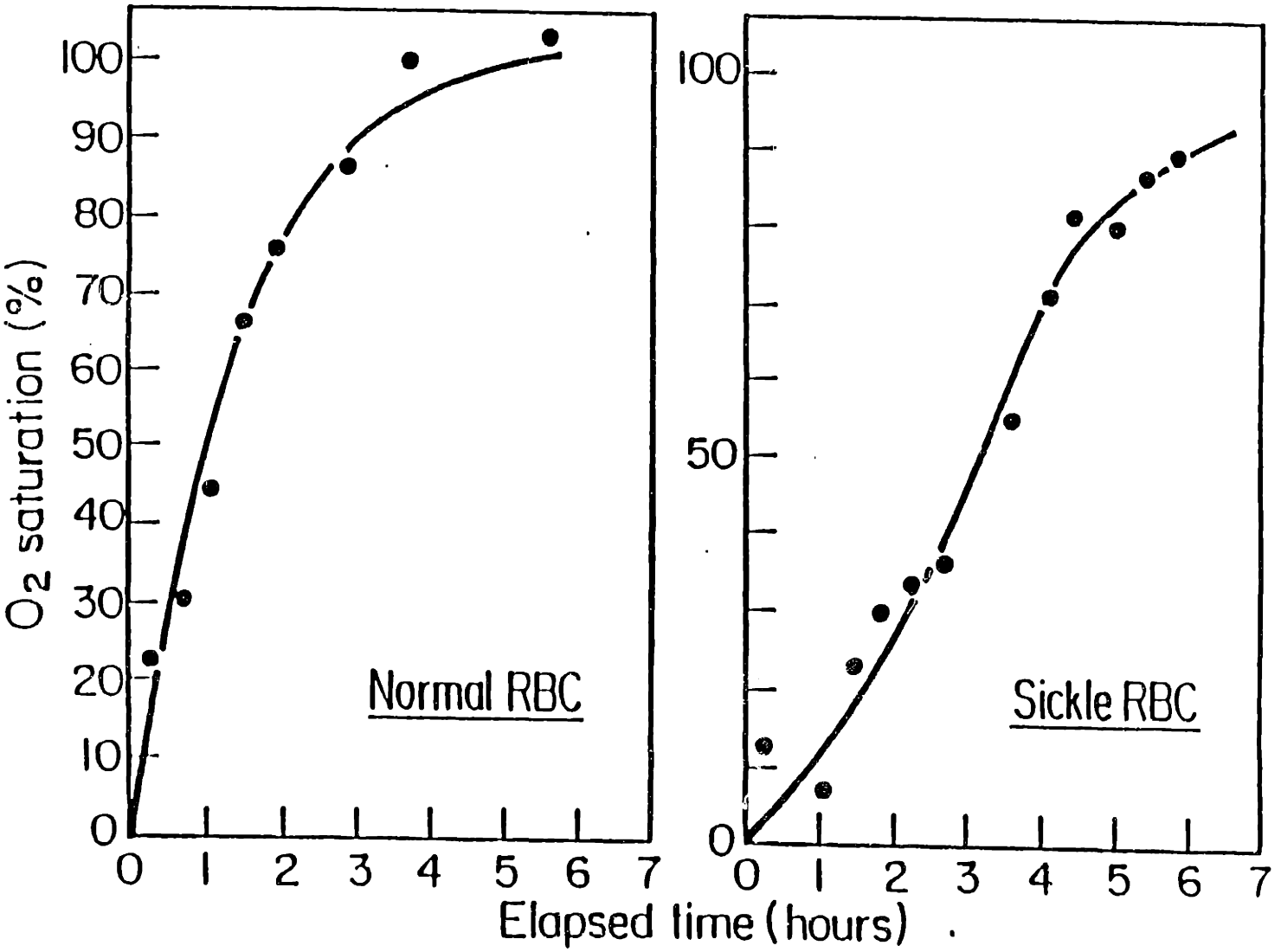

Figure 4.13 Oxygen Saturation of Intracellular Hemoglobin measured as a function of time in the slow reoxygenation experiment presented in Figure 4.12 on single Normal and Sickle red blood cells

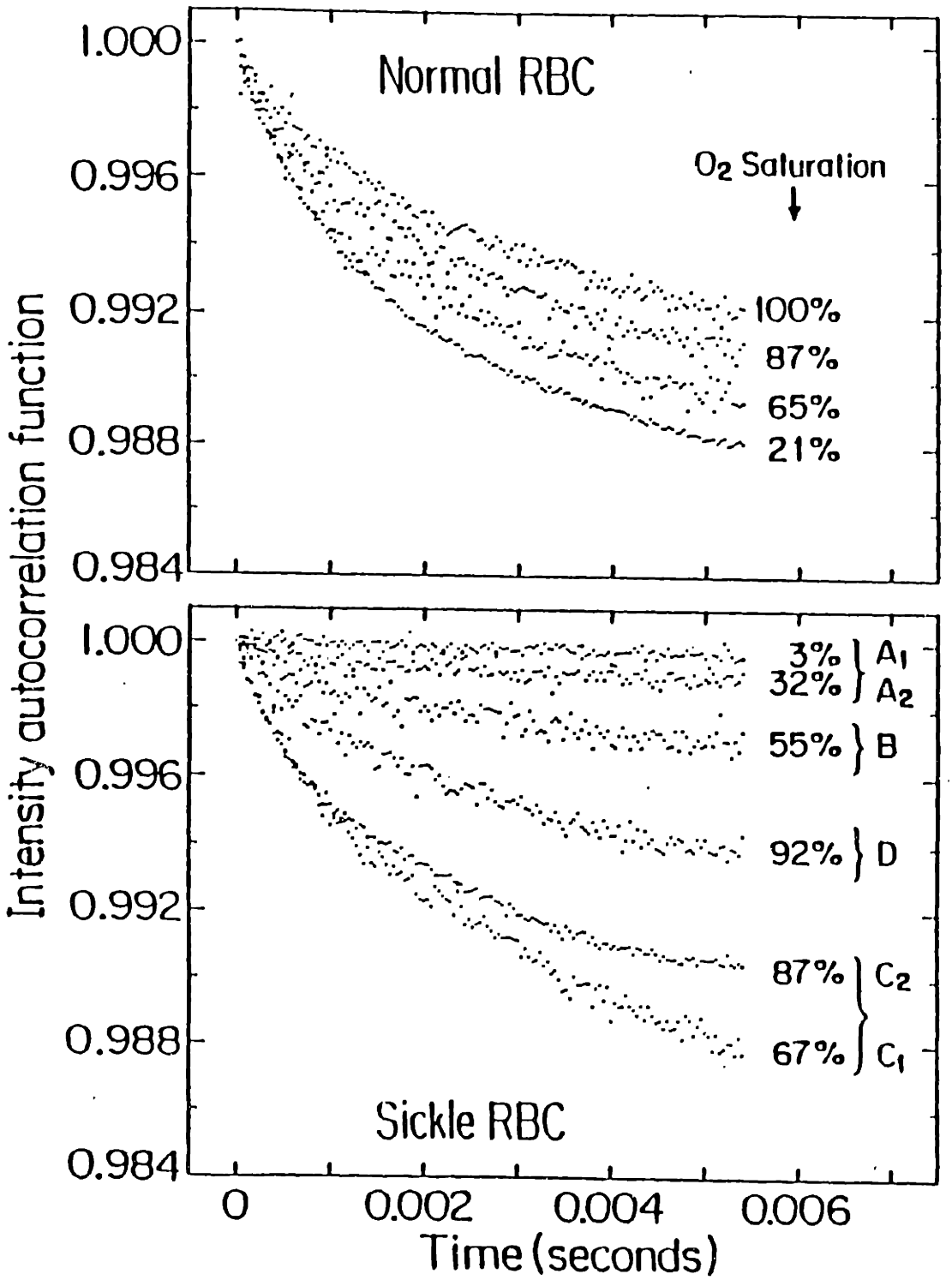

Figure 4.14 Intensity Autocorrelation Functions taken on the red blood cells of Figures 4.12 and 4.13. The oxygen saturation level determined at the time each correlation function was taken, is marked next to each function. The lettered regions are marked for easy reference in the discussion of the data

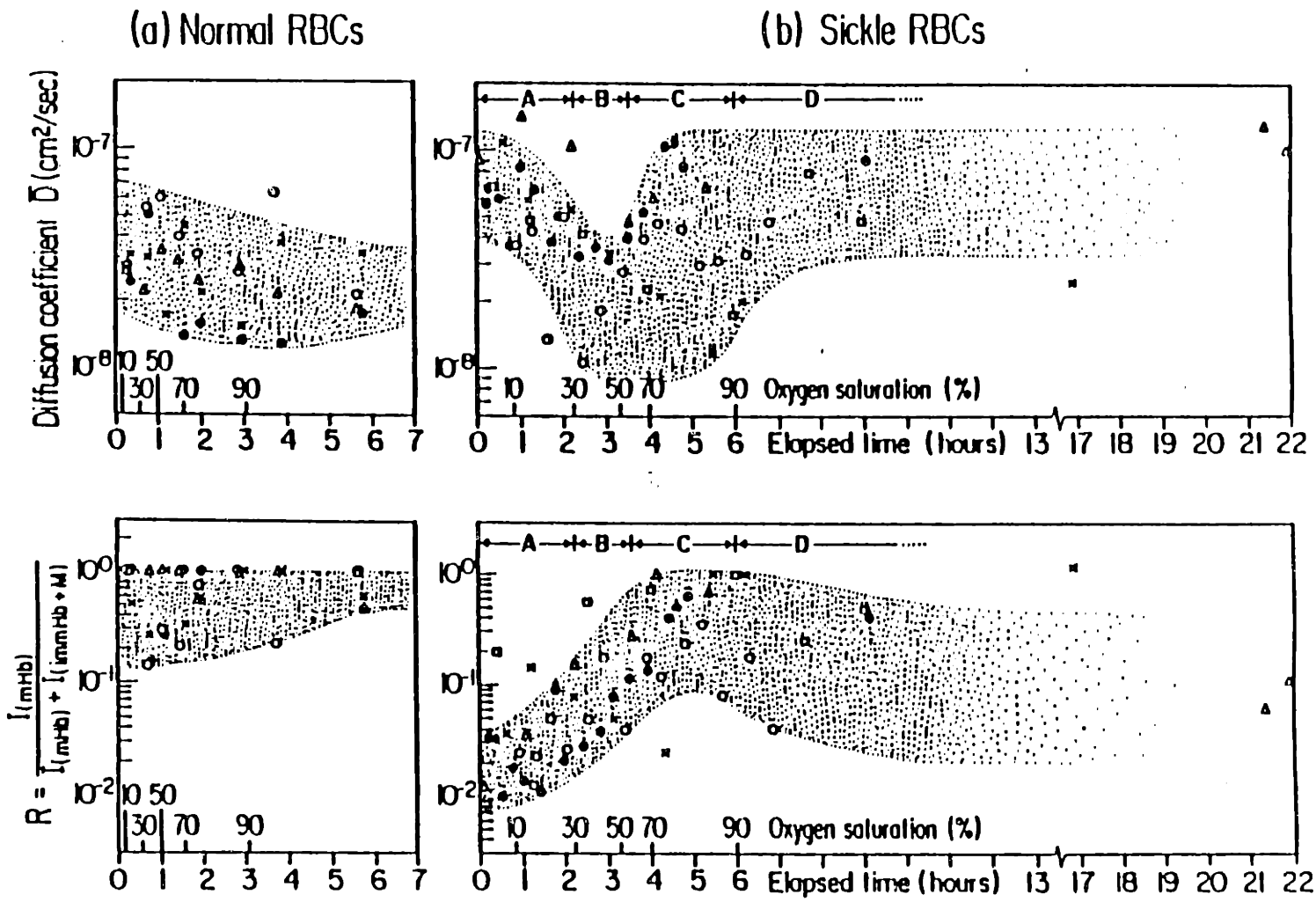

Figure 4.15 Diffusion Coefficient $\bar{D}$ and Intensity Ratio R extracted from correlation functions such as the ones in Figure 4.14. Each symbol indicates another single red blood cell The horizontal axis shows the elapsed time after the cells were placed inside the microcapillary. The parallel horizontal axis gives the approximate oxygen saturation level taken from Figure 4.13

following way. If the distance from the edge of the capillary to the location of the cells is L, then it takes oxygen molecules a time L^2/D to diffuse over this distance L, where D is the diffusion coefficient for oxygen molecules in water ($D \sim 2.0 \times 10^{-5}$ cm^2/sec). Therefore, if the partial oxygen pressure pO_2 has reached a certain value at a time t_1 and a distance L_1 from the edge of the capillary, the same oxygen pressure should be reached at a distance L_2 in the capillary at a time $t_2 = (L_2/L_1)^2 t_1$. Scaling the time axis according to this rule yields a common axis on which any given point corresponds to one given oxygen pressure for all the cells. The shaded regions are a guide to the eye and accentuate the trends found in individual cells. Figure 4.16 shows the diffusion coefficient $\overline{D}$ and the relative intensity R as a function of time for just one sickle RBC. Whereas in Figure 4.15 all data points are averaged over our several measurements, here individual measurements are shown in order to demonstrate that the scatter decreases with time. This trend follows the progressive increase of the relative scattered intensity of the mobile species as the Hb in the RBCs is being reoxygenated. The development in the many-cell curves of Figure 4.15 is very clear in the single cell curves of Figure 4.16. The parallel horizontal axis in both figures is taken from the full line traced through the experimental points in Figure 4.14.

Results and Discussion

In this section, an interpretation of the general trends in the reoxygenation data is given based on the combination of the light scattering data, the absorption spectra measurements and the morphologic information. After that a comparison is made between the data on normal RBCs and the data on sickle RBCs. Also, the relation between morphologic recovery and

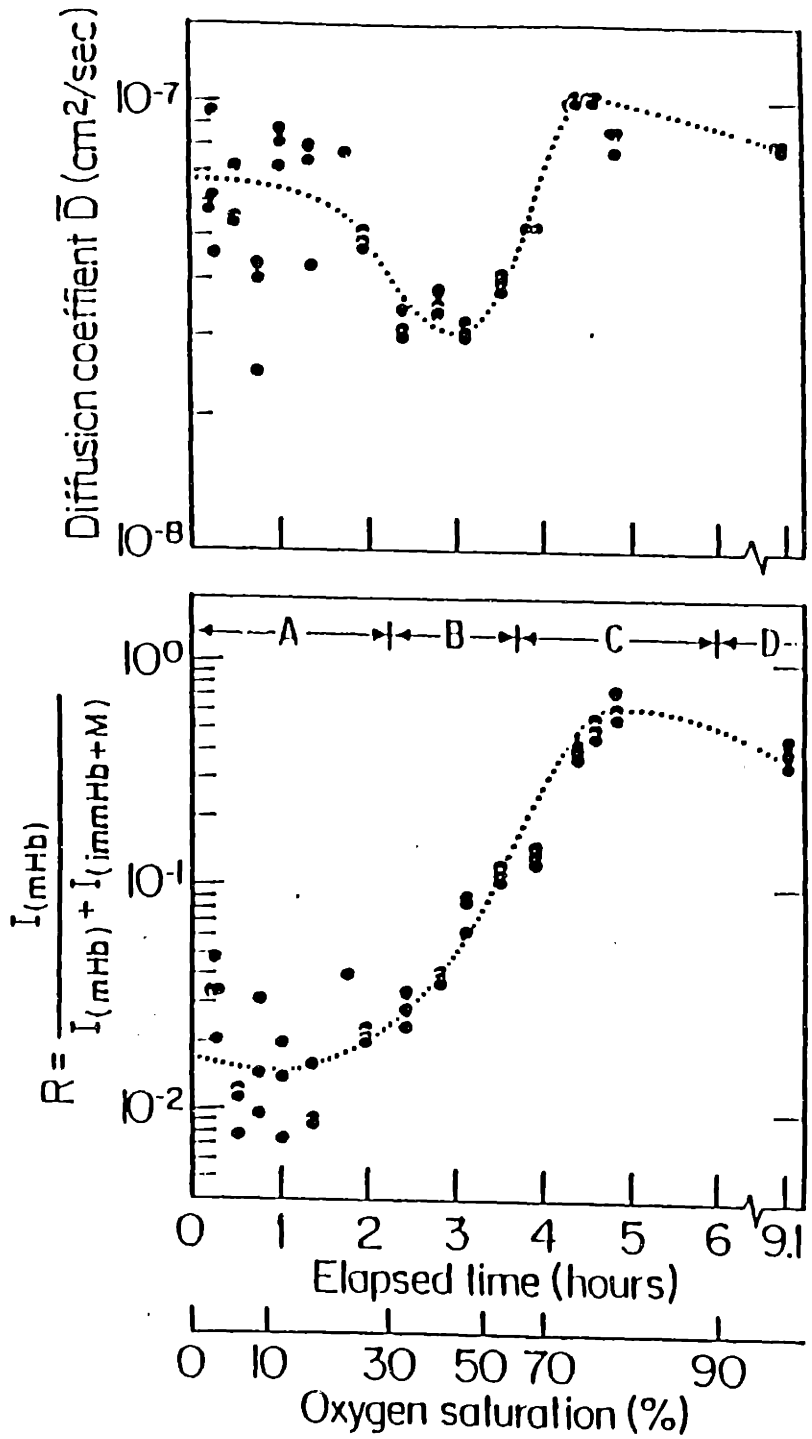

Figure 4.16 Diffusion Coefficient $\bar{D}$ and Intensity Ratio R extracted from correlation functions taken on one red blood cell. The dotted line emphasizes the trends found in slow reoxygenation experiments

Hb reoxygenation is commented on.

- i. Initial stage (stage A)

The time region marked as A in Figure 4.15 and Figure 4.16 corresponds to correlation functions A1 and A2 in Figure 4.14 and represents the stage at which the oxygen saturation is less than 35% (see Figure 4.13). Morphologically, the cells are strongly sickled and no sign of desickling is observed between 0% and 35% oxygen saturation. Correlation function A1 is taken at an oxygen saturation level of 3%. At this low oxygen saturation, a large fraction of the Hb molecules forms aggregates of lengths of the order of the RBC diameter. These aggregates stretch the cells and are totally immobile. Therefore, the amplitude of the fluctuations of the scattered light intensity is minimal. Indeed, the correlation function A1 is almost flat and the relative scattered light intensity from mobile particles, R, is very small. Because of this very small signal to background ratio, the diffusion coefficient obtained from correlation functions such as A1 is insignificant. Values for $\overline{D}$ obtained in this regime therefore show large uncertainty. This is demonstrated clearly in Figure 4.16. Correlation function A2 is taken at 32% oxygen saturation and decays sufficiently to be able to determine $\overline{D}$ in a more meaningful way. Throughout time region A, the spread on $\overline{D}$ is, however, very large and it is not possible from this figure alone to claim that $\overline{D}$ is larger in the 20% to 35% oxygen saturation region than in the subsequent time region. When the measurements made at one oxygen saturation level are averaged, however, and when such curves of $\overline{D}$ versus oxygen saturation are put together for several RBCs, one obtains Figure 4.15. On this figure it is clear that there is a trend for $\overline{D}$ to start out high and subsequently go through a minimum. The large values for $\overline{D}$ obtained in this regime indicate that the only

fluctuations are due to small, fast moving Hb monomers in between the huge, immobile Hb polymers. The presence of a detectable fraction of unpolymerized Hb even at these low oxygen pressures is in agreement with NMR data taken by Noguchi et al. [18]. Figure 4.17.a represents an illustrative sketch for the postulated population distribution P_n at stage A. P_n shows two peaks, one at aggregation number n=1 (monomers) and one at n > N (immobilized aggregates).

- ii. Initial Depolymerization (stage B)

Region B on the time axis is represented by correlation function B in Figure 4.14 and is characterized by an increase of R and an initial decrease followed by an increase of the diffusion coefficient (see Figure 4.15 and Figure 4.16). This stage corresponds to 35% to 55% oxygen saturation (see Figure 4.13). No change in the sickled morphology of the cell is observed. Two important features are characteristic of this regime: the rise of the relative scattering intensity of mobile particles R over approximately one order of magnitude and a noticeable minimum in $\overline{D}$. The significant increase in R indicates an increase in the fraction of moving particles inside the RBC. It is caused by the break down of Hb rods into large, but mobile, aggregates. The diffusion coefficient $\overline{D}$ at first decreases because the average size of the mobile Hb polymers increases from that of the Hb monomers (only mobile scatterers in time region A) to that of large, but mobile Hb rods. When these polymers break down further, however, the average mobile scatterer size decreases and the average diffusion coefficient $\overline{D}$ increases. Since there is no noticeable morphologic recovery at this stage, it is reasonable to assume that some Hb polymers of the size of the RBC itself are still present. Figure 4.17.b represents qualitatively the population distribution function P_n for this time region B.

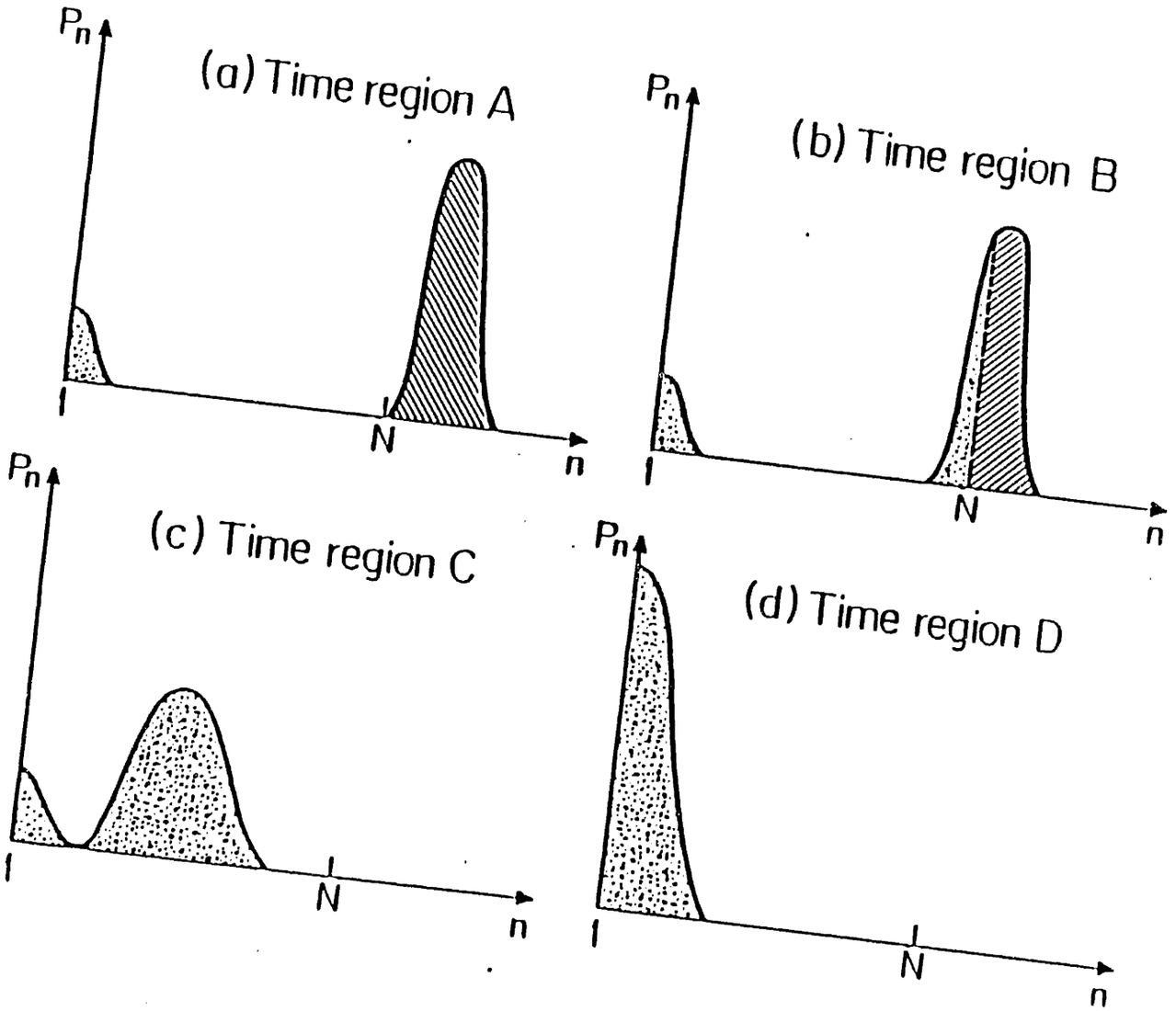

Figure 4.17 Illustrative sketch of proposed Population Distribution P_n of hemoglobin n-mers as a function of time in the slow reoxygenation experiment (from (a) to (d))

- iii. Intermediate stage of Depolymerization and Morphologic Recovery (stage C).

At this stage of the Hb-S depolymerization, which covers the range of oxygen saturation from 55% to 90% (see correlation functions C1 and C2 in Figure 4.14 and time region C in Figure 4.15 and Figure 4.16), the relative intensity scattered by mobile particles reaches a maximum. The first sign of the recovery to the biconcave shape is observed. It may be reasonable therefore to assume depolymerization of the last huge immobile Hb-S rods, which were previously stretching and distorting the RBC. More and more small mobile aggregates are formed. Initially, this results in the further increase of the relative intensity scattered by mobile particles, but eventually this value decreases because the scattered intensity of Hb aggregates decreases as the average aggregate size becomes smaller and the weight averaged aggregation number $\bar{n}_w$ decreases (see Eq.2.33). Thus, R reaches a maximum. It is interesting that the morphologic recovery of the desickling cells, once started, takes place in a very short time, which seems similar to what happens in the sickling process of RBCs [17]. Figure 4.17.c schematically depicts a possible aggregation size distribution function P_n at this stage of depolymerization.

- iv. Reoxygenated state (stage D)

At this last stage (see correlation function D in Figure 4.14 and time region D in Figure 4.15 and Figure 4.16), final depolymerization of the small aggregates of Hb-S molecules takes place. The oxygen saturation levels are above 90%. In this state, the sickle cell has recovered to the biconcave shape, the averaged diffusion coefficient $\bar{D}$ decreases slightly, and the relative scattering intensity R displays a significant decrease. The decrease of R reflects the further breakdown of the small aggregates

and, with it, the further decrease of the scattered intensity. The observed decrease in the diffusion coefficient $\overline{D}$ for the sickle cells in this final depolymerization stage may be associated with differences in the specific volume occupied by a Hb-S molecule in the monomeric and aggregated state. A sketch of the population distribution P_n in region D is given in Figure 4.17.d.

Normal RBCs compared to Sickle RBCs. The normal RBCs show a very different behavior from the sickle cells. The intensity autocorrelation functions in Figure 4.14 do not show the trends found for the sickle RBCs (namely, the relative intensity R first increasing and later slightly decreasing as the oxygen saturation level increases). For the normal RBCs, the average value of R does not change much with Hb reoxygenation and the diffusion coefficient has a downward trend (see Figure 4.15.a). This is in agreement with the known swelling of normal erythrocytes upon deoxygenation [19,20].

Another important difference between the data taken on the sickle RBCs and on the normal RBCs lies in the quantitative results. The intensity ratio R does not go below 0.1 for normal RBCs and, accordingly, repeated measurements of the diffusion coefficient on a distinct cell show little spread. In Figure 4.14, it is very clear that the ratio R covers a much wider range for the sickle cells than for the normal cells. It is, however, difficult to examine the diffusion coefficient $\overline{D}$ through just visual inspection of individual correlation functions such as the ones shown in Figure 4.14. Nevertheless, a minimum is found in $\overline{D}$ for sickle RBCs as was explained in the previous section. For the normal RBCs, the situation is very different. Although some spread is found in the initial slope of the

intensity autocorrelation functions, the range over which this slope varies is smaller than for the functions taken on sickle cells and no minimum in $\overline{D}$ is observed.

In Figure 4.12 the curves for the normal and the sickle RBC are essentially similar to the absorption spectra taken on cell free Hb solutions. The normal cell and the sickle cell were subject to approximately the same oxygen pressure after the same amount of time. Nevertheless, Figure 4.13 shows a marked lag phase for the sickle RBC which is not observed in the case of the normal RBC. This lag may indicate a reduced oxygen affinity of polymerized Hb-S compared to unpolymerized normal Hb, as was suggested elsewhere [21,22].

Relationship between Hb depolymerization and Morphologic Recovery. A sharp rise in the relative intensity R of mobile particles in sickle RBCs, which is a sign of fast depolymerization of Hb aggregates, occurs when the oxygen saturation of the Hb is approximately 55%. The morphologic recovery happens at an oxygen saturation level of about 80%. From deoxygenation experiments, it is well known that sickling takes place at approximately 50% oxygen saturation. This large difference between the oxygen saturation level at which the sickling of the RBC occurs upon deoxygenation and the recovery from the sickled to the biconcave shape occurs upon reoxygenation (in other words, the hysteresis in morphologic recovery), can be due to hysteresis in the sickle cell membrane shape itself or to oxygen affinity changes upon Hb-S polymerization. In the first case, the sickle cell membrane, which is known to be more rigid than the normal RBC membrane [23,24], once sickled, may not return to its normal biconcave shape immediately after the breakdown of large Hb-S polymers. In the latter case, the

Hb-S, once polymerized into very long rods, has a lowered oxygen affinity [21,22] thus making it harder to depolymerize very long rods that stretch the cell, than the shorter rods. Since the elapsed time between the 55% and 80% oxygen saturation level is on the order of one hour, the latter situation is more likely to cause the observed hysteresis. In any case, Hb depolymerization and cellular morphology are controlled by Hb reoxygenation, not necessarily by ambient oxygen pressure. Indeed, in all cells studied, both features show changes at one same oxygen saturation level, not at the same time and thus ambient oxygen pressure in the reoxygenation process. One of the features, the oxygen saturation level at morphologic recovery, is illustrated much more extensively in section 4.4.f.

4.4.f. CELL-TO-CELL VARIABILITY IN OXYGEN SATURATION AS A FUNCTION OF PARTIAL OXYGEN PRESSURE (Hb-A and Hb-S)

The degree of oxygen saturation of hemoglobin molecules within RBCs is determined during slow re-oxygenation using the single cell absorption spectrophotometry described in section 3. The experiment is performed using normal and sickle RBCs. Samples are separated by density to avoid cell-to-cell variability caused by the differences in hemoglobin concentration. Morphologic change of individual RBCs is studied extensively as a function of the partial oxygen pressure (pO_2), temperature, pH, concentration of potential anti-sickling drugs etc. In many experiments, the controlled variable is pO_2 of the medium in which the RBCs are suspended. Exactly speaking, however, it is the degree of oxygen saturation, not the pO_2, that determines the interaction between the Hb molecules, and thus the

degree of Hb-S aggregation. It is a common belief that the oxygen saturation is the same in all individual cells at a given pO_2, but this hypothesis has not been confirmed. For this reason, it is important to carry out direct measurements of the oxygen saturation within individual RBCs. Evidence is presented for cell-to-cell differences in the oxygen saturation curve for density separated normal and sickle RBCs as a function of ambient pO_2.

Sample and Sample preparation

The microcapillary sample holders were used with the slow oxygen leak in the putty used for a seal. Normal and sickle RBCs are placed in there in the deoxygenated state. Since the aim of this experiment is to determine the possible existence of cell-to-cell variations in the rate at which the intracellular Hb is being reoxygenated given a certain ambient pO_2, all sickle cells were density separated. In this way cell-to-cell variations are not merely due to the variations in the extend of Hb-S polymerization due to intracellular Hb concentration differences. The density separation was described earlier. To compare normal and sickle RBCs under exactly the same conditions, the two types of cells are separately washed and then mixed together in the microcapillaries. Because of the morphologic differences between sickle and normal RBCs at very low oxygen pressures, it is easy to discriminate the two types of cells. When sickle cells of the major band are studied, the washed normal and sickle cells are separated on a same density gradient. Using this method, sickle and normal RBCs can be compared in an identical environment: same density, pO_2, pH, osmolarity etc.

All spectra in this study are the average of 5 spectra, each accumulated for 1 second under illumination that is sufficiently weak to allow naked eye observation through the eyepieces (position 4 on the Optiphot).

Data and Data Analysis

The absorption spectra are analyzed as described in section 3. The spectra basically look like the ones shown in Figure 4.14. Only the fitted oxygen saturation values are given here. Figure 4.18 shows the degree of oxygen saturation observed as a function of time from normal RBCs undergoing slow reoxygenation due to diffusion of oxygen molecules from the end of the capillary sample cell into the deoxygenated sample. The three symbols are taken on the normal RBCs of different experiments. Two of them represent normal cells studied simultaneously with sickle RBCs in experiments discussed below. All reoxygenation curves fall in a narrow band (O_2 saturation is 63%±10% at pO_2=35mmHg), indicating small cell-to-cell variability among the normal cells. Therefore, scaling the time axis of different experiments so that the curves taken on the normal RBCs in each experiment fall in the same narrow region, yields a time axis common to all reoxygenation experiments. This was done for the three reported experiments. The solid line approximately traces the average oxygen saturation curve as a function of time. It is the same one in all graphs and I refer to it as the master curve for normal RBCs. This master curve is used to scale the time axis of experiments performed at different distances from the edge of the capillary sample holder. The approximate pO_2 is given parallel to the time axis and is deduced from the oxygen saturation as a function of pO_2 curves found in the literature [11] for normal RBCs. This pO_2 axis is constructed for the master curve for normal RBCs.

Figure 4.19 shows oxygen saturation curves taken on

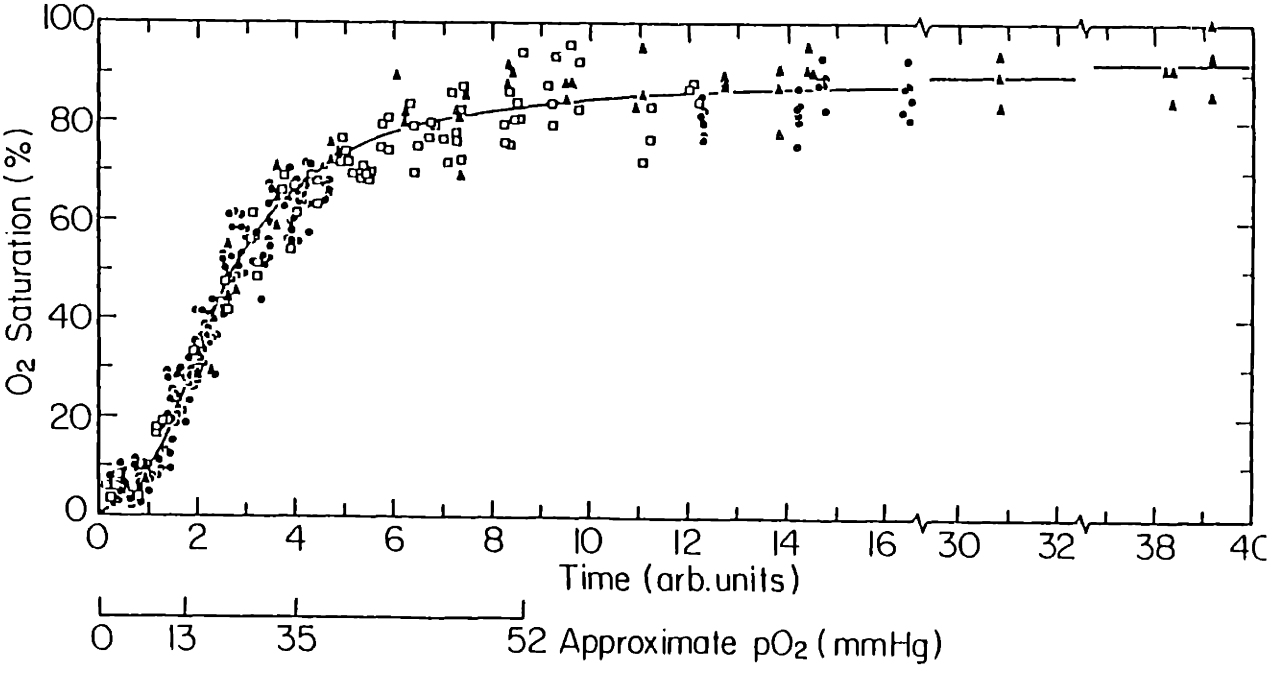

Figure 4.18 Oxygen Saturation Level (%) as a function of time and approximate ambient Partial Oxygen Pressure (mmHg) measured using Single Cell Absorption Spectroscopy on Normal Red Blood Cells (Normal RBCs). Each symbol indicates a separate experiment:
● contains 7 Normal RBCs, □ contains 4 Normal RBCs that were studied simultaneously with Sickle RBCs from the major band in a density gradient (see Figure 4.19) and ▲contains 3 Normal RBCs studied simultaneously with Sickle RBCs from the densest cell region in the gradient (see Figure 4.20). The solid line traces the trend in the experimental points. It is referred to further as the "master curve for normal RBCs"

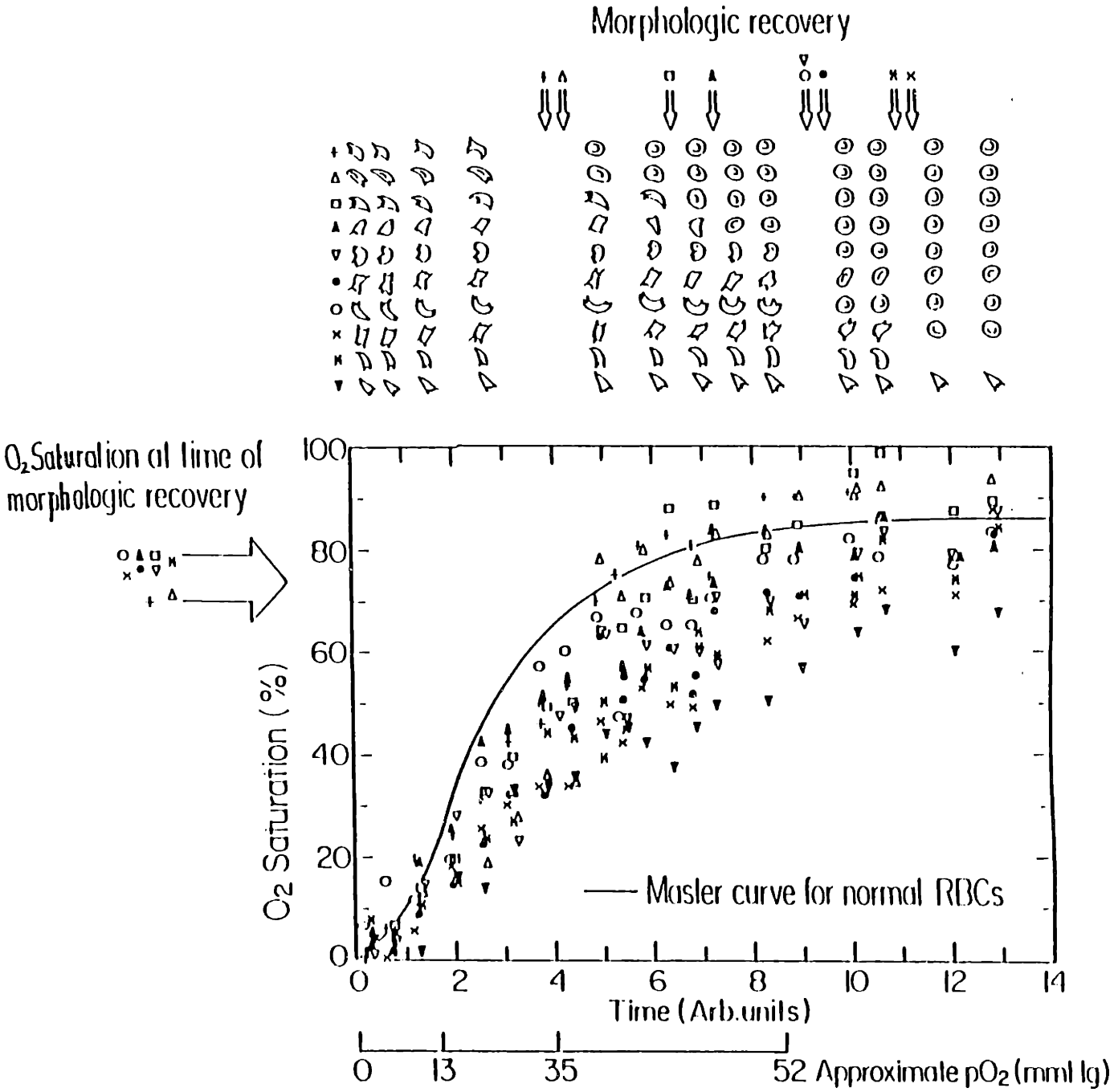

Figure 4.19 Oxygen Saturation Level (%) as a function of time and approximate ambient Partial Oxygen Pressure pO_2 (mmHg) measured using Single Cell Absorption Spectroscopy on 10 Sickle Red Blood Cells from the major band in a density gradient (see Figure 4.2). Each symbol indicates a separate RBC. The solid line is the master curve for normal RBCs. The cell morphology is sketched as a function of time for all 10 sickle RBCs. The sketches are copied from photographs taken throughout the reoxygenation experiment. The approximate pO_2 and oxygen saturation level at the point of morphologic recovery are marked with an arrow for each sickle RBC. It is clear that morphologic recovery occurs in a narrow region of oxygen saturation (70% to 80%) and over a very wide range of pO_2

10 sickle RBCs from the major band in the density gradient. The solid line is the master curve for normal RBCs. The normal RBCs that were mixed with the sickle RBCs in this experiment are shown in Figure 4.18. Clearly, the cell-to-cell variability is much wider (O_2 saturation is 47%±15% at pO_2=35mmHg) for the sickle than for the normal RBCs. Figure 4.19 also shows sketches of the morphology of each cell copied from photograph taken throughout the reoxygenation experiment. An arrow on the abscissa marks the approximate time of morphologic recovery and a corresponding arrow on the ordinate indicates the approximate oxygen saturation level at this recovery time for each cell. It is important to note that morphologic recovery occurs approximately at the same oxygen saturation level of 75% for all cells. This occurs at very different times and at very different pO_2 for each cell.

Figure 4.20 shows the oxygen saturation curve of 10 sickle RBCs from the densest portion of sickle RBCs. The normal RBCs in this experiment are also shown in Figure 4.18 and the solid line is again the master curve for normal RBCs. Careful comparison with the curves for the the sickle cells from the major band (Figure 4.19) shows that on average these denser cells have a lower oxygen affinity than the ones from the major band. One cell seems very much an exception. It will be important to understand the correlation between the low oxygen affinity of these densest RBCs and the irreversibility of some sickle RBC deformation. Cell-to-cell variability is not noticeably different for these densest cells than for the cells from the major band.

In the course of this experiment, we found a very sharp increase of the oxygen saturation at the time of morphologic recovery in a few sickle RBCs. Figure 4.21 shows a pronounced example.

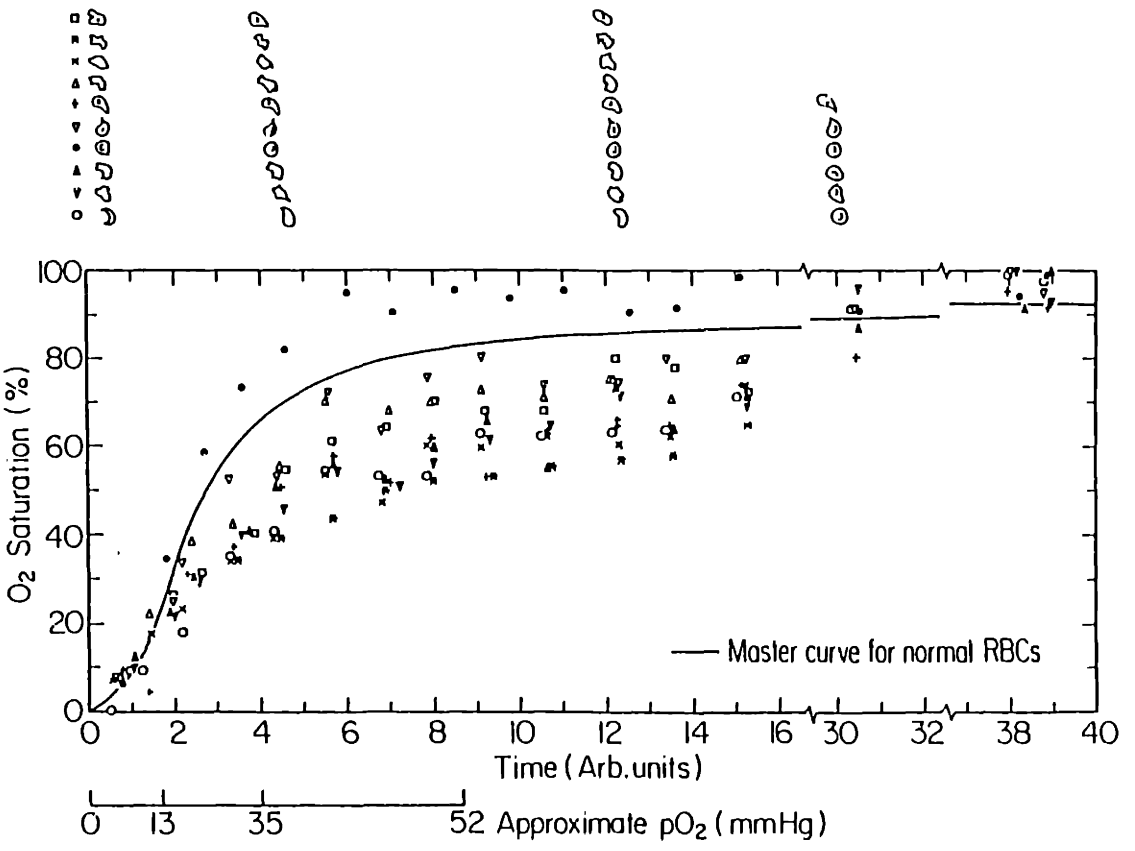

Figure 4.20 Oxygen Saturation Level (%) as a function of time and approximate ambient Partial Oxygen Pressure pO_2 (mmHg) measured using Single Cell Absorption Spectroscopy on 10 Sickle Red Blood Cells from the densest cell region in a density gradient (see Figure 4.2). Each symbol indicates a separate RBC. The solid line is the master curve for normal RBCs. The cell morphology is sketched at a few points for all 10 sickle RBCs

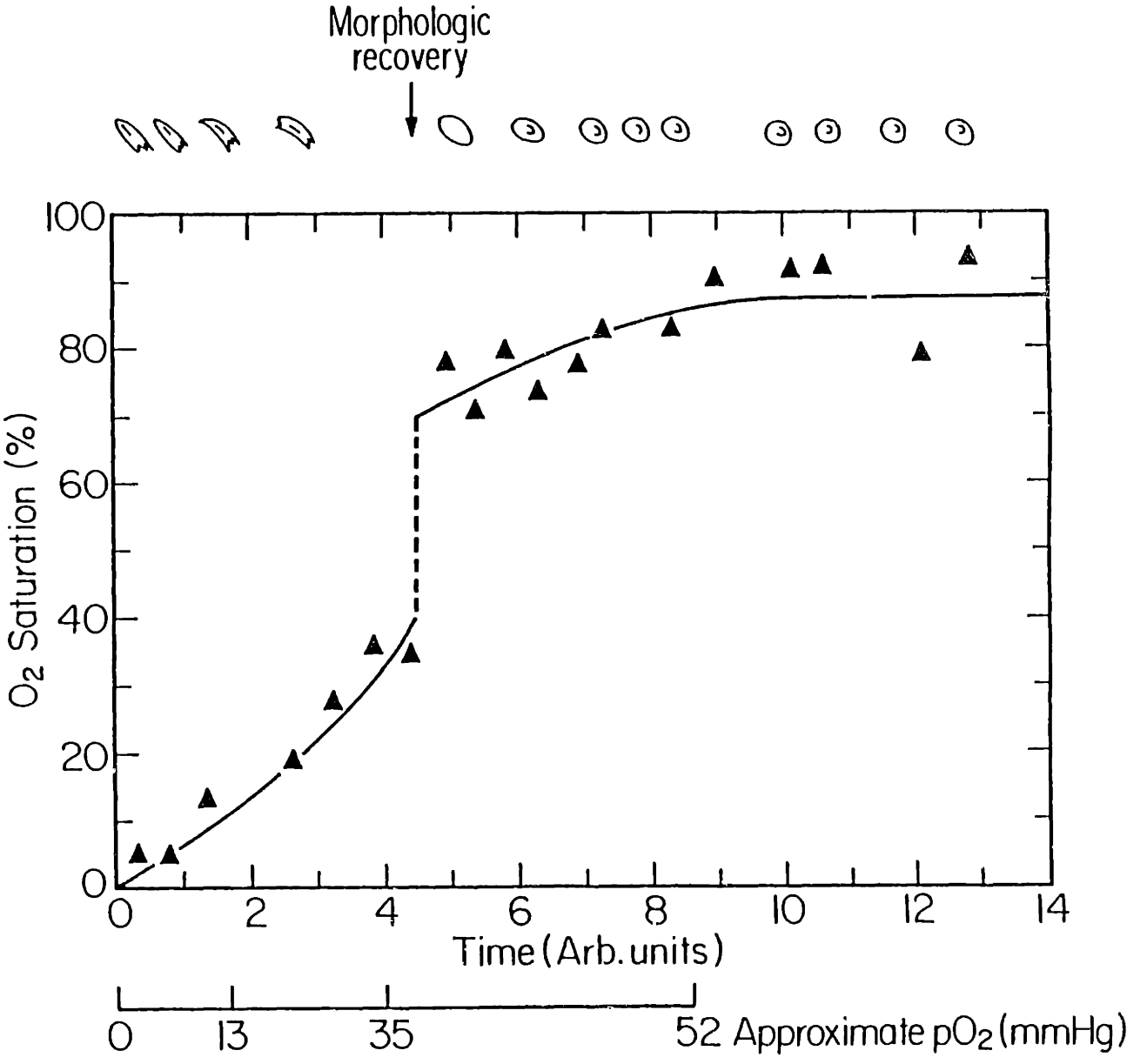

Figure 4.21 Oxygen Saturation Level (%) as a function of time and approximate ambient Partial Oxygen Pressure pO_2 (mmHg) measured using Single Cell Absorption Spectroscopy on 1 Sickle Red Blood Cell from the major band in a density gradient (see Figure 4.2). The cell constitutes a clear example of the sometimes occurring abrupt jump in the oxygen saturation at the pO_2 of morphologic recovery. The cell morphology is sketched as a function of time

This jump in the oxygen saturation is associated with the morphologic recovery of the RBC, which is believed to be caused by the dissociation of Hb-S. It occurs mostly in cells for which the rate of Hb reoxygenation with increasing pO_2 is initially slow.

Results and Discussion

It is demonstrated here that among the sickle RBCs there is a large cell-to-cell variation of the degree of oxygen saturation at a same pO_2, even for sickle RBCs of one density. It is also proven that the morphologic recovery is determined by oxygen saturation rather than by pO_2. This study clearly shows the importance of single cell experiments and how they can lead to different conclusions from the measurements of a quantity averaged over many cells. I think the cell-to-cell variation described here was totally unexpected in the field of sickle cell anemia research.

A possible explanation for this feature is the following. Hb-S polymerization is nucleation controlled. The extended rod formation, once a nucleus is made, may happen at a rate much higher than the rate of nucleation. Thus, if only few nucleation sites are formed upon deoxygenation of the RBC, few very large Hb-S rods can grow. If more nucleation sites are simultaneously formed, the Hb-S may aggregate into fewer, less long rods. This is then the reason for the diversity in the sickled cell shape: the extend and orientation of the rods varies from cell to cell and from sickling to sickling even for one same cell. Since oxygen affinity seems to decrease with Hb aggregation, the hysteresis which was already mentioned in section 4.4.e (Relationship between Hb depolymerization and morphologic recovery), may be stronger in the cells with fewer, longer Hb-S rods. The

rate of nucleation is higher in more concentrated cells, but in cells of the same density, random local density fluctuations can cause cell-to-cell variations in the extend of Hb-S polymerization.

The jump of oxygen saturation found in some cells can possibly be explained in the same way. Though I do not have at this point evidence to prove it, my feeling is that the larger cells and the very "strongly sickled" ones are better candidates for showing a discrete jump in the oxygen reoxygenation curves. Both these cells can contain very long Hb rods. This feature needs further investigation. First of all, the existence of the jump has to be demonstrated more convincingly. Its sharpness and reversibility should then be investigated before the possibility of a phase transition can be seriously considered.

4.4.g. REVERSIBLE OXYGENATION OF RBCs IN FLOW CELL (Hb-A)

So far the experiments in which cells were exposed to variable conditions were the ones in which the deoxygenated suspension buffer was slowly reoxygenated due to the uncontrolled leak in the Critoseal at the edge of the microcapillaries. Obviously, it would be interesting to be able to expose one same cell to changes in suspension buffer other than partial oxygen pressure, and to do so in a reversible way. Here, I present data demonstrating the ability of the flow set-up to provide these features.

Sample Preparation and Sample Holder

Normal RBCs are washed as usual and placed in the flow cell to which they are anchored using the poly-l-lysine coating. One syringe on the infusion pump is filled with fully oxygenated buffer, the other one with fully deoxygenated buffer. Only a small drop of the poly-l-lysine is placed on the bottom half of the flow cell. In this way, when the deoxy buffer flows over the oxygenated cells, the oxygen released by the cells does not create a lag time in really exposing the cells to a deoxy environment and vise versa when the oxy buffer flows over deoxygenated cells. The flow rate is 0.078 cc/min.

Data and Data Analysis

The first experiment is designed to prove that the flow does not create artifacts in the data. In the flow cell experiments that study several cells, the cells are chosen in at most one and a half microscope fields at the 32x magnification. Therefore, cells were chosen in two microscope fields and studied in the order marked on the photographs shown in Figure 4.22. One deoxy to oxy and back to deoxy cycle is shown for each of the 5 cells in this run in Figure 4.22.

Figure 4.23 shows repeated cycles on one same cell. Both MLLSS and absorption spectroscopy are performed. Three quantities are plotted on one same time axis: the oxygen saturation, the diffusion coefficient D and the AC/DC ratio. They are defined in section 2.5.

Results and Discussion

The most striking feature of the data in Figure 4.22 is the asymmetry

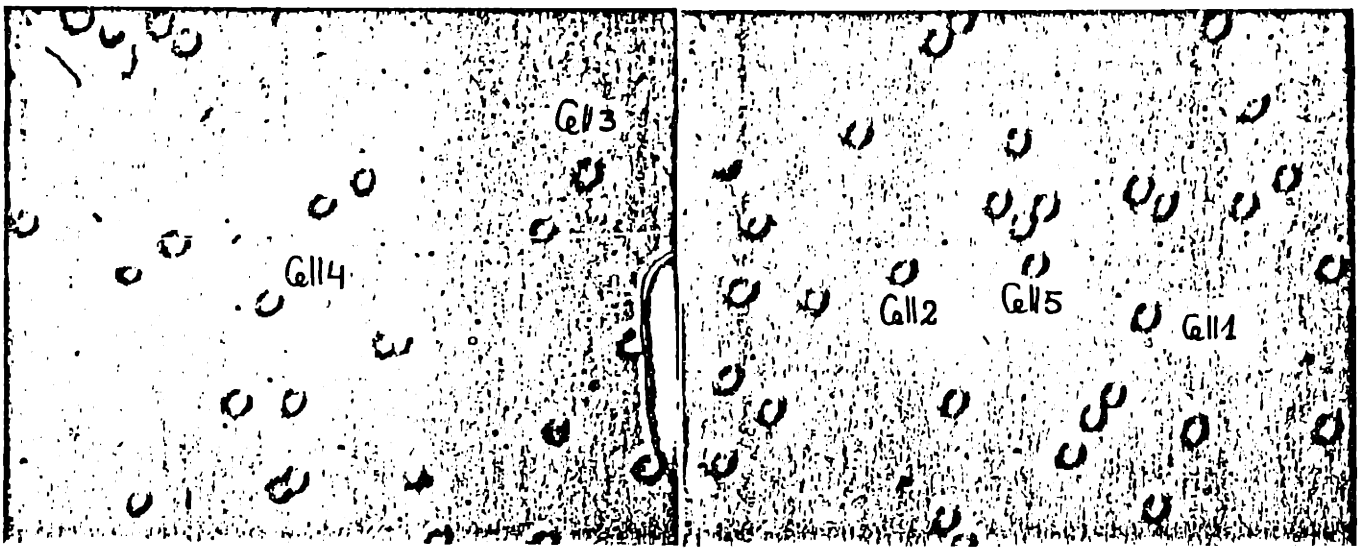

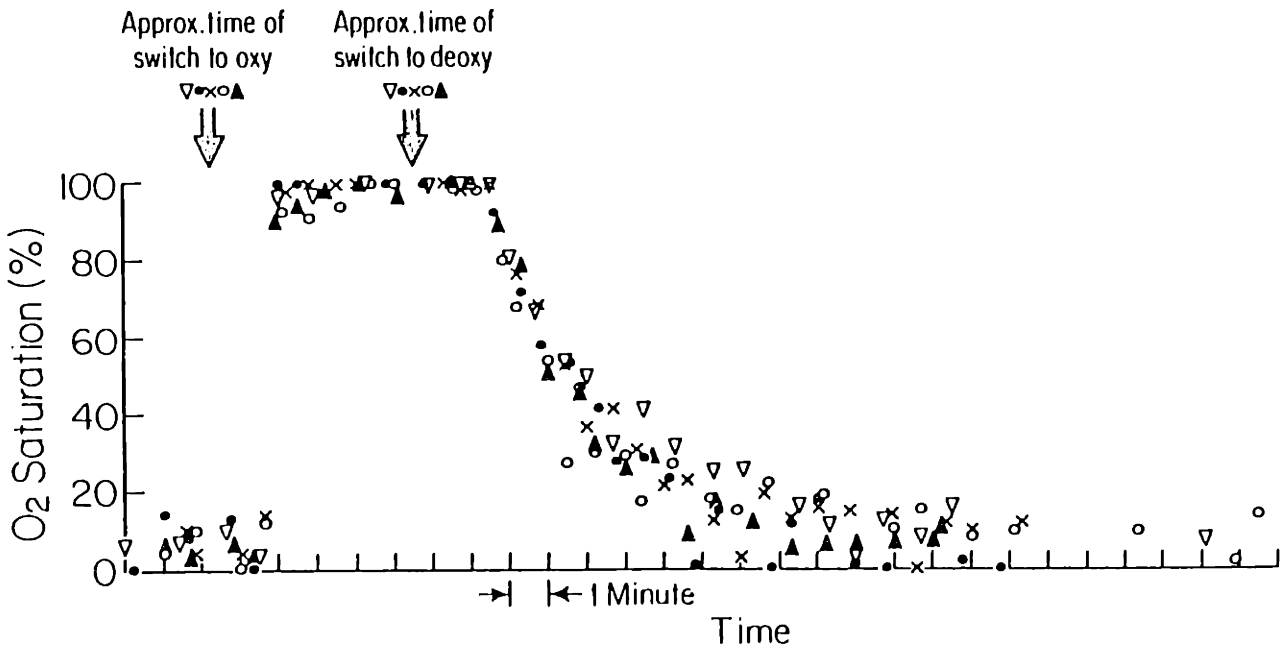

Figure 4.22 A photograph indicating the location of 5 normal red blood cells selected to demonstrate that the slow flow in the flow sample holder during measurement using MLLSS or single cell absorption spectroscopy does not induce partial oxygen pressure gradients over cell separations typical for all reported experiments in the flow cell

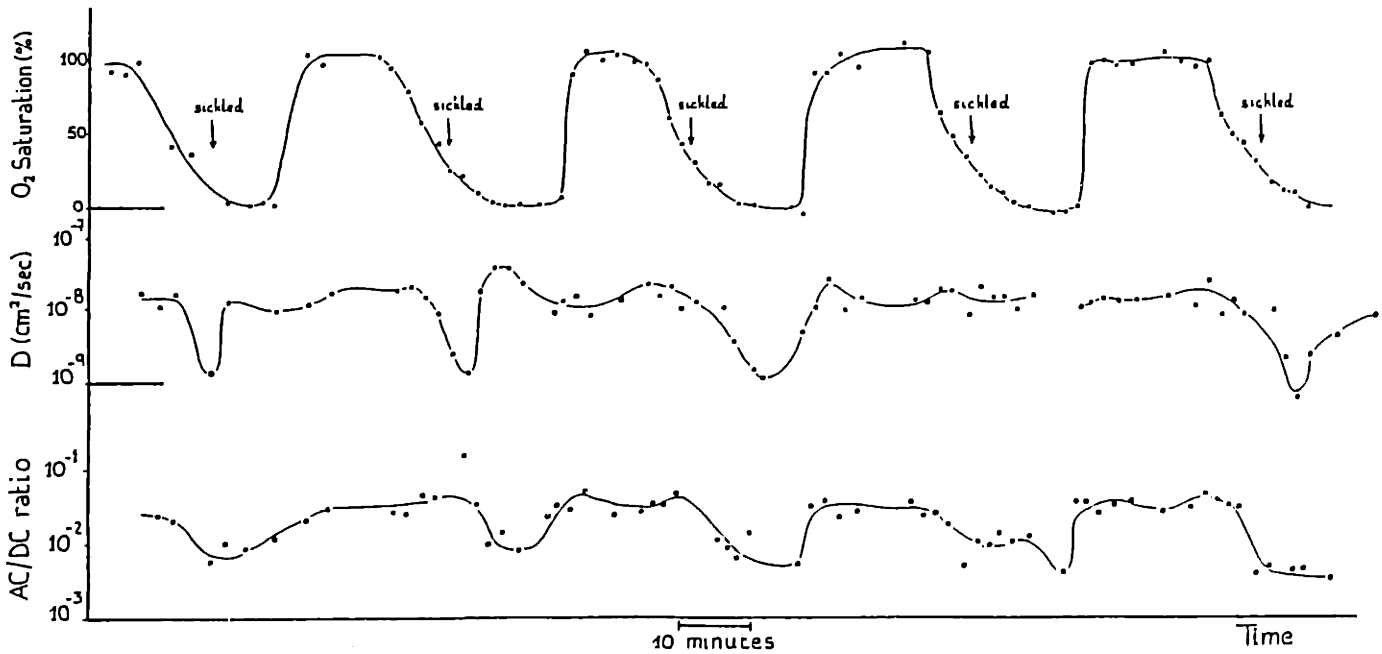

Figure 4.23 Repeated oxy-deoxy cycles on a single RBC in the Ca^{++}-free suspension buffer. On the top, the oxygen saturation of the intracellular Hb is shown as a function of time as the cell is successively exposed to the fully oxygenated and the fully deoxygenated buffer. The middle and lower panel show respectively the diffusion coefficient D and the AC/DC level for the same oxy-deoxy cycles.

between Hb oxygenation and Hb deoxygenation: the first is much more rapid than the latter. In fact, the rise in oxygen saturation level is so rapid, that it is hardly possible to record more than one data point between the deoxy and the oxy state. The five cells in the experiment do not show evidence of the existence of a gradient in the partial oxygen pressure of the buffer with location in the flow cell. Many other experiments performed in the flow cell confirmed this. One can thus safely assume that the replacement of the buffer from the one syringe by the buffer of the other syringe happens uniformly throughout the flow cell in the direction perpendicular to the flow . Only very close to the edges of the flow chamber could this be different. These areas were therefore avoided.

The repeated cycling of the two buffers is very reproducible as is demonstrated in Figure 4.23. This is extremely important since it demonstrates that the MLLSS set-up, equipped with a flow cell, is not only capable of performing experiments on single cells. It is also capable to compare the effect of the presence or absence of buffer constituents on one and a same cell. We believe that the **combination of MLLSS and a flow cell** is presently the only technique capable of performing such measurements on intact, metabolically active single cells.

4.4.h. FORMATION OF IRREVERSIBLY SICKLED CELLS BY REPEATED OXY-DEOXY CYCLING IN THE PRESENCE OF Ca^{++}? (Hb-S)

Some sickle cell anemia researchers claim [4,5,25] that irreversibly sickled cells (ISCs) are the oldest RBCs in the circulation of sickle cell

patients. The hypothesis is that the cell membrane eventually, after having reversibly sickled one to three million times, becomes leaky. The purpose of this study is to check if Hb-S aggregates are detectable in oxy sickle RBCs after repeated cycling in our flow cell.

Sample Preparation and Sample Holder

The sample holder for this experiment is the flow cell. At first, the syringes are filled with a fully oxygenated and a fully deoxygenated Ca^{++}-free buffer. The cells, which are from the major band on a density gradient, are cycled (0.056 cc/min) and monitored with MLLSS and absorption spectroscopy once to establish a Ca^{++}-free baseline for the experiment.

Subsequently, the syringes are refilled with fully oxy and fully deoxy buffer that contains Ca^{++}. This buffer is the same as the one given in section 4.2 except that the 5mM KCl is replaced with 5mM $CaCl_2$. The cells are cycled (0.056 cc/min) once while monitoring the cells with MLLSS and absorption spectroscopy. Then, they are cycled at high rate (0.15 cc/min) 30 times without monitoring them. After this rapid cycling, a slow monitoring cycle is done (0.056 cc/min) and then the entire sequence is repeated: 30 fast cycles without monitoring, 1 slow cycle with monitoring. The data are plotted in Figure 4.24. They show the oxygen saturation level, the diffusion coefficient D and the intensity ratio R as a function of time.

Results and Discussion

The diffusion coefficient D and the AC/DC ratio do not show any evidence of irreversibly aggregated Hb-S after the 60 oxy-deoxy cycles in a Ca^{++} medium. Of course, 60 cycles is very much less than the typical 1

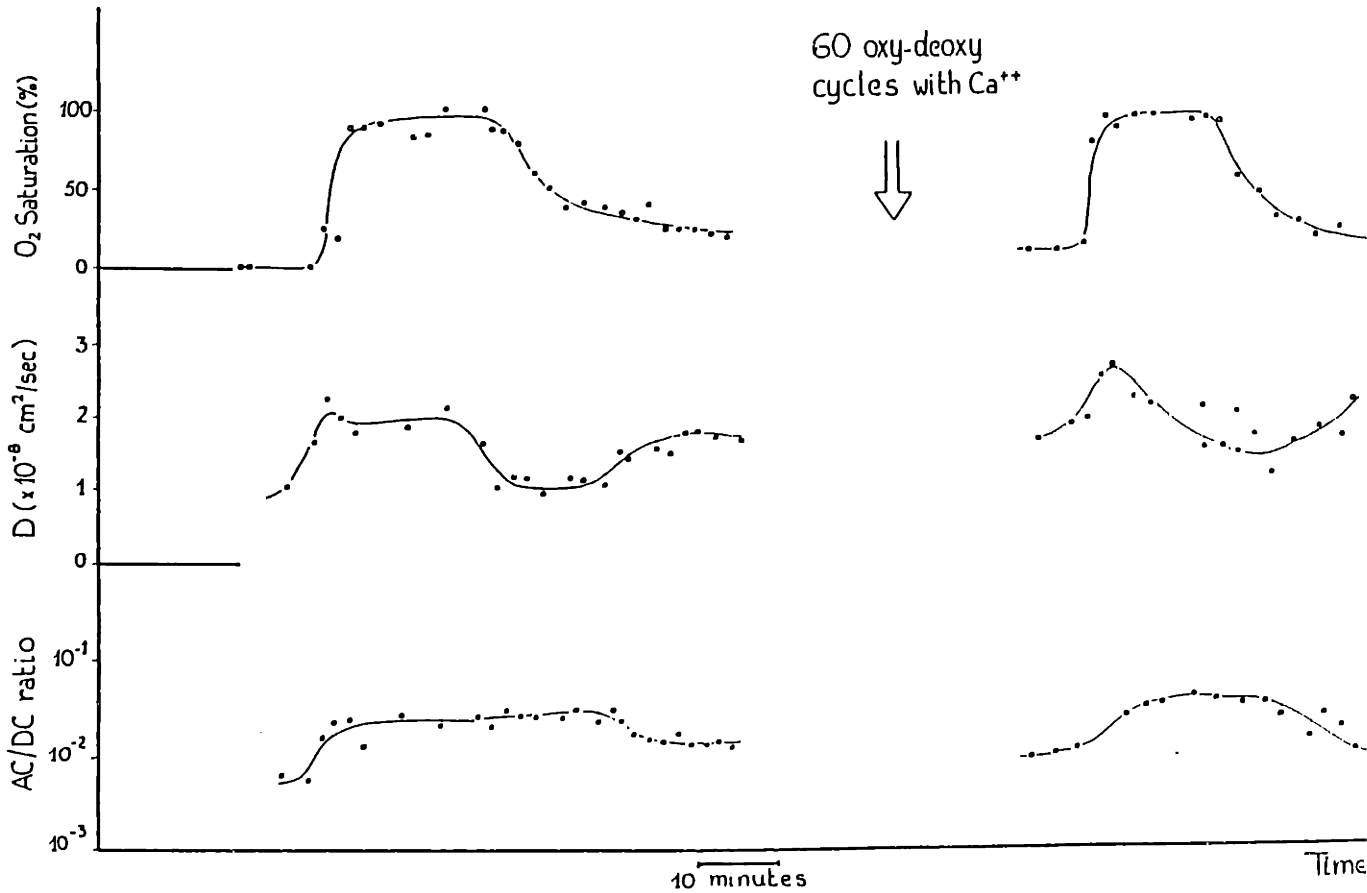

Figure 4.24 One oxy-deoxy cycle exposing a RBC to fully oxygenated and fully deoxygenated Ca^{++}-free suspension buffer (oxygen saturation, diffusion coefficient and AC/DC level) and one oxy-deoxy cycle on the same RBC after 60 cycles in a Ca^{++} containing buffer.

million cycles that a sickle RBC goes through in the circulation. Yet, in the body, the pO_2 does not drop below typically 40 mmHg, which is the pO_2 in the veins. Some [4] have claimed that the induced irreversible sickling occurs much more readily under these conditions. With this assumption, the experiment should maybe be repeated under more strenuous conditions. At this stage, however, we can say that we could not confirm the induced irreversible Hb-S aggregation under the conditions predicted by some sickle cell anemia researchers.

4.4.i. MEMBRANE FLEXIBILITY IN NORMAL AND SICKLE RBCs (Hb-A and Hb-S)

It has been known for a long time that sickle RBCs are less flexible on average than normal RBCs, even in the fully oxygenated state. The question, however, remains [23,24,26,27] if this is due to membrane flexibility, cytoplasmic viscosity or binding of Hb-S to the inner wall of the RBC membrane. No studies, to my knowledge, have found the answer to this question in a non controversial way. A very similar question remains unanswered for the RBCs of people with diabetes. Both in sickle cell anemia and in diabetes, it is a very important question from the pharmacological standpoint.

Sample Preparation and Sample Holder

The sample holder is the microcapillary cell. Both normal and sickle RBCs were used. Before claiming that a fraction of the intensity fluctuations originate from membrane motion when MLLSS is performed on whole cells, it is necessary to determine the frequency range of intensity

fluctuations caused by cell membranes alone. In order to do so, I prepared RBC ghosts. These are relatively intact cell membranes filled with the suspension buffer rather than with the concentrated Hb solution.

To make ghosts that contain as little Hb as possible, it is essential to lyse (break) the RBCs abruptly. This is done as follows. First wash about 1 ml of whole blood in the usual way. Add 1 ml of the washing buffer to the final pellet of RBCs in order for the individual cells to be well separated from one another. Then, rapidly dilute 1 volume of this cell suspension in 40 volumes of a 15mM phosphate buffer at pH 7.4 (19% of monobasic and 81% of dibasic) by adding the RBCs to the buffer while stirring it. Centrifuge the mixture at 9000 rpm for 20 minutes. The pellet looks white with a red central spot (unlysed cells). The supernatant is bright red; it contains the Hb. Aspirate the supernatant carefully, discard it, slowly move the tube and then gently aspirate the white part of the pellet. Add 20 volumes of phosphate buffer to it and centrifuge the new suspension at 9000 rpm for 20 minutes. Repeat this last procedure till the pellet looks white (or hardly pink, which is harder for dens sickle cells or less fresh cells than for other cells). It should now contain RBC ghosts only. Resuspend them to an appropriate concentration using the 15mM phosphate buffer.

For whole cell experiments, the RBCs were washed as usual. Normal and sickle cells were used. Also osmotically swollen cells were studied. These were prepared as described in section 4.4.a in 150 milli-osmoles.

Data and Data Analysis

A few correlation functions taken from normal RBC ghosts using the illumination from the top and from the bottom are shown in Figure 4.25.

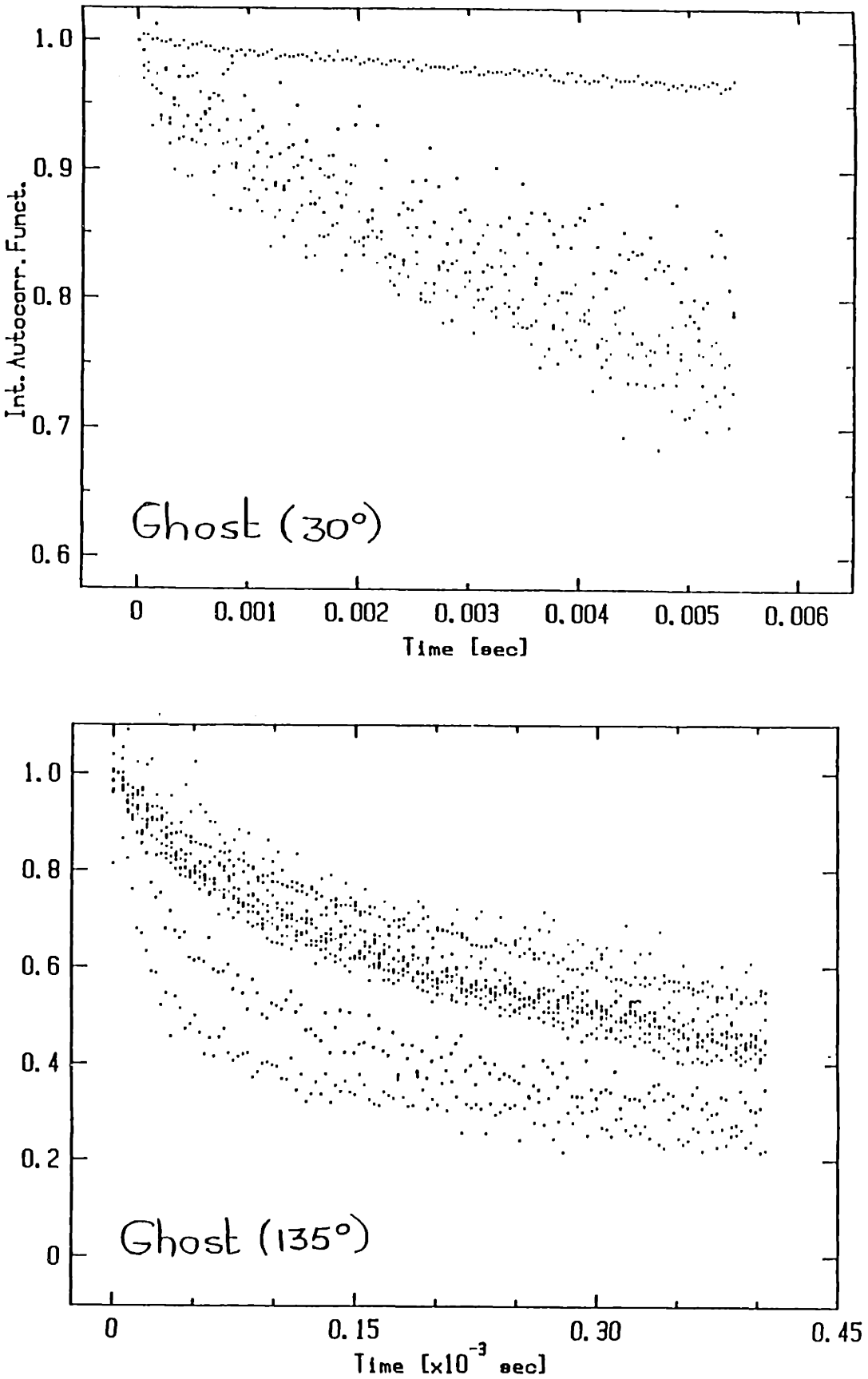

Figure 4.25 Intensity autocorrelation functions measured on RBC ghosts using small angle scattering (top) and large angle scattering (bottom). Some of the latter correlation functions show clear double exponential features

The signal is very weak in the bottom illumination (small angle) and rather strong in the top illumination (large angle). Interestingly, the correlation functions collected at large angles have a double exponential feature which is not found in small angle scattering. The table in Figure 4.26 shows the diffusion coefficient D_{se} from a single exponential fit of the small angle data, the fast and the slow diffusion coefficients D_f and D_s from a double exponential fit on the large angle data, the corresponding characteristic decay time f_s for the slow component, the relative amplitude $A_f/(A_f+A_s)$ of the fast signal, and the signal to background ratio s/b_f and s/b_s for small and large angle scattering.

Top and bottom illumination MLLSS was performed on normal RBCs, on sickle RBCs and on osmotically swollen RBCs. The values for D_{se}, D_f, D_s, f_s, s/b_f, s/b_s and $A_f/(A_f+A_s)$ are given in the table of Figure 4.26.

Results and Discussion

At first I wish to suggest an explanation for the ghost signal found in these experiments. Figure 4.27 shows the scattering vectors and a RBC as well as the scattering volume. In small angle scattering, the present set-up is mostly sensitive to horizontal motion (on a long length scale). At the large angle, scattering is mostly sensitive to vertical motion (on a shorter length scale). This difference between the two configurations combined with the particular shape of the RBCs may explain our findings. If the RBC has "breathing" modes like the one schematically illustrated in Figure 4.27, then the membrane moves back and forth in the horizontal direction on the edges of the disc shape. Those edges are, however, separated by about 8μm which is much larger than the linear dimension of

Sample	D_{se} (cm^2/sec) ~ 27°	D_f (cm^2/sec) ~ 148°	D_s (cm^2/sec) ~ 148°	f_s (Hz) ~ 148°	s/b ~ 27°	s/b ~ 148°
normal RBC	4.0×10^{-8} $\pm1.1\times10^{-8}$	2.4×10^{-7} $\pm1.1\times10^{-7}$	6.1×10^{-9} $\pm1.2\times10^{-9}$	412 ±81	3.0×10^{-2} $\pm1.7\times10^{-2}$	2.1×10^{-2} $\pm1.3\times10^{-2}$
,,	2.8×10^{-8} $\pm0.6\times10^{-8}$	1.4×10^{-7} $\pm0.7\times10^{-7}$	4.8×10^{-9} $\pm1.3\times10^{-9}$	324 ±88	2.0×10^{-2} $\pm1.1\times10^{-2}$	3.6×10^{-2} $\pm3.7\times10^{-2}$
,,	3.2×10^{-8} $\pm0.5\times10^{-8}$	2.0×10^{-7} $\pm0.4\times10^{-7}$	6.7×10^{-9} $\pm0.9\times10^{-9}$	453 ±61	2.2×10^{-2}	2.0×10^{-2} $\pm1.5\times10^{-2}$
swollen RBC	2.8×10^{-8} $\pm1.3\times10^{-8}$	3.1×10^{-7} $\pm1.4\times10^{-7}$	6.6×10^{-9} $\pm1.8\times10^{-9}$	446 ±122	1.9×10^{-2} $\pm0.8\times10^{-2}$	5.6×10^{-2} $\pm3.9\times10^{-2}$
sickle RBC	2.5×10^{-8}	2.8×10^{-7} $\pm1.0\times10^{-7}$	6.6×10^{-9} $\pm1.3\times10^{-9}$	446 ±88	2.6×10^{-2} $\pm1.6\times10^{-2}$	2.3×10^{-2}
normal GHOST	1.9×10^{-8} $\pm0.9\times10^{-8}$	2.7×10^{-7} $\pm1.1\times10^{-7}$	10.0×10^{-9} $\pm1.4\times10^{-9}$	676 ±95	1.4×10^{-2} $\pm1.4\times10^{-2}$	4.4×10^{-2} $\pm4.4\times10^{-2}$

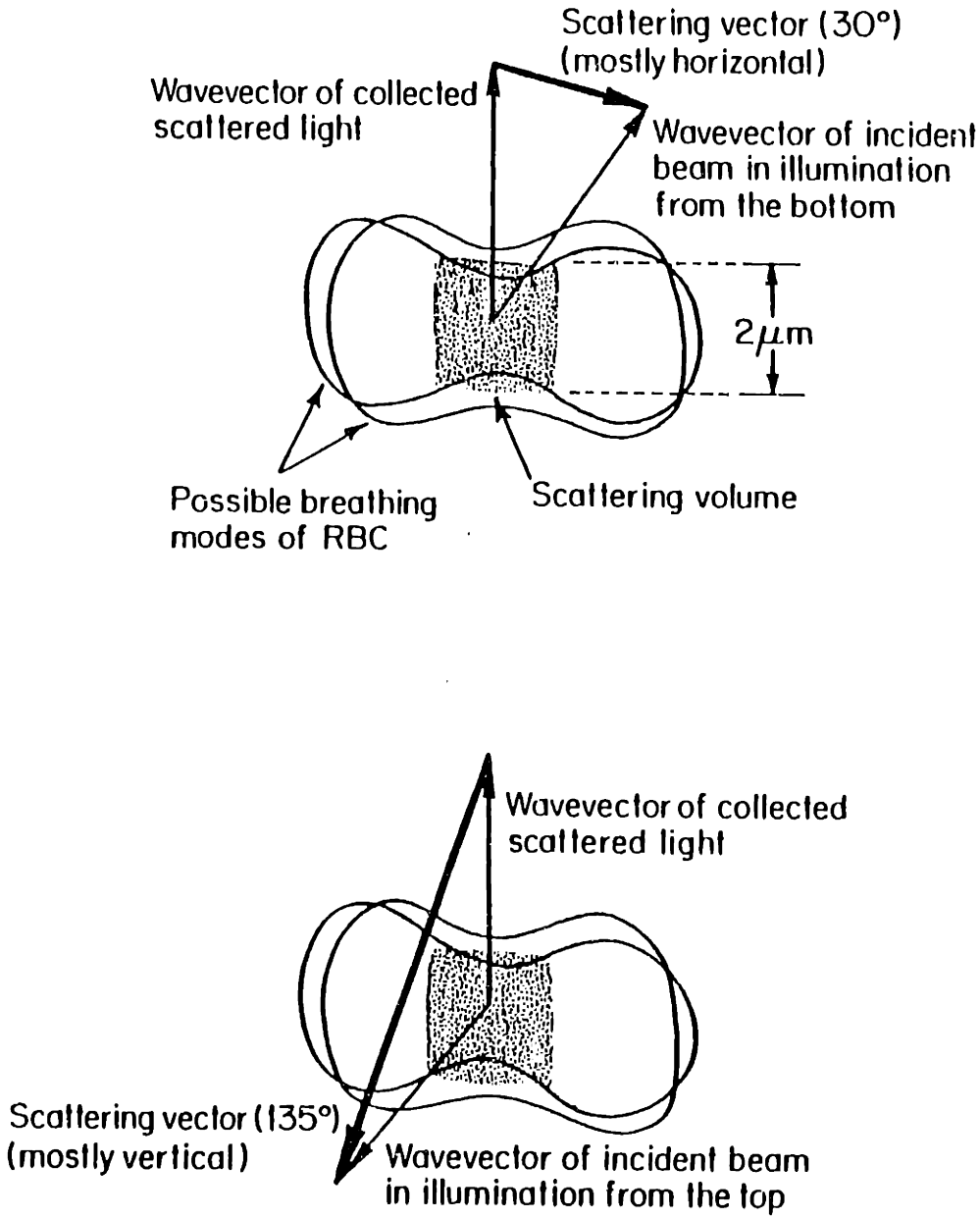

Figure 4.27 The scattering vectors and their orientation relative to the RBC in the present set-up. The linear dimension of the scattering volume is comparable to the RBC thickness

the scattering volume (2 μm). It is thus not hard to avoid scattering from these edges. Thus, membrane motion hardly contributes at all to forward angle scattering. In the vertical direction (the thickness direction of the cell), the breathing motion moves the top area of the RBC up and down (the bottom is fixed on the glass of the sample holder). In this direction, the linear dimension of the RBC is only 2 μm and it is thus impossible to avoid contributions of membrane motion in the large angle configuration. This may explain the lack of a double exponential feature in small angle scattering from ghosts.

My assumption is that the two frequencies found in large angle scattering, can be attributed to Hb and membrane motion. It is indeed known that one can never totally remove the Hb from ghosts. To confirm this, I collected absorption spectra from ghosts. This is rather difficult, because the ghosts are extremely transparent. In fact, to get significant spectra, I had to prepare the ghosts as described above, wash them well, and then reconcentrate them using a centrifuge. Figure 4.28 shows two spectra. One is taken by averaging 100 spectra accumulated during 1 sec each on a whole RBC. The other is taken in the same way on a concentrated suspension of ghosts. I estimate that the absorption spectrum was taken through 20 to 30 ghosts. Though the signal is still weak, it is clear that some Hb is present inside the ghosts. Thus, the fast component in the correlation functions at large angle could originate from this very diluted Hb. A literature search seems to confirm that there exists no membrane motion at these high frequencies (about 1.5×10^4 1/sec in our data). Some people did consider this possibility [28,29] but seem to conclude that it does not exist in RBCs. Several authors [28-37] predict or report membrane motion with frequencies between 15 Hz [29] (at very a very large

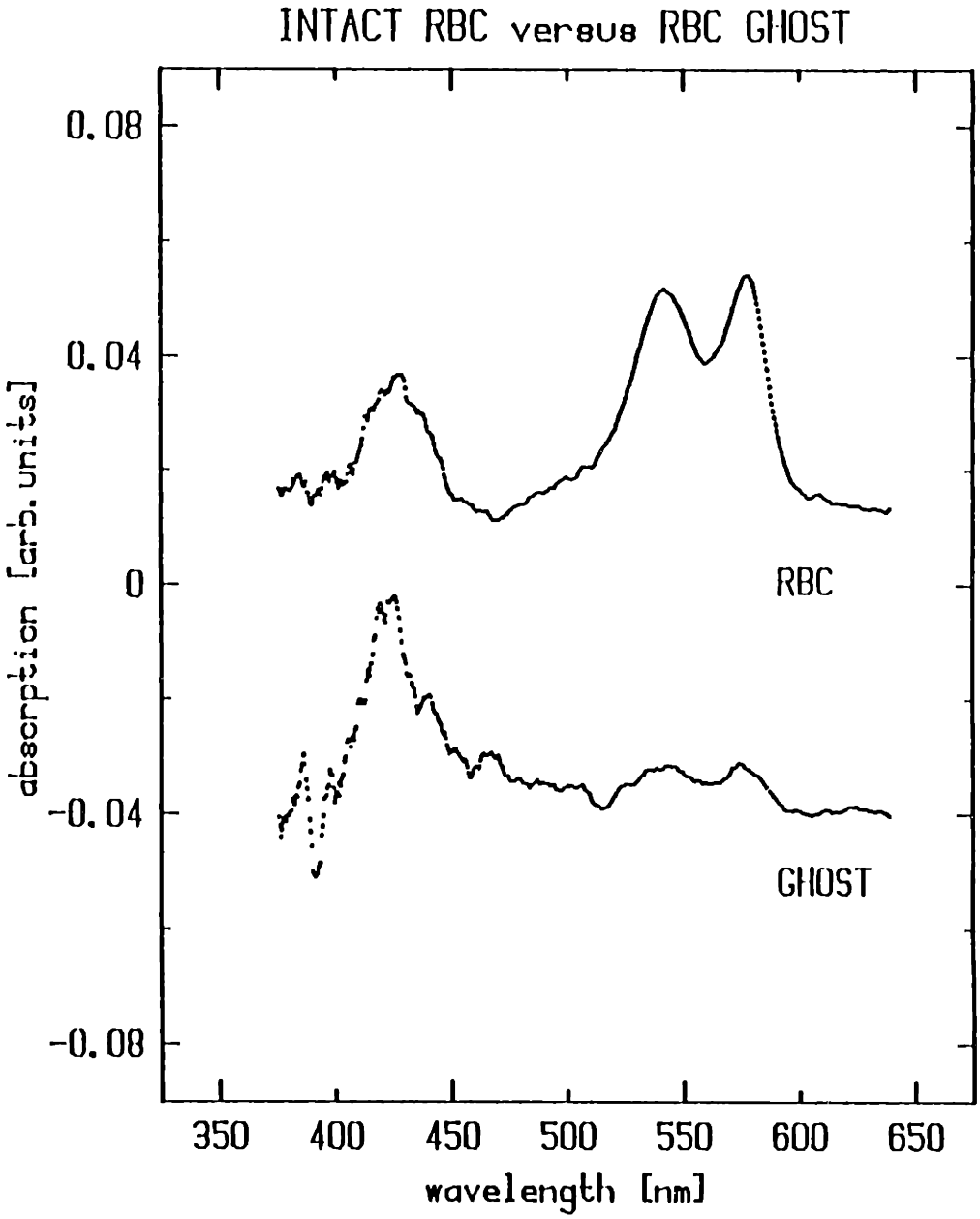

Figure 4.28 Absorption spectra taken on a single RBC and on a concentrated suspension of washed RBC ghosts. The spectra are the average of 100 spectra accumulated during 1 sec each.

scattering vector), 40 Hz [34] and a few 100 Hz (170 Hz in [35] which is a dynamic light scattering study on a suspension of RBC ghosts at an angle of 144°). In fact, as early as 1890, Browicz [38] described vibratory movements in human erythrocytes. This motion was first called "the flicker phenomena" by Blowers et al. in 1951 [32] and it since often goes by that name. Many papers comment on its presence or absence, only few study it in a quantitative manner and, so far, no consensus has been reached about its origin.

I found a slow component with an inverse **characteristic decay time** of about 400 Hz in the whole RBCs and 670 Hz in the RBC ghosts. The difference between the frequency in ghosts and in whole RBCs is probably due to the differences in viscosity between the cell interiors in both cases. The viscosity of the Hb containing cytoplasm of the whole cells is about 6 times higher than that of the buffer that fills the ghosts. The slow motion, which I identify with membrane motion, in the ghosts is about 1.6 times faster than in RBCs. It may be due to stronger slowing down hydrodynamic drag on whole RBC membranes than on ghost membranes because the cytoplasm is more viscous than the ghost filling buffer.

Because the small angle scattering is relatively insensitive to membrane motion, the **signal to background** or **AC/DC** ratio at these angles is rather smaller in ghosts than in whole RBCs due to the difference in Hb concentration. At the larger scattering angles, however, this is not so, because both Hb and membrane contribute to the scattered intensity fluctuations.

The **diffusion coefficients** given in Figure 4.26 were all computed from the characteristic decay times of the intensity autocorrelation functions

using the viscosity of water. This is a good approximation of the true viscosity for all motion in ghosts. However, in whole RBCs, it is certainly an underestimate for the Hb inside the cell. For the slower membrane motion, the viscosity is close to that of water on the outside of the cell and higher on the inside. This tends to slow the membrane motion down as was already discussed earlier. I was expecting to find appreciably faster diffusion coefficients for the Hb in ghosts than for the Hb in whole RBCs for two reasons. First, the concentration is much lower inside the ghosts and second, the cytoplasm is more viscous than the suspension buffer. It was a surprise to find the D_f values to be comparable and do not have a quantitative explanation for this, but I believe the answer can be found in the hydrodynamic interaction that exists between the opposite surfaces of the RBCs. I think that this interaction could be stronger in the ghosts than in the whole RBCs and could cause some effective slowing down of the Hb especially in ghosts. This will be the topic of further research in the near future.

REFERENCES

[1] L. Pauling et al.; Sickle cell anemia, a molecular disease; Science 110 , 543-548, 1949

[2] V. Ingram; A specific chemical difference between the globins of normal human and sickle cell anaemia haemoglobin; Nature 178 , 792-794, 1956

[3] B. Wishner et al.; Crystal structure of sickle-cell deoxyhemoglobin at 5 A resolution; J.Mol.Biol. 98 , 179-194, 1975

[4] S.T. Ohnishi; Inhibition of in vitro formation of irreversibly sickled cells by cepharanthine; Br.J.Haematol. 55 , 665-671, 1983

[5] C.M. Smith; The irreversibly sickled cell; Am.J.Ped.Hemat.&Onc. 4 , 307-315, 1982

[6] T. Maugh; A new understanding of sickle cell emerges; Science 211 , 265-267, 1981

[7] L. Luzzato et al.; Fetal hemoglobin and malaria; Lancet 2 , 523-524, 1976

[8] M.J. Friedman; Erythrocyte mechanism of cycle cell resistance to malaria; Proc.Natl.Acad.Sci.USA 75 , 1994-1997, 1978

[9] M.J. Friedman; Ultrastructural damage to the malaria parasite in the sickled cell; J.Protozool. 26 , 195-199, 1979

[10] S.T. Ohnishi et al.; Measurement of red cell sickling: a method for studying the efficacy of antisickling drugs under physiological condi-

tions; Can.J.Physiol. Pharmacol. 61 , 941-945, 1983

[11] E. Antonini and M. Brunori; Hemoglobin and myoglobin and their reactions with ligands; North Holland Publ. Co., 1971

[12] D. Mazia et al.; Adhesion of cells to surfaces coated with polylysine; J.Cell Biol. 66 , 198-200, 1975

[13] B. S. Jacobson et al.; Plasma membrane: rapid isolation and exposure of the cytoplasmic surface by use of positively charged beads; Science 195 , 302-304, 1976

[14] P. Ross et al.; Analysis of non-ideal behavior in concentrated hemoglobin solutions; J.Mol.Biol. 112 , 437-452, 1977

[15] R. Siezen et al.; Exclusion chromatography of concentrated hemoglobin solutions, Comparison of the self-association behavior of the oxy and deoxy forms of the $\alpha_2\beta_2$ species; Biophys.Chem. 14 , 221-231, 1981

[16] oligomers of nucleation in HbS

[17] M. Bessis, Living Blood Cells and their Ultrastructure p.169, Springer-Verlag (1973)

[18] C. Noguchi et al.; Intracellular polymerization of sickle hemoglobin; J. Clin. Invest. 72 , 846-852, 1983

[19] M. Fabry et al.; The effect of deoxygenation on red blood cell density: Significance for the pathophysiology of sickle cell anemia; Blood 60, 1370-1377, 1982

[20] I. Nishio et al.; Microscope laser light scattering spectroscopy of

single biological cells; Cell Biophysics 7, 91-105, 1985

[21] R. Benesch, R. Edalgi, S. Kwong and R. Benesch, ... , Anal. Biochem. 89, 162-173 (1978)

[22] J. Pumphrey et al.; Oxygen equilibrium of emulsified solutions of normal and sickle hemoglobin; Biophys. Biochem. Res. Comm. 88, 980, 1979

[23] S. Chien; Rheology of sickle cells and erythrocyte content; Blood Cells 3 , 283 (1977)

[24] S.T. Ohnishi; Viscosity and filtrability measurements of sickle cell suspensions in the development of anti sickling drugs; Blood Cells 8, 79-... (1982)

[25] J. Palek; Red cell membrane injury in sickle cell anaemia; Br.J.Haematol. 35 , 1-9 (1977)

[26] S. Fischer et al.; The binding of hemoglobin to membranes of normal and sickle erythrocytes; Biochem.Biophys.Acta 375, 422-433 (1975)

[27] Vincentzi ....

[28] M. Peterson; Shape dynamics of nearly spherical membrane bounded fluid cells; Mol.Cryst.Liq.Cryst. 127, 257-272 (1985)

[29] F. Brochard et al.; Frequency spectrum of the flicker phenomenon in erythrocytes; J.de Physique 36, 1035-1047 (1975)

[30] R. Cabot; A guide to the clinical examination of blood 4^{th} edition, Longmans, Green and Co., London, 1901

[31] R. Pulvertaft; Vibratory movement in the cytoplasm of erythrocytes; J.Clin.Pathol. 2, 281-..., 191949

[32] R. Blowers et al.; Flicker phenomenon in human erythrocytes; J.Physiol. 113, 228-239, 1951

[33] A. Parpart et al.; Flicker in erythrocytes "Vibratory movements in the cytoplasm"?; J.Cell.Comp.Physiol. 47, 295-303, 1956

[34] A. Burton et al.; Quantitative studies on the flicker phenomenon in the erythrocytes; Blood 32, 819-822, 1968

[35] C. Bargeron et al.; Light-beating spectrum of erythrocyte ghosts; Phys.Rev.Lett. 28, 1105-1107, 1972

[36] W. Helfrich; Blocked lipid exchange in bilayers and its posible influence on the shape of vesicles; Z.Naturforsch 29c, 510-515, 1974

[37] M. Schneider et al.; Thermal fluctuations of large quasi-spherical bimolecular phospholipid vesicles; J.de Physique 45, 1457-1472, 1984

[38] E. Browicz; Zbl.Med.Wiss. 28, 625, 1890

Chapter 5 :

CHICKEN EMBRYO LENSES: CELL DIFFERENTIATION AND PROTEIN SYNTHESIS

5.1 δ-CRYSTALLIN ACCUMULATION IN THE DEVELOPING CHICK EMBRYO LENS

Rapid progress is being made in the understanding of molecular events of cellular differentiation, particularly at the level of gene expression. Lens cell differentiation has been a favorable system of investigation because it is associated with a marked change in morphology (cell elongation) and differential synthesis of the soluble lens proteins (crystallins). Also, the chick lenses are easily accessed at all stages of the lens development. The crystallins are the structural proteins of the lens and they comprise 90% of the soluble protein of the lens. δ-crystallin is one of the crystallins and is found in birds and reptiles [1]. A review on lens differentiation and lens crystallins can be found in [2].

A mature chicken lens contains two kinds of cells: simple, small epithelial cells and more evolved, elongated fiber cells. The fiber cell differentiate out of the epithelial cells as they divide. Figure 5.1 illustrates the lens development. Coincident with this cell differentiation is the synthesis of δ-crystallin proteins, which are found only in the fiber cells. The crystallin protein accumulates in the fiber cells till it comprises about 70% to 80% of the soluble protein. The δ-crystallin pro-

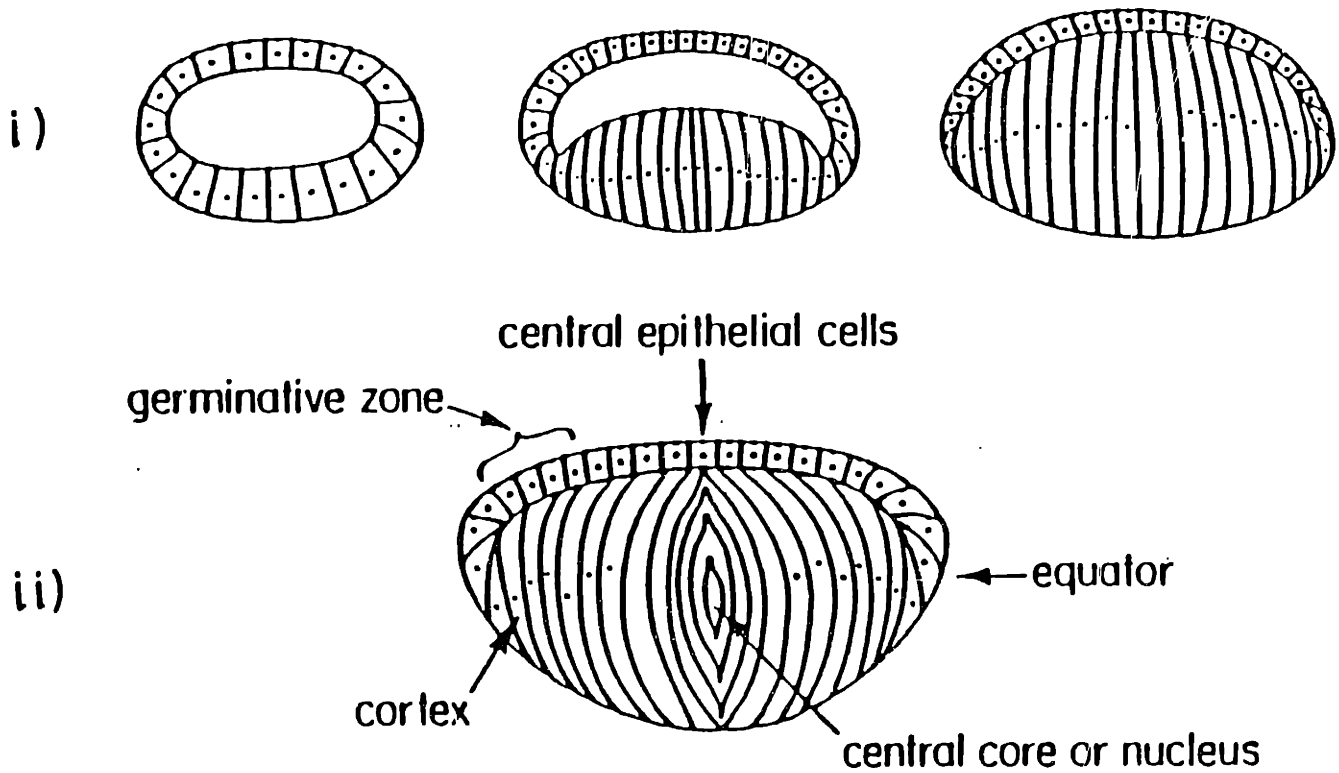

Figure 5.1 (i)Sketch of chick eye lens development showing the initial vesicle of epithelial cells, the intermediate stage with elongated posterior cells differentiated into fiber cells and the final stage in which the hollow of the lens is completely filled with fiber cells (ii)Sketch of the mature lens indicating different regions of the lens

duction gradually decreases with the age of the chicken till it finally almost stops. Consequently, the δ-crystallin concentration is high in the center of the adult lens (nucleus), which contains the cells deposited early in development. It is very low at the lens periphery (cortex), which contains the cells deposited later in development [3].

Though a vast amount of experiments were performed on the chick embryo lens, most were extremely disruptive. All biochemical methods lose spatial resolution and in situ methods such as immunofluorescence, were up to now qualitative at best. Both may introduce artifacts. It thus seems that MLLSS is an ideal technique to address some of the remaining questions in this context. The eye lens is perfectly suited for MLLSS. It is an optically clear system and the cells do not contain a very large amount of light scattering components. Indeed, the epithelial cells contain mainly large organelles and a nucleus. Immediately after the differentiation of such a cell into a fiber cell is initiated, these large scatterers start disappearing. Simultaneously, δ-crystallin is synthesized and its concentration increases while the concentration of organelles decreases [4]. Eventually, δ-crystallin seems to be just about the only scatterer inside the fiber cell. It is possible to peel the layer of epithelial cells off the lens and to keep these cells alive in a petri dish with an appropriate buffer. The techniques have been developed to initiate epithelial cell to fiber cell differentiation in the explanted petri dish sample. The aim is to study the effect of different conditions and agents on this differentiation and also on the trans-differentiation of primitive cells, originally predestined to evolve into non-fiber cells, into fiber cells. We also hope, in the future, to check the assumption that the germinative region where differentiation occurs, is indeed located on a ring in the epithelial

layer where it is currently assumed to be located. This chapter shows the results of preparative work done using the conventional QLS and of preliminary work done using MLLSS on this system.

5.2 CONVENTIONAL QLS ON DEVELOPING CHICK LENSES

The results presented here were published in 1984 (S.-T.Sun, T.Tanaka, I.Nishio, J.Peetermans, J.Maizel and J.Piatigorsky; Direct observation of δ-crystallin accumulation by laser light-scattering spectroscopy in the chicken embryo lens; Proc.Natl.Acad.Sci.USA 81 , 785-787, 1984). In conventional QLS one scatters light of several cells at a time. Thus all the results shown here are an average over typically 50 cells. Because the fiber cells are stacked onto the bulk of the lens from the equatorial periphery of the lens, their should be a one to one correspondence between the age of the cells in the lens and the position of the cells. This was confirmed in the following way. First we scanned an already large lens that is almost fully matured, from the center (oldest cells) to the periphery (youngest cells). Then QLS was performed on the center of lenses from chick embryos younger than the one for the first experiment. Two sets of intensity correlation functions are shown in Figure 5.2. The age of the embryo is counted in days after the onset of development which coincides with the time at which the eggs are placed in a 37° humidified incubator. Indeed, chick embryo development does not start at the fertilization of the egg, but rather at the time the egg is placed in a warm, incubating environment (the brooding hen). It is clear that the functions of Figure 5.2 are not single exponentials. They were analyzed using a double

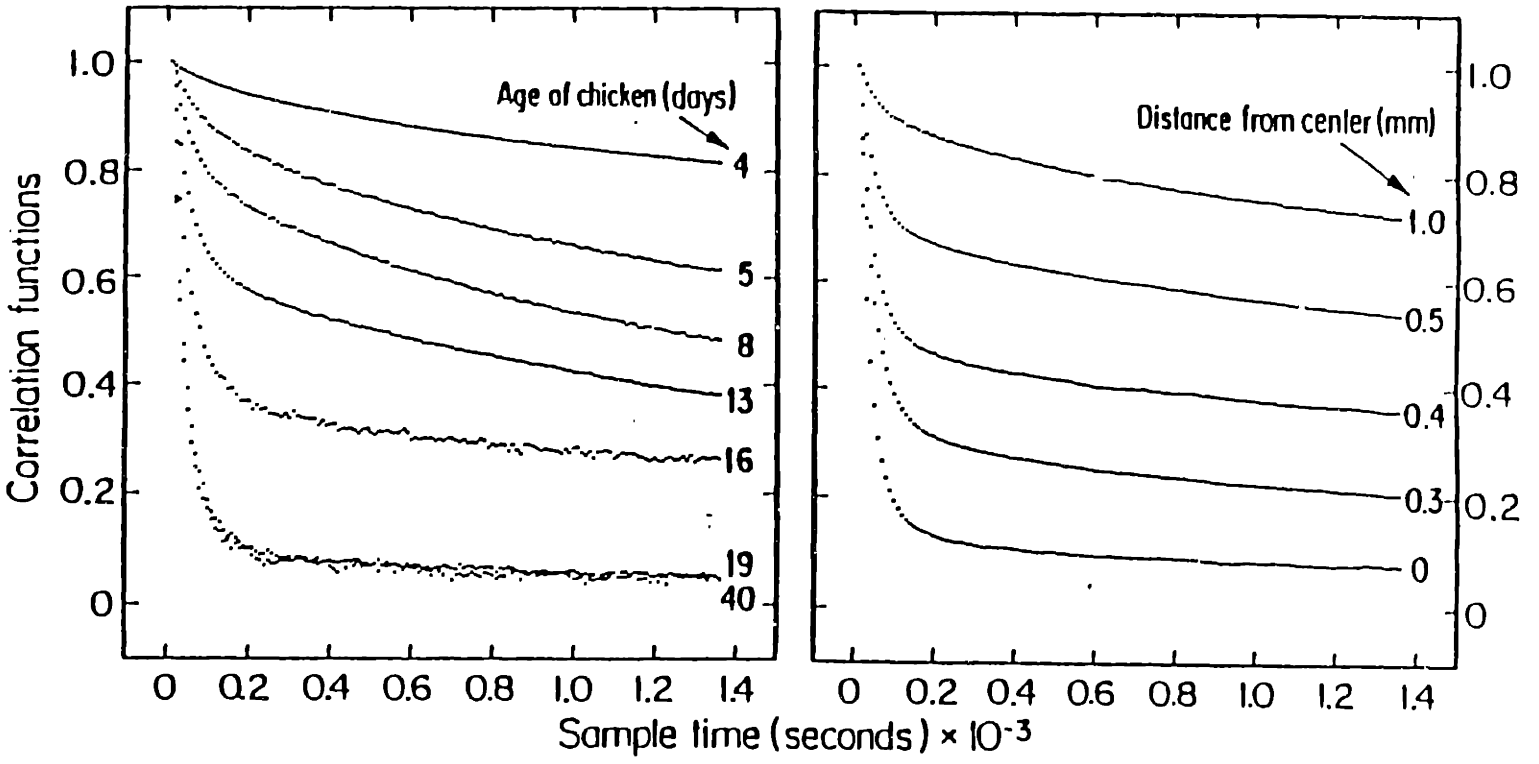

Figure 5.2 Intensity Autocorrelation Functions taken on the Center of Lenses of Different Ages (left) and at Different Locations in a Scan from to Center of a Mature Lens to the Periphery of the same lens (right)

exponential fit (see Eq.2.28).

$$c(\tau) = (A_f e^{-D_f k^2 \tau} + A_s e^{-D_s k^2 \tau})^2 \qquad 5.1$$

where D_f and A_f correspond to the small (fast) particles and D_s and A_s to the large (slow) scatterers. This was done in the following way. Many correlation functions were taken on the center of lenses of the youngest embryos (4 days) and on the center of mature lenses. These functions are more closely single exponential. A single exponential fit on them yields diffusion coefficients that correspond to sizes of about 65A and 6700A (probably the organelles) using Eq.2.13.

$$D = \frac{k_B T}{6\pi \eta a} \qquad 5.2$$

We assumed that the 65A particles are the δ-crystallin proteins. This is not in contradiction with electron microscopy done on purified δ-crystallin samples (see electron micrograph in the paper stated above by S.-T.Sun et al.). The latter experiments gave sizes of about 42A and QLS on a dilute solution of the same crystallins gave 45A. The increased observed size inside the intact lenses is probably due to the interactions between the crystallin proteins at the high intracellular concentrations. There may be some protein aggregation too.

Once the two diffusion coefficients are determined as explained, the correlation functions for all locations and all ages are fitted using Eq.5.1 with fixed D_1 and D_2. The fits yield the values A_f and A_s. In Figures 5.3 and 5.4 we plot the relative amount of δ-crystallin defined as

$$R_\delta = \frac{A_f}{A_f + A_s} \qquad 5.3$$

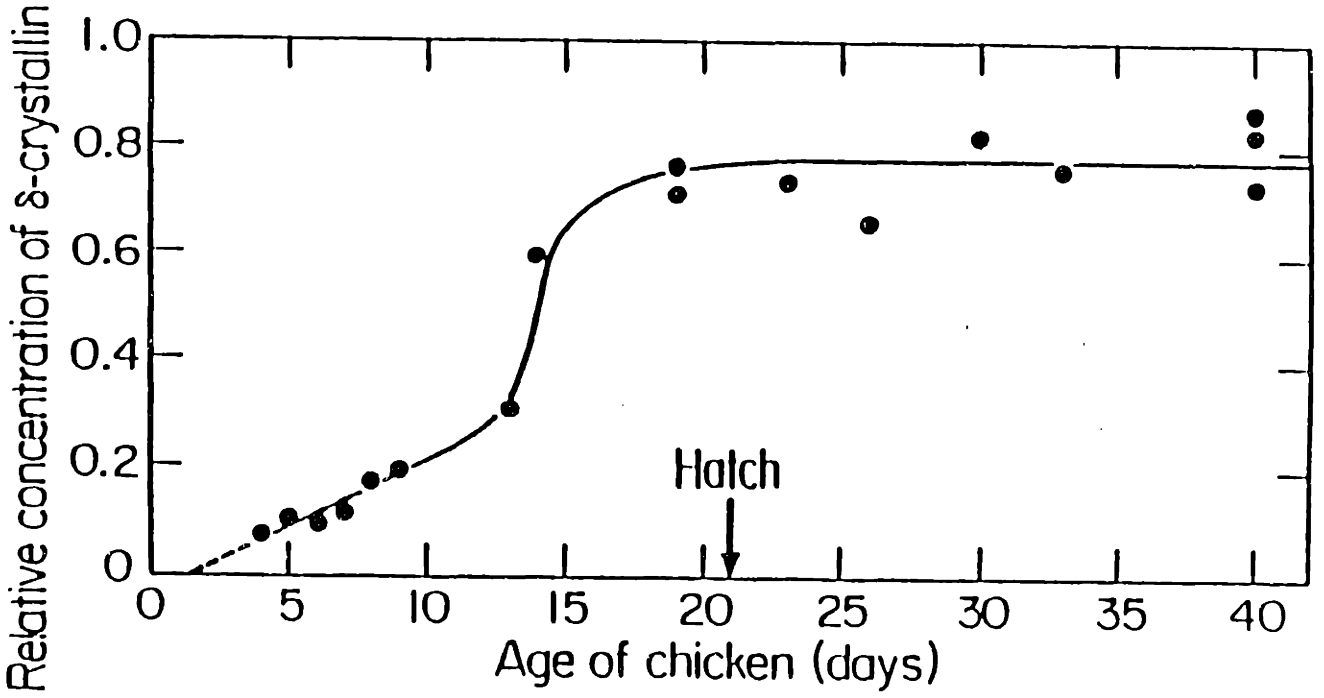

Figure 5.3 Relative Concentration of δ-crystallin in the Center of the Lens as a function of the Age of the Chick and thus of the Lens. By the time the chick hatches, the relative δ-crystallin concentration has reached a plateau at about 78%

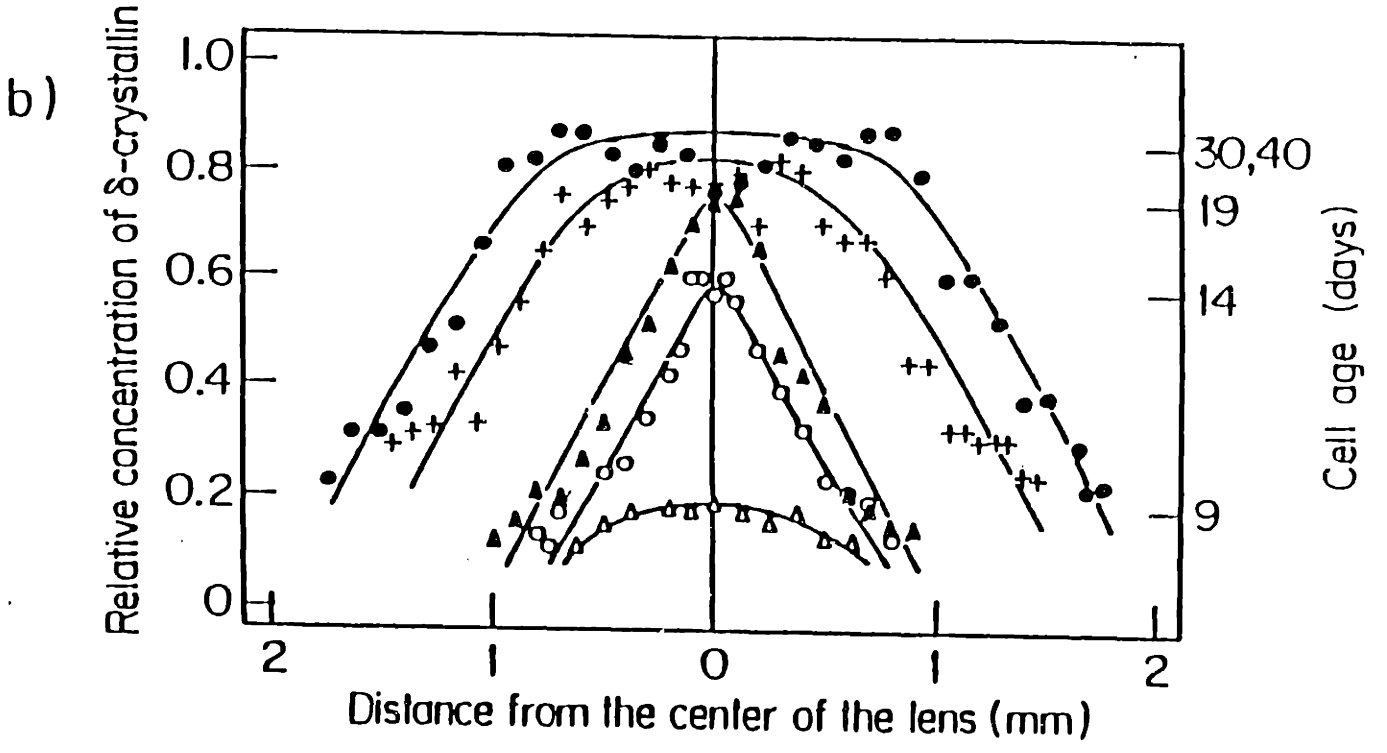

Figure 5.4 Relative Concentration of δ-crystallin as a function of Position in the Lens for Lenses of Different Ages. The parallel vertical axis indicates the Cell Age taken from the one to one correspondence between cell age and relative δ-crystallin concentration given in Figure 5.3

as a function of chick age and position in the lens. The first curve corresponds to data taken in the center of lenses so that the chick age is about the same as the cell age. In Figure 5.4 lenses of chicks of different age are scanned. The curves are nicely symmetric about the lens center. The right vertical axis is the estimated age of the cells that give the R_δ value at the corresponding position on the left vertical axis. The right vertical axis is extracted from Figure 5.3. The dashed line in Figure 5.3 is extrapolated using a linear fit on the first six data points. It suggests that δ-crystallin synthesis begins at about 1.4 days of development. This is in good agreement with earlier biochemical analyses of the problem [5,6].

5.3 MICROSCOPE LASER LIGHT SCATTERING ON DEVELOPING CHICK LENSES

The preliminary experiments shown are of two types: MLLSS on explanted epithelial cells and MLLSS on a whole lens.

In the first case, the epithelial cells are peeled off the bulk of fiber cells. They form a monolayer of cells which is placed between coverslides with some physiologic buffer and some vacuum grease around the edges to prevent rapid drying out of the cells. Correlation functions are taken from cells close to the center of the epithelial layer and from cells close to the edge. The center cells should be "pure" epithelial cells that contain large organelles and a nucleus. The edge cells, if they were located equatorially (see Figure 5.1) relative to the germinative region, should have started the differentiation into fiber cells and could thus contain some δ-crystallin. Figure 5.5 shows correlation functions

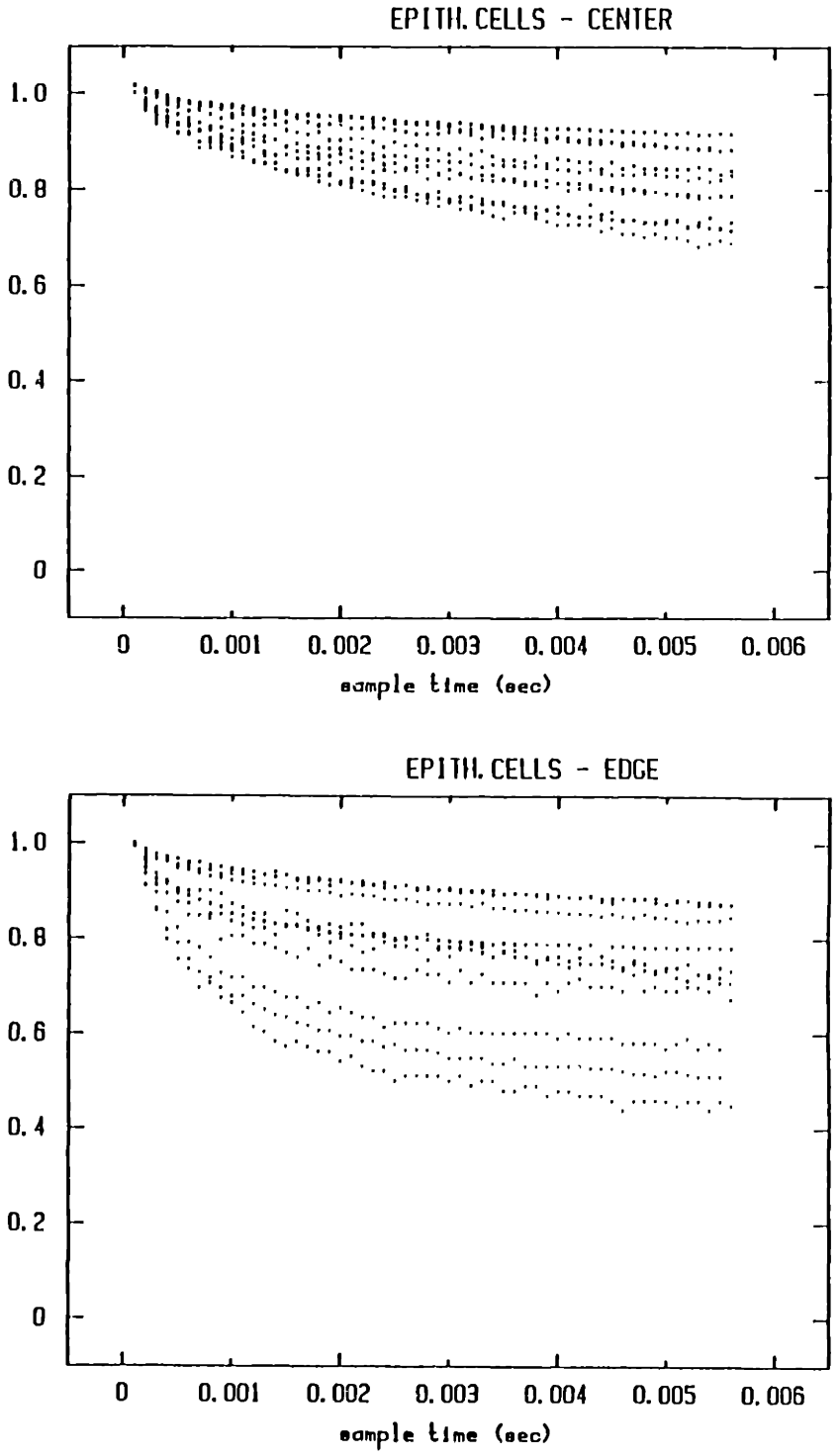

Figure 5.5 Intensity Autocorrelation Functions taken using small angle scattering on Epithelial Cells at the Center (top) and at the Edge (bottom) of the Epithelial Layer

taken on center and edge epithelial cells. On average, the edge cells do seem to show higher ratios R_δ, but some of the correlation functions at the edge seem to show only a slow decay.

In Figure 5.6 the correlation functions are taken from whole lenses. These experiments are very difficult to do, because the edges of the cells in the lens are hardly visible. This is of course expected since the eye lens should be very transparent to visible light. The functions shown were taken using the illumination from the top (large angle illumination) and focusing on the surface of the lens (epithelial cells ?) and on the inside of the lens (fiber cells). As I am not too sure of where exactly the correlation functions are taken from, I do not want to draw any conclusions from these data. I feel, however, that the quality of the correlation functions is sufficiently good to demonstrate the feasibility of performing MLLSS on lens cells.

REFERENCES

[1] R. Clayton; The eye, Volume 5; Academic Press, New York, 1974

[2] J. Piatigorsky; .....; Differentiation 19 , 134-..... , 1981

[3] J. Genis-Galvez et al.; .....; Exp.Eye Res. 7 , 593-...., 1968

[4] j. Piatigorsky et al.; Biology of the epithelial lens cells in relation to development, aging and cataract; Eds. Courtois & Regnault, Inst.Nat.de la Sante et de la Rech.Med. 60 , 85-104, 1976

[5] J. Zwaan et al.; .....; Exp.Eye Res. 7 , 301-..., 1968

[6] T. Shinohara et al.; .....; Proc.Natl.Acad.Sci.USA 73 , 2808-2812, 1976

Chapter 6 :

SUGGESTED IMPROVEMENTS TO THE MLLSS SET-UP AND PRELIMINARY DATA FOR FUTURE EXPERIMENTS

6.1 SUGGESTED IMPROVEMENTS TO THE MLLSS SET-UP

6.1.a. The laser focusing lens

In the present set-up, two ranges of angles are available: the forward angles (27° to 33°) and the backward angles (115° to 135°). This is a sufficiently wide range for most of the work one would want to do on the MLLSS set-up. Indeed, very precise characterization of a system of scatterers could require continuous scanning of scattering angles from a very small angle continuously to the backward angles. MLLSS is however not designed for this type of work, which would much more conveniently be done on the more conventional dynamic laser light scattering set-ups. What is inconvenient and calls for improvement though, is that the forward and backward angle configuration use different lenses to focus the incident laser beam. In some applications of MLLSS it is possible that one would want to extract a parameter which reflects the polydispersity of the system of scatterers. One would then first have to subtract the apparent polydispersity induced by the use of large numerical aperture lenses (see section 2.4.a and Figure 2.8). This could in principle be done for objective lenses such as the one

used in the top illumination. For the bottom illumination, which uses the condenser to focus the incident laser beam, it is much harder to asses the width of the cone of light collected for focusing. Moreover, the shape of the focal region made by the off-axis illumination of the condenser, is far from symmetric around the axis determined by the average incident beam direction. This complicated shape is slightly different for different alignments of the set-up in the bottom illumination configuration. Thus, assessing the apparent polydispersity as was done in section 2.4 would have to be done after each alignment, which is highly inconvenient. For this reason, it would be advisable to modify the set-up in such a way that one could easily move the condenser out of the way and illuminate the sample using an objective lens. This could possibly be done using the objective lens which is now used in the top illumination configuration only, for both positions.

6.1.b. The position control of the stage - Tiltable stage

The vertical positioning of the stage uses the original microscope image focusing mechanism which is satisfactory. The translation of the stage in the horizontal plane is, however, controlled by two linear translators of insufficient quality. Motion is inaccurately controlled with sticky translator screws. Better translators will soon be installed and will make the positioning of the image of the cell center underneath the end of the pick-up optical fibers much easier.

Presently, the microscope stage can not be tilted. It is clear from the data analysis in section 4.12 that the relative orientation of the bio-

logical cell and the scattering vector can be very important in the case of non-spherical cells with at least one dimension comparable to the linear dimension of the scattering volume. With the present set-up it is hardly possible to test if the Hb in normal RBCs aggregates at all at extremely low oxygen pressures (see section 4.6). This particular problem is just one example of a case in which it would be useful to tilt the sample, the RBC in this case, relative to the scattering vector.

6.1.c. The flow cell

It was mentioned that it is useful to always keep a microcapillary filled with a standard polystyrene solution next to the microcapillary containing the sample under study. In this way, the alignment can be checked during an experiment without having to remove the sample. When using the flow cell, this is presently impossible. It would be advisable to have a flow cell custom built which has a narrow chamber of the same thickness as the main chamber next to the part of the cell that has flow. In this way, the alignment could be checked during a flow experiment without removing the flow cell. This would be a useful improvement especially since it is a little cumbersome to mount and unmount the flow cell (see Figure 4.4)

6.1.d. Inverted microscope- Micro-manipulation

A much more major improvement than the ones discussed so far would be the use of an inverted microscope rather than an upright microscope as is used presently. This would not improve the quality of the measurements

from the optical point of view. Yet, the increased available space would facilitate the use of a better temperature control of the microscope stage. It would also make possible in an easier way than it would be on the present set-up, the addition of a micro-manipulator. This could be useful in several biological experiments.

6.2 SMALL STUDIES ON OTHER THAN RBCs OR LENS CELLS

6.1.a. MLLSS on the volume phase transition of submillimeter gels

The work presented here is partially to be published in Phys.Rev.Lett. by T.Tanaka, E.Sato, Y.Hirokawa, S.Hirose and J.Peetermans in a paper entitled "Critical kinetics of volume phase transition of gels". Only the data presented in Figure 6.3b and Figure 6.4 were taken by myself. The volume phase transition of submillimeter spherical isopropylacrylamide gels shows critical kinetic behavior near the critical point; the transition takes an infinite time, and the thermal expansion becomes infinitely large. At the critical point the gels also undergo internal critical density fluctuations as revealed by photon correlation spectroscopy. In 1979, it was demonstrated that the swelling process of a gel is determined by the diffusion of the polymer network into water rather than by that of water molecules into the polymer network [1]. The local motion of a polymer network obeys a diffusion equation in which the diffusion coefficient is defined by the ratio of the elastic modulus of the network, K, to the frictional coefficient, f, between the network and the fluid [2]. This diffusion process of the polymer network is called the collective diffusion of a gel [3]. The

concept of the collective diffusion successfully describes not only the kinetics of gel swelling but also the dynamics of density fluctuations of gels as observed by photon correlation spectroscopy [2,3]. The diffusion coefficients determined by macroscopic swelling experiments and by MLLSS have shown remarkable agreement.

In the paper stated above, we report the observation of the critical behavior of the kinetics of swelling and shrinking of spherical isopropylacrylamide gels (radius ranging from 100 μm to 1.5 mm) in response to temperature jumps: The characteristic time of swelling and shrinking of the gel becomes infinitely long and the thermal expansion coefficient diverges at 34°C for a network density of 0.192 g/ml. We also examined the internal density fluctuations of the gel beads using MLLSS. The density fluctuations also diverge and critically slow-down at the same temperature. The numerical value and temperature dependence of the diffusion coefficients determined by both kinetic and dynamic experiments coincide well. The observation of the critical kinetics constitutes strong evidence that the gel kinetics is governed by the collective diffusion of the polymer network rather than by the diffusion of water, since the pore size of the gel at the critical point remains much larger than the size of water molecules. The relaxation time for the gel volume after a temperature jump is proportional to the square of the gel radius and inversely proportional to the collective diffusion coefficient of the polymer network [1]. The collective diffusion coefficient also characterizes the thermal fluctuations of a polymer network. It can therefore be determined from the relaxation time of laser light intensity scattered from the density fluctuations of the gel. The values of D determined by the kinetic experiments (characteristic length of 100 μm) and the dynamic experiments (where the probing

characteristic length is that of the wavelength of light), are in excellent agreement.

The volume change of the gel beads was monitored under an optical microscope equipped with video camera and recorded on a video tape. The radius of the gel was then measured from the display image using a caliper. A typical time course of radius change is plotted in Figure 6.1 along with the corresponding temperature variation.

In Figure 6.2a the equilibrium radius of a gel bead is plotted as a function of temperature. The gel is swollen at lower temperatures and undergoes a sharp collapse at 34°C [4]. At this temperature the radius versus temperature curve has an infinite slope representing the critical point.

The relaxation time τ determined experimentally from the single exponential region of the volume change following a temperature jump is plotted as a function of temperature in Figure 6.2b. The relaxation time is finite except for the critical point where it appears to diverge. The thermal expansion coefficient, the relative radius change per temperature increment, also diverges at the critical point as shown in Figure 6.2c.

The relaxation time for the volume change of the gel bead after a temperature lump is proportional to the square of the radius. The proportionality constant gives the collective diffusion coefficient of the gel, which is plotted as a function of temperature in Figure 6.3a. It diminishes at the critical point.

In Figure 6.3b is plotted the collective diffusion coefficient of the gel determined from its thermal density fluctuations as revealed by MLLSS.

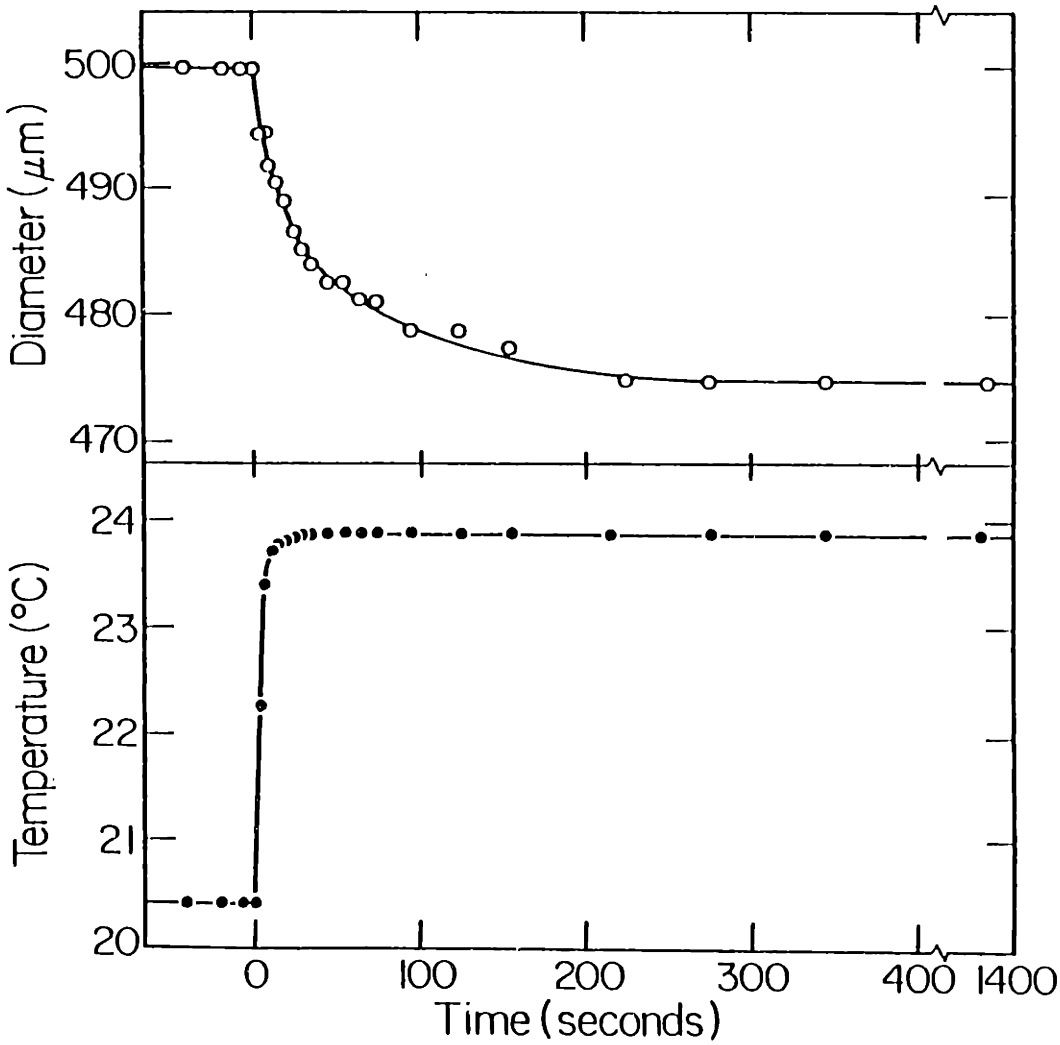

Figure 6.1 The time course of swelling of a submillimeter N-isopropylacrylamide gel bead in water is plotted in response to a sudden temperature jump. The lower curve shows the change of the temperature

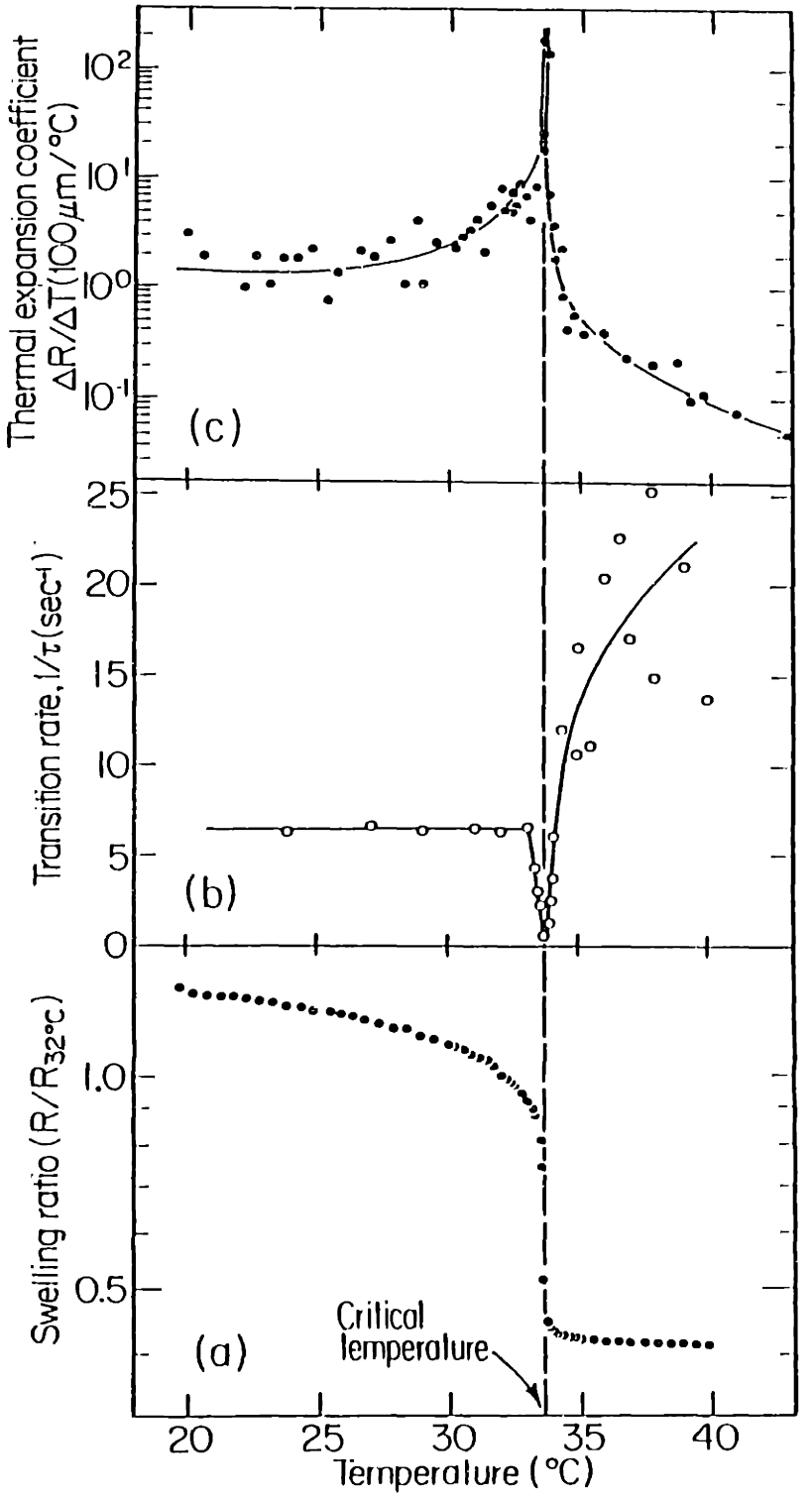

Figure 6.2 (a)Equilibrium radius of an isopropylacrylamide gel sphere is plotted as a function of temperature. At lower temperatures the gel is swollen and at higher temperatures the gel is shrunken. At about 34°C the swelling curve becomes infinitely sharp, which corresponds to the critical point.
(b)Relaxation time of gel volume change in response to a temperature jump is plotted as a function of temperature. The relaxation becomes infinitely slow at the critical point.
(c)Thermal expansion coefficient, the relative radius change per temperature increment, also diverges at the critical point.

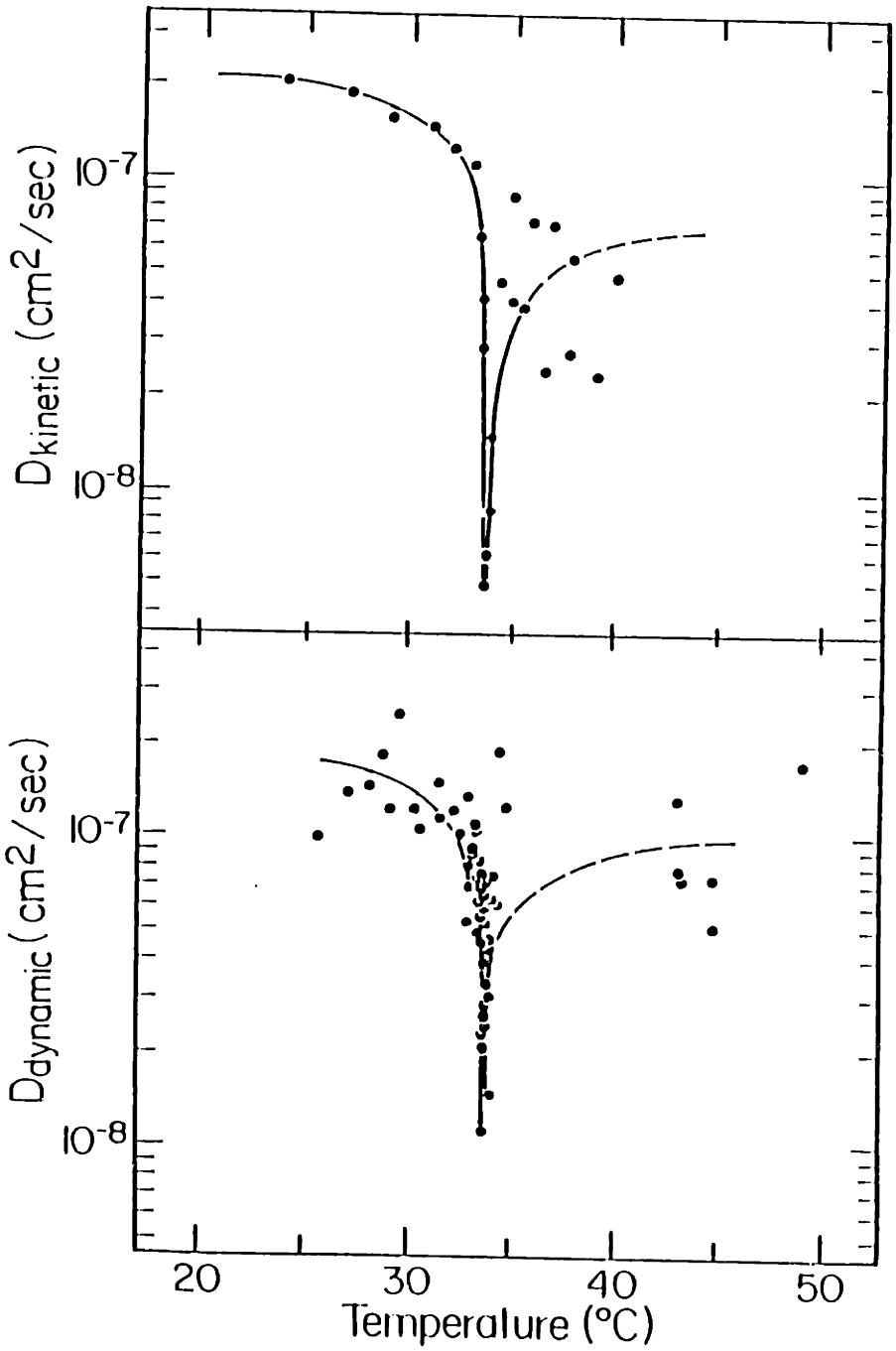

Figure 6.3 (a)Collective diffusion coefficient D of a N-isopropylacrylamide gel as determined by the kinetics of volume change is plotted as a function of temperature. It diminishes at the critical point.
(b)Collective diffusion coefficient as determined from the density fluctuations using photon correlation spectroscopy. The agreement between the results obtained from dynamics of microscopic fluctuations and from kinetics of macroscopic volume change is excellent considering the difficulty in the dynamic experiments

The agreement between the results obtained from the dynamics of microscopic density fluctuations and the kinetics of macroscopic volume change is excellent considering the difficulty of the spectroscopic measurements. The result confirms the previous observation of critical slowing-down of the density fluctuations of acrylamide gels [5-7].

Figure 6.4 shows the signal to background ratio or AC/DC ratio for the correlation functions collected using MLLSS as a function of temperature. The AC/DC ratio is proportional to the compressibility of the gel. In the swollen state, the gel is relatively soft and the amplitude of polymer motion is large. Correspondingly, the AC/DC ratio is relatively large in this regime and grows at the critical point where critical density fluctuations occur on very large length scales and the sample turns temporarily opaque. After the transition into the collapsed state, the gel bead is relatively hard and the polymer motion has smaller amplitude; the AC/DC ratio is much decreased. Though the spread on the data is large in this regime, this feature is clearly seen.

6.1.b. MLLSS on a granule secreting cell, the pancreatic acinar cell

The work presented in this section is to be published soon by J.Peetermans, E.K.Matthews, I.Nishio and T.Tanaka in a paper entitled "Direct observation of intracellular particle motion inside single acinar cells using microscope laser light scattering spectroscopy". It reports the direct observation of translational diffusion of cytoplasmic subcellular organelles and macromolecules within single, metabolically active, pancreatic acinar cells using MLLSS. The relative amount and the diffusion

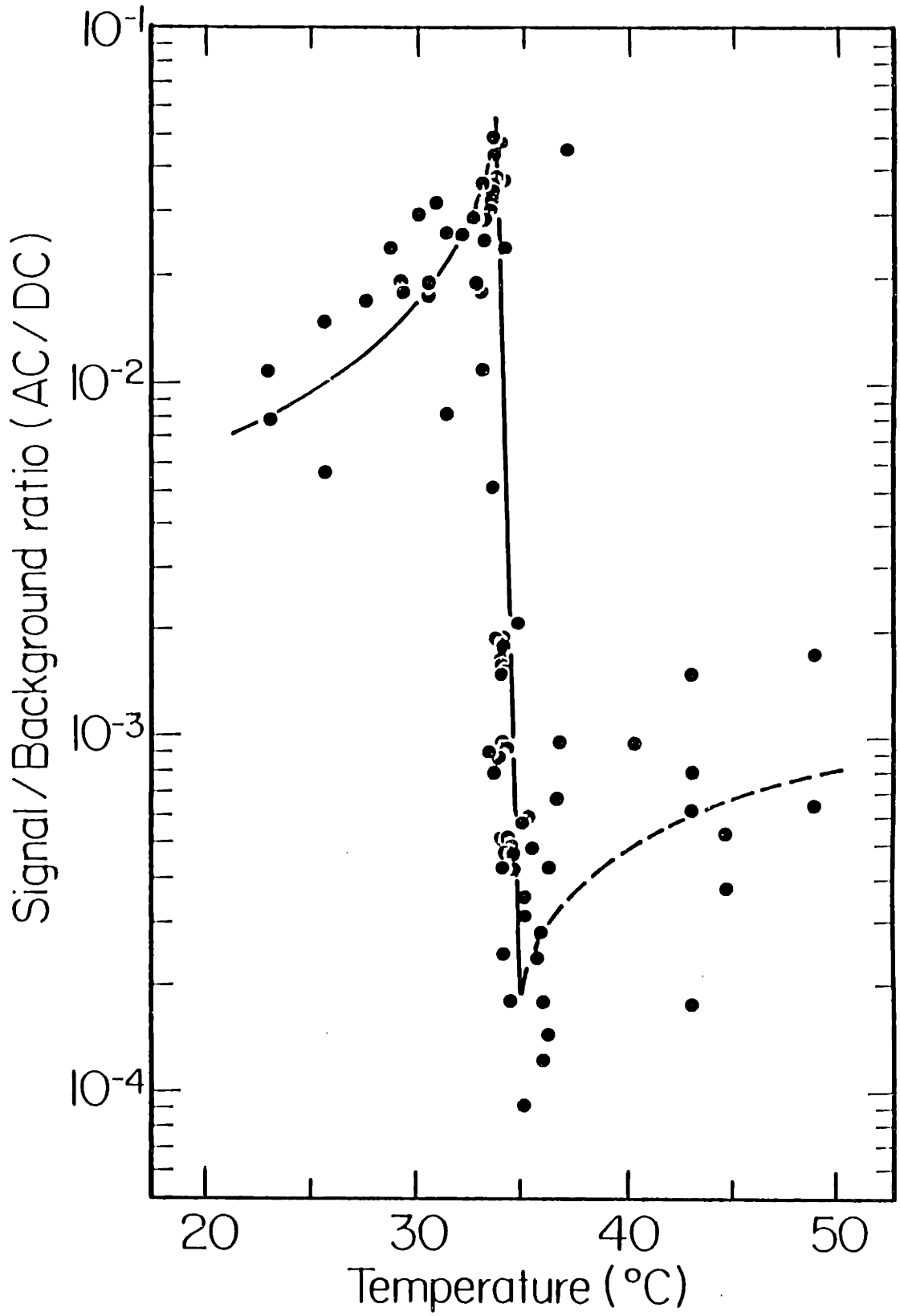

Figure 6.4 Signal to background ratio or AC/DC ratio as a function of temperature for the intensity autocorrelation functions collected using MLLSS. The AC/DC ratio is proportional to the compressibility of the gel

coefficient of the mobile particles shows a marked difference in magnitude between the apical and basal regions of the cell and secretory stimulation evoked by the cholinergic agonist bethanechol, as well as osmotic swelling of the cells, induces changes in the Brownian motion in the cytoplasm. This study demonstrates the feasibility and utility of MLLSS for the analysis of intracellular events in single granule secreting, cells.

Cellular secretory mechanisms have attracted wide spread attention. A large number of models have been proposed to describe the process of secretion which in many cells involves a calcium-dependent exocytosis of preformed storage granules. Significant changes in the translocation of ions and the state of the cytoplasm may be associated with the secretory process [8].

We present here the first report of a study with MLLSS on, granule secreting, cells, those of the mammalian pancreatic acinus. Pancreatic acinar cells release their digestive enzyme content by exocytosis of zymogen granules upon stimulation with cholinergic agonists such as bethanechol. The response to the stimulus is generally assessed by measuring the amount of enzyme released into the suspension medium of the acinar cells following stimulation. Such a response is, however, an average over a large number of cells, so that it remains unknown if all cells have the same threshold for stimulation and similar kinetics of secretion, or if only a certain fraction of the cells secrete, while others remain relatively unresponsive. Using MLLSS, we were able to detect differences in the movement of intracellular particles between the zymogen granule containing apical region and the basal region of the acinar cells by analyzing the time dependent fluctuations of light scattered from these discrete sub-

cellular regions of single, metabolically active cells. Altering the composition of the suspension medium was found to influence subcellular particle motion within single acinar cells.

Dissociated pancreatic acinar cells from Sprague-Dawley rats of 150-250g wt were prepared essentially by the technique of Amsterdam and Jamieson [9]. The dissociated cells were washed three times with Krebs solution (without Ca^{++}) and suspended in oxygenated medium of similar composition. For some experiments the medium was decreased in osmolarity to 50% by dilution with distilled water; in other experiments the Krebs solution was supplemented with Ca^{++} (2.56 mM) and bethanechol (2x10 sup {-4}M). The isolated cells were maintained at 37°C on a temperature-controlled stage for study by MLLSS.

The average diffusion coefficient $\overline{D}$ and the intensity ratio R (see Eq.2.31) are discussed in this report. Figure 6.5 is a diagram of an acinar cell viewed with an optical microscope. Two distinct regions are seen: the apical region within which most granules are stored, and the more transparent looking, "clear" basal region. The nuclear region was avoided in gathering the data. An optical fiber, embedded in one of the eyepieces, was used to pick up the scattered light and guide it to the detection system for photon correlation spectroscopy. It is shown on Figure 6.5. Figure 6.6 shows single cell intensity autocorrelation functions taken in the basal and the apical regions. There is a marked difference between the correlation functions obtained from the two regions. The functions collected from basal regions decay substantially, whereas the functions taken from apical regions show little if any decay. This may be interpreted as follows. The cells, even those primed for secretion, contain a pool of

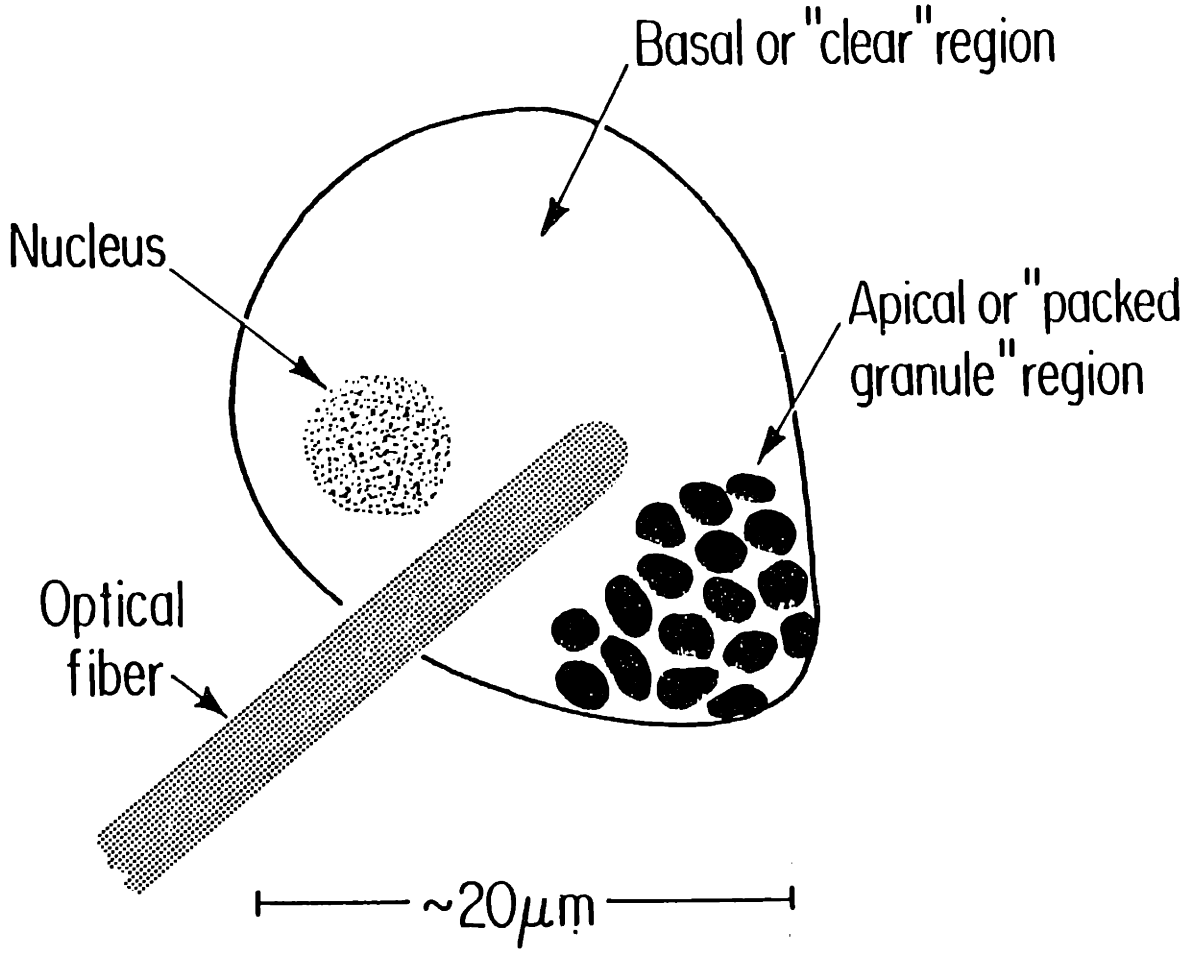

Figure 6.5 Diagram of a pancreatic acinar cell showing the "packed granules", apical and the "clear" basal regions of the cell, and the cell nucleus. The optical fiber pick-up for the scattered light is also shown

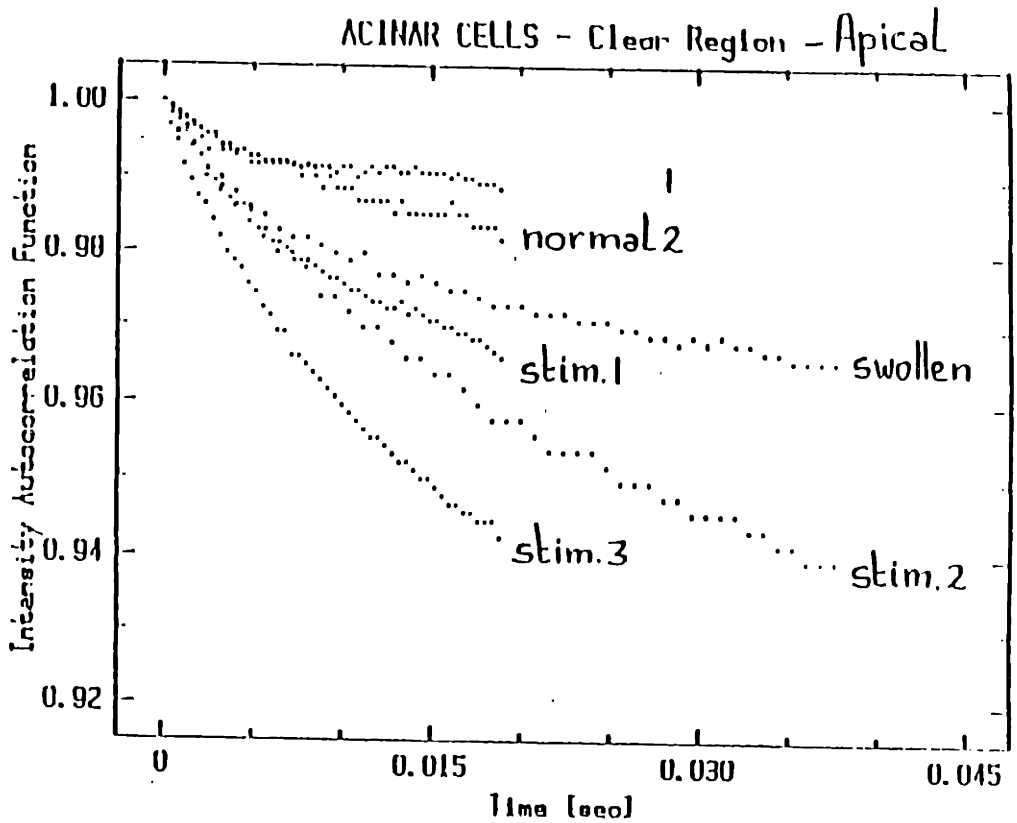

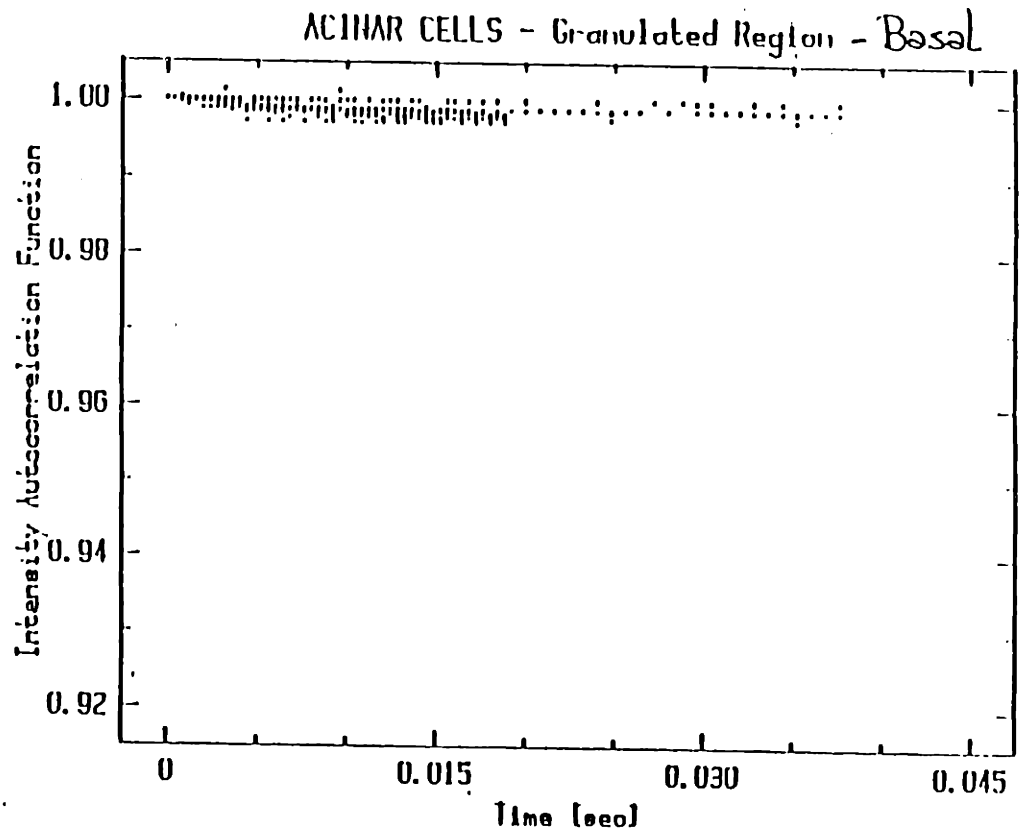

Figure 6.6 Intensity autocorrelation functions collected on the apical (top) and basal (bottom) region of the acinar cells at the same scattering angle (21°).

granules which are closely packed in one aspect of the cell with restricted freedom of motion. In the basal regions, intracellular proteins and small organelles together with some granules, are more free to move. Accordingly, the intensity autocorrelation functions collected from these basal regions show appreciable decay.

We studied the cells in three different suspension media: a solution with no added Ca^{++} or secretory stimulant (unstimulated cells), a low osmolarity solution (swollen cells) and a solution containing bethanechol and Ca^{++} (stimulated cells). The correlation functions obtained in the basal regions of unstimulated cells decay at a slower rate than the functions of the corresponding region of stimulated and swollen cells (see Figure 6.6 top). This indicates that the translational diffusion of intracellular macromolecules becomes greater in the cells exposed to bethanechol or in those that were swollen.

The average diffusion coefficient $\bar{D}$ of the basal region and the relative intensity of mobile scatterers R_I for the basal and the apical regions derived from the correlation functions of Figure 6.6 are given in the table below. The value of R_I is systematically higher in the basal region than in the apical region, indicating relatively more mobile scatterers in the basal region of the acinar cells. The average diffusion coefficient $\bar{D}$ is somewhat higher in the swollen cell and is increased 2 to 3-fold in the stimulated compared to the unstimulated cells.

In future studies it should be possible to determine, using the flow cell for medium transfer, and by autocorrelation at different scattering angles, the magnitude of granule translocation within the apical region itself before and after stimulation of the same cell.

Cell	$\bar{D}_{basal}$ (cm^2/sec)	$R_{I\ basal}$	$R_{I\ apical}$
normal 1	3.53×10^{-9}	0.190	0.021
normal 2	3.54×10^{-9}	0.108	0.036
swollen	5.02×10^{-9}	0.118	0.013
stimulated 1	7.35×10^{-9}	0.155	0.091
stimulated 2	6.31×10^{-9}	0.130	0.030
stimulated 3	11.3×10^{-9}	0.131	0.003

In conclusion, we have demonstrated that measurement can be made by MLLSS of Brownian motion in pancreatic acinar cells. The difference in signal between the "clear" basal and "packed granule" or apical regions of one individual cell is striking. Also, some changes can be detected in the data obtained from the basal region as the cells are exposed to suspension medium of different composition. These results clearly demonstrate the usefulness of MLLSS for non-invasive intracellular analysis and pave the way for a high spatial resolution study of events in discrete regions of single, metabolically active, secretory cells.

6.1.c. MLLSS in progress on some other cells

I wish to briefly mention four so far unmentioned cell types on which we are presently working.

RBCs of people that have **diabetes** are known to have enhanced stickiness of hemoglobin to the inner walls of the cell membranes. This is the result of a chemical alteration of the hemoglobin of which a fraction is glycosylated (has sugar groups attached). Clinically, it is known that diabetes patients can develop much decreased blood flow mostly in extremities. Some believe that the glycosylated hemoglobin stuck to the cell membrane is responsible for increased cell rigidity and thus decreased blood flow. This is however still a matter of controversy [10-12]. We feel MLLSS may contribute interesting information in this field.

Macrophages are crawling cells with a strong cytoskeletal structure [13]. Several mechanisms have been proposed to explain how such cells crawl. Many of them contain the idea that the cytoskeleton can locally melt, allowing the cell to change its shape in that region, for example extend a leg or pseudopod. We are trying to use MLLSS to establish if such local "phase transitions" of the skeleton indeed are observed and, if so, to investigate their reversibility.

Intracellular granules such as the ones found in the acinar cells discussed above, contain extremely concentrated solutions of the secretory material that they are the stock area of. It is un unanswered question how a biologic cell manages to maintain such "condensated" solutions. We are investigating this problem on granules that are secreted from the epithelial cells of a particular slug type. These granules contain very highly concentrated mucus which is released to humidify the outer surface of the slug.

In organ transplantation, the first important issue is the acceptability of the organ by its new host. If the immune system of the host is

incompatible with the new organ, a very much increased level of certain **lymphocytes** will cause the rejection of the organ. Prior to an organ transplantation, mixed lymphocyte cultures are studied that contain cells from both host and donor. In case of organ rejection, the lymphocytes undergo a differentiation into a proliferating cell type capable of totally destroying the function of the new organ. We are trying to detect early changes in the Brownian motion of the intracellular components of such differentiating lymphocytes.

REFERENCES

[1] T.Tanaka et al.; Kinetics of swelling of gels; J.Chem.Phys. 70, 1214-1218, 1979

[2] T.Tanaka et al.; Spectrum of light scattered from a viscoelastic gel; J.Chem.Phys. 59 5151-5159, 1973

[3] J.P.Munch S.Candau, R.Dupiessix, C.Picot, J.Herd and H.Benoit, J.Polym.Sci., 14 1097 (1976)

[4] Y.Hirokawa et al.; Volume phase transition in a nonionic gel; J.Chem.Phys. 81, 6379-6380, 1984

[5] T.Tanaka et al.; Critical behavior of density fluctuations in gels; Phys.Rev.Lett. 38, 771-774, 1977

[6] T.Tanaka; Dynamics of critical concentration fluctuations in gels; Phys.Rev.A 17, 763-766, 1978

[7] A.Hochberg et al.; Spinodal line and critical point of an acrylamide gel; Phys.Rev.Lett. 43, 217-219, 1979

[8] E.K. Matthews, Secretory Mechanisms, S.E.B. Symposium XXXIII, ed. Hopkins and Duncan, Cambridge University Press (1979)

[9] A. Amsterdam and J.D. Jamieson, J.Cell.Biol., 63, 1037-1056, 1974

[10] Y. Baba et al.; Higher levels of erythrocyte membrane microviscosity in diabetes; Diabetes 28, 1138-1140, 1979

[11] D.McMillan et al.; Reduced erythrocyte deformability in diabetes; Diabetes 27, 895-901, 1978

[12] A.Barnes et al.; Is hyperviscosity a treatable component of diabetic microcirculatory disease?; Lancet Oct 15, 789-791, 1977

ACKNOWLEDGEMENTS

This thesis represents a piece of work that I could not have accomplished without the help and company of a large group of people. In the specific context of this thesis work, I wish to thank very warmly Toyo Tanaka and Izumi Nishio, respectively my advisor and postdoc for my Ph.D. research. Toyo's enthusiasm and optimism were a continuous source of encouragement, his scientific insight and the freedom he gave me in my work were always a source of stimulation. Izumi was really my big brother throughout this work: the one who was always there, both at times of success and at times of discouragement, the one who's inspiration I followed, the one who made figures 2.7 and 4.4 for me, the one who invested in me an incredible amount of unselfish time and effort. Both of you, Toyo and Izumi, were great teachers who I will always remember with a lot of fondness and respect.

When I joined Toyo's group two and a half years ago, Shao-Tang Sun and Gerry Swislow were there. They, together with Izumi and Toyo, welcomed me into this new place with great generosity, making it possible for me to start work quickly and feel at home in Toyo's labs. Thank you for your warm welcome and the great companionship after that.

Many other people worked in these labs during my thesis research and all of them contributed to the atmosphere which was always pleasant and friendly. In particular, I wish to thank Yoshi Hirokawa, Jaro Ricka, Eriko Sato, Yoshiharu Hirose, Taka Amiya, Giulio Giannetti and

Shun Hirotsu for their nice company in the group. I also greatly enjoyed the occasional working sessions with Yuri Imanishi and Tsuyoshi Ohnishi. Yong Li was very special to me in the recent months in the lab. Thank you, Yong, for your friendship and for the kind and friendly help which you gave me numerous times.

Co-students and postdocs, past and present, were important throughout my years on the second floor of building 13. Through the shared atmosphere and surroundings, I feel quite a bit of closeness to them. Some were truly friend through it all: to George Thurston, Zoran Djordjevic, Loretta Mengel and Solange Akselrod, my very sincere thanks for your support in hard times and your sharing of good times. I wish to express also my sincere gratitude to George Benedek who has been an important teacher and professional father to me.

Richard Cohen and Tom Greytak were great readers at my thesis defense, I appreciated their comments and suggestions very much. Finally, before leaving the second floor, I wish to thank for an infinite number of friendly services rendered, Patti Jones, Bill Billings, Barbara Fox, Lisa Payne, Frank Payne and John Mara.

In my personal life, so many friends and family members really deserve my thanks. I hope not to insult those of you who were so important to me throughout the years and will not find their names here, but I shall restrain myself to personalized acknowledgements to my grandparents Edgar and Yvonne Peetermans and Frans and Jeanne Nuyens, to my aunt and her family, Dora, Hans and Anne Silvester, to Lizy Nuyens, to Betty and Frans Clemens, to Francine Bosselaar and Laure-Anne Muller, to Adam and Andree Telerman, all of whom were very substantial in

expressing, one way or another, continuous interest and faith in what I was doing. To all of you, my warmest thanks.

Last and most of all, I am very grateful to my parents, Lea and Marc Peetermans for the unconditional support and encouragement they gave me throughout my graduate years. But maybe even more than your support, Mamy and Marc, you gave me during all this time the motivation and urge to accomplish which gave me the necessary energy to continue when times were hard and added enjoyment when things went well. To you, Jan, my brother, thank you for the loving attention I always received from you, for the comforting words you gave me at times in which it was hard not to be closer to home. And to you, Seth, my boy friend and husband through it all, thanks for your love, company, help, all combined and omnipresent, giving me always a place to turn and share all of the emotions that graduate school contains. Mamy, Marc, Jan and Seth, thanks to you there was never solitude in the realization of this work.

Appendix II-1 :

SINGLE MODE OPTICAL FIBERS (see p.25)

The critical angle

The refractive index n_1 of the core is larger than the refractive index n_2 of the cladding (see Figure 2.2.a): $n_1 > n_2$. Refraction of a beam incident from the core at an angle θ_1 into the cladding at an angle θ_2 obeys Snell's law: $n_1 \sin\theta_1 = n_2 \sin\theta_2$. When $\sin\theta_2 = 1$ (refraction parallel to the interface), $\sin\theta_2 = n_2/n_1$. At this point the incident angle θ_1 is the **critical angle** θ_c:

$$\theta_c = \text{Arcsin}\,\frac{n_2}{n_1}. \qquad (1)$$

All light hitting the interface at $\theta_1 > \theta_c$ undergoes total internal reflection and is thus trapped inside the core of the optical fiber.

Numerical aperture of the fiber

How large can the angle θ_o at which light impinges onto the optical fiber core from outside the fiber, be for the incident light to be totally refracted into the fiber core (see Figure 2.2.a)? Snell's law at the entrance of the fiber core and at the core-cladding interface yields

$$n_o \sin\theta_o = n_1 \sin\theta_i = n_1 \cos\theta_1 = n_1 (1 - \sin^2\theta_1)^{1/2}. \qquad (2)$$

Thus the maximum exterior incidence angle $\theta_{o_{max}}$ is given by

$$n_o \sin\theta_{o_{max}} = n_1 (1 - \sin^2\theta_c)^{1/2} = n_1 (1 - n_2^2/n_1^2). \qquad (3)$$

This yields the definition of the **numerical aperture** of an optical fiber:

$$NA_{fiber} = \left[n_1^2 - n_2^2\right]^{1/2} \qquad (4)$$

Modes in a fiber

Consider parallel rays of light somewhere in the fiber core. Some will interfere constructively, others destructively. The figure below helps illustrate this point.

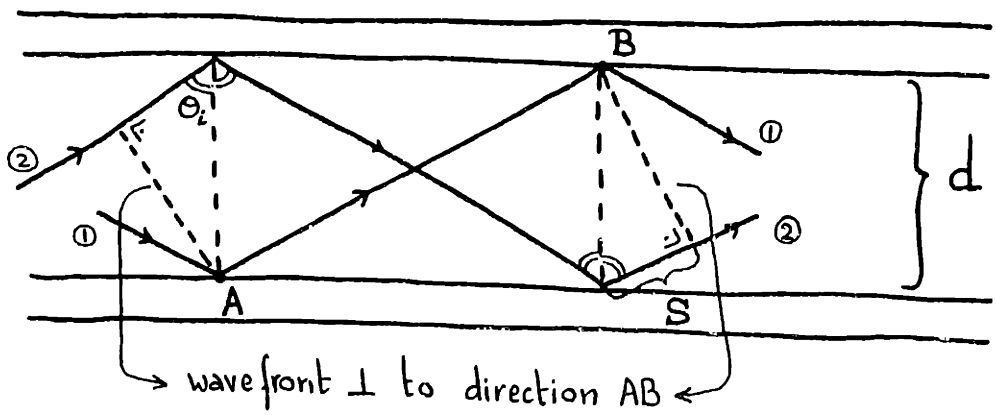

By the time the bottom ray (1) has traveled from point A to point B, its "partner" ray (2) has traveled a longer distance, namely the distance AB plus 2 x S where $S = d \cos\theta_i$. Thus the optical path difference OPD is $OPD = 2 n_1 d \cos\theta_i$. If the wavefront of which rays (1) and (2) are part, has wavevector k, then the phase difference between the two rays is

$$\Phi_{OPD} = 2\, n_1\, d\, k \cos\theta_i . \qquad (5)$$

There is constructive interference for $\Phi_{OPD} = 2\, m\, \pi$ where m is an integer. The maximum value for m is found for $\theta_i = \theta_c$: $m_{max} = M$:

$$M = \frac{n_1\, k\, d}{\pi} \cos\theta_c = C\, \frac{d}{\lambda}\, NA_{fiber} . \qquad (6)$$

The exact value of the constant C depends on the geometry of the fiber. For round fiber, $C = 2\,\pi$. The definition of a **single mode fiber** is given as

$$\text{single mode fiber} : M < 1. \qquad (7)$$

Typically $2\,\pi\, d\, NA\, /\, \lambda < 2.4$, thus single mode fibers typically have small diameter d and small numerical aperture NA.

The specifications of our case

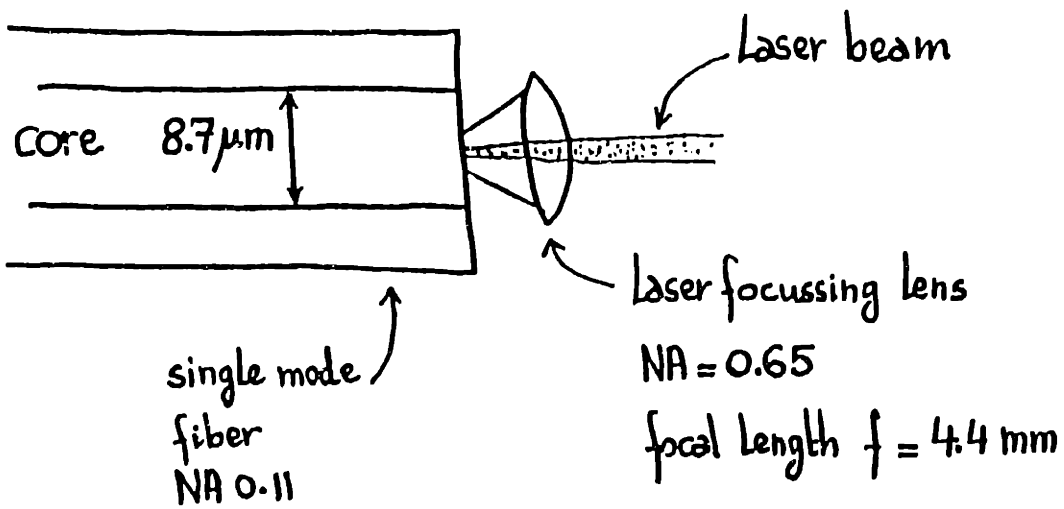

The NA of the laser focusing lens is >> NA of the single mode fiber and thus the acceptance angle of the fiber is << than the angle at which the focussed laser beam comes into the fiber. However, not too much

light is lost, because the laser beam diameter is ~ 1/7 of the lens diameter and thus the angle at which the beam comes onto the fiber entrance is much smaller than for a beam of the diameter of the lens:

The lens : NA = 0.65 (angular spread 80°)

focal length 4.4 mm

thus lens diameter ~ 7 mm

and angular spread on focussed laser beam ~ 11.5°

The fiber : NA = 0.11 (angular spread 12.5°)

11.5° < 12.5° thus the only loss is due to reflection at the glass-air interface.

Appendix II-2 :

COHERENCE AREA IN A QLS EXPERIMENT (see p.43)

The path length difference for two rays originating from the points A and B in the cylinder of light formed by the laser beam in the sample is

$$L \sin\theta + a \left|\cos\theta\right| \qquad (1)$$

where A and B are in the plane formed by the incident laser beam and the detected scattered beam. Additional path length difference originates from the thickness a of the sample in the direction perpendicular to this plane. The ratio of each of these path length differences and the wavelength of light determine the coherence solid angle

$$\Omega_{coh} = \frac{\lambda^2}{a\ (L \sin\theta + a \left|\cos\theta\right|)} \qquad (2)$$

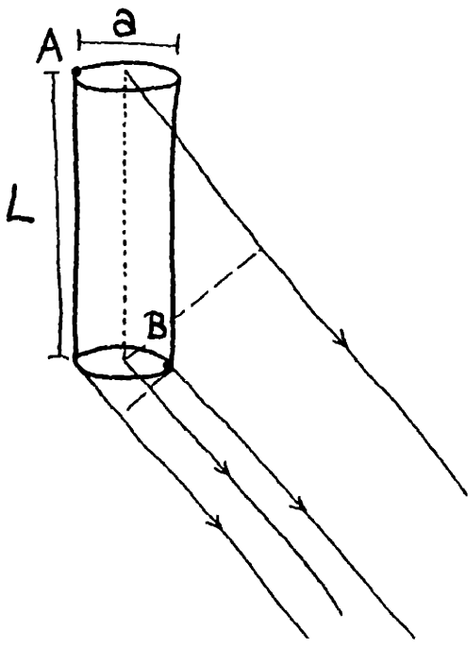

Appendix II-3 :

INTENSITY AUTOCORRELATION FUNCTION FOR MLLSS ON BIOLOGICAL CELLS (see p.53)

We wish to prove Eq.2.19 which gives the intensity autocorrelation function $c_I(\tau)$ as a function of the total average scattered intensity corresponding to the moving and the immobile particles, respectively I_m and I_{imm}, and as a function of the field autocorrelation function $g(\tau)$ of the electric field scattered by the mobile particles:

$$c_I(\tau) = (I_m + I_{imm})^2 + A\,(g(\tau)^2\, I_m^{\,2} + 2\, g(\tau)\, I_m\, I_{imm}) \qquad (1)$$

The intensity measured on the detector surface at time t is the sum of the intensities measured on individual coherence areas of which there are N:

$$I(t) = \sum_{i=0}^{N} I_i(t) = \sum_{i=0}^{N} E_i(t) E_i^{*}(t) \qquad (2)$$

where the vector signs were omitted for simplicity in notation. Substitution into the definition of the intensity autocorrelation function yields

$$c_I(\tau) = \langle I(t) I^{*}(t+\tau) \rangle \qquad (3)$$

$$= \sum_{i=0}^{N} \sum_{j=0}^{N} \langle I_i(t) I_j^{*}(t+\tau) \rangle$$

$$= \sum_{i=0}^{N} \sum_{j=0}^{N} \langle E_i(t) E_i^*(t) E_j(t+\tau) E_j^*(t+\tau) \rangle$$

In this double sum, there are N^2 terms for which $i \neq j$. In this case, the average of the product of four fields can be rewritten simply as

$$\sum_{i=0}^{N} \sum_{j=0}^{N} \langle E_i(t) E_i^*(t) E_j(t+\tau) E_j^*(t+\tau) \rangle \quad \text{for } i \neq j \tag{4}$$

$$= N^2 \langle E(t) E^*(t) \rangle^2$$

where $E(t)$ refers to the electric field that reaches just one coherence area. For $i = j$ in the double sum of Eq.3, there are N terms which can be rewritten as

$$\sum_{i=0}^{N} \sum_{j=0}^{N} \langle E_i(t) E_i^*(t) E_j(t+\tau) E_j^*(t+\tau) \rangle \quad \text{for } i = j \tag{5}$$

$$= N \langle E(t) E^*(t) E(t+\tau) E^*(t+\tau) \rangle .$$

At this point, it is necessary to introduce a more specific form for the electric field. It is also given in Eq.2.16

$$E(t) = E_m(t) + E_{imm}(t) = E_m(t) + E_{imm} , \tag{6}$$

the sum of the field scattered by mobile and by immobile scatterers. The field scattered by immobile particles is time independent. Eq.4 yields a simple expression:

$$N^2 \langle E(t) E^*(t) \rangle^2 \tag{7}$$

$$= N^2 \langle (E_m(t) + E_{imm}) (E_m^*(t) + E_{imm}^*) \rangle^2$$

$$= N^2 \left[< E_m(t) E_m^*(t) > < E_{imm} E_{imm}^* > \right]^2$$

$$= N^2 \left[I_m + I_{imm} \right]^2$$

where the following notation was used:

$$< E_m(t) E_m^*(t) > = < I_m(t) > = I_m \tag{8}$$

$$< E_{imm} E_{imm}^* > = < I_{imm} > = I_{imm} \, . \tag{9}$$

The terms containing a factor of the type $< E_m(t) E_{imm}^* >$ are zero because they contain a factor $< e^{i\omega t} >$ which is zero due to the time average. Eq.5 is a little more complicated.

$$N < E(t) E^*(t) E(t+\tau) E^*(t+\tau) > \tag{10}$$

$$= N < (E_m(t)+E_{imm}) (E_m^*(t)+E_{imm}^*) (E_m(t+\tau)+E_{imm}) (E_m^*(t+\tau)+E_{imm}^*) >$$

$$= N \left[< E_m(t) E_m^*(t) E_m(t+\tau) E_m^*(t+\tau) > + I_m I_{imm} \right.$$

$$+ < E_m(t) E_{imm}^* E_{imm} E_m^*(t+\tau) > + < E_{imm} E_m^*(t) E_m(t+\tau) E_{imm}^* >$$

$$+ < E_{imm} E_{imm}^* E_m(t+\tau) E_m^*(t+\tau) >$$

$$\left. + < E_{imm} E_{imm}^* E_{imm} E_{imm}^* > \right]$$

$$= N \left[\text{first term} + 2 \, I_m I_{imm} + 2 \, g(\tau) I_m I_{imm} + I_{imm}^2 \right]$$

where the normalized field autocorrelation function $g(\tau)$ is defined as

$$g(\tau) = \frac{< E_m(t)E_m^*(t+\tau) >}{< E_m(t)E_m^*(t) >} = \frac{< E_m^*(t)E_m(t+\tau) >}{< E_m^*(t)E_m(t) >} . \qquad (11)$$

The first term is the average of a product of 4 values of one Gaussian random variable. Such a product can be written as the sum of 3 terms that contain only averages of 2 values of the Gaussian random variable. This is demonstrated at the end of this Appendix. Through this factorization, the first term can be rewritten as

$$\begin{aligned} &<E_m(t)E_m^*(t)E_m(t+\tau)E_m^*(t+\tau)> \qquad (12)\\ &\quad = < E_m(t)E_m^*(t) >< E_m(t+\tau)E_m^*(t+\tau) > \\ &\quad\quad + < E_m(t)E_m(t+\tau) >< E_m^*(t)E_m^*(t+\tau) > \\ &\quad\quad + < E_m(t)E_m^*(t+\tau) >< E_m^*(t)E_m(t+\tau) > \end{aligned}$$

The first term yields I_m^2. The second term is zero because the electric field can be written as $E_m(t) = E_m^o(t)e^{i\omega t} = E_o\, e^{i\vec{k}\cdot\vec{r}_m(t)}\, e^{i\omega t}$. Thus the second term contains a factor of the type $< e^{2i\omega t} >$ which is zero. The third term yields $(g(\tau)I_m)^2$. Putting all the terms together, one obtains

$$c_I(\tau) = (N^2+N)\ (I_m+I_{imm})^2 + N\,(2g(\tau)I_mI_{imm} + g^2(\tau)I_m^2) \qquad (13)$$

Finally, introducing the total intensity measured from mobile and immobile scatterers and using the notation $I_m = NI_m$ and $I_{imm} = NI_{imm}$, one obtains the equation that had to be proven with

$$A = \frac{1}{1+N} \qquad (14)$$

Factorization of the average of the product of 4 Gaussian random variables

We wish to prove that the average of the product of 4 values of a Gaussian random variable $X(y)$ can be written as follows:

$$\begin{aligned} \langle X(y_1)\, X(y_2)\, X(y_3)\, X(y_4) \rangle &= \langle x_1 x_2 x_3 x_4 \rangle \\ &= \langle x_1 x_2 \rangle \langle x_3 x_4 \rangle \\ &\quad + \langle x_1 x_3 \rangle \langle x_2 x_4 \rangle + \langle x_1 x_4 \rangle \langle x_2 x_3 \rangle \end{aligned} \tag{15}$$

Make a column vector $\bar{x} = (x_1, x_2, x_3, x_4)$ and a similar vector $\bar{z}$ such that $x_i z_j$ is dimensionless. Define the mean or ensemble average of a variable X as

$$\langle X \rangle = \int_{-\infty}^{+\infty} X\, f(X)\, dX \tag{16}$$

where the distribution function $f(X)$ for a Gaussian random variable centered at zero, is given by

$$f(X) = \frac{1}{(\sigma(2\pi)^{1/2})^n}\, e^{-x^2/2\sigma^2} \tag{17}$$

where n is the dimension of the vectors $\bar{x}$ and $\bar{z}$. We now demonstrate that

$$\langle e^{i\bar{x}\cdot\bar{z}} \rangle = e^{-1/2 \sum_{ij} z_i z_j \langle x_i x_j^* \rangle} \tag{18}$$

PROOF:

$$< e^{i\bar{x}\cdot\bar{z}} > = \int_{-\infty}^{+\infty} \frac{1}{(\sigma(2\pi)^{1/2})^n} e^{-x^2/2\sigma^2} e^{i\bar{x}\cdot\bar{z}} d\bar{x} \qquad (19)$$

$$= e^{-\sigma^2 z^2/2}$$

It thus remains to be proven that

$$z^2\sigma^2 = \sum_{ij} z_i z_j <x_i x_j^*> \qquad (20)$$

The proof will be written out for the 4 dimensional case, which is the one we are here interested in, but the proof is identical for any dimension n.

$$\sum_{i,j=1}^{4} z_i z_j <x_i x_j^*> = \sum_{i,j=1}^{4} z_i z_j \int_{-\infty}^{+\infty} \prod_{k=1}^{4} dx\, x_i x_j^* \frac{1}{(\sigma(2\pi)^{1/2})^4} e^{-\sum_{l=1}^{4} x_l^2/2\sigma^2}$$

$$= \sum_{i=1}^{4} z_i^2 \int_{-\infty}^{+\infty} dx_i |x_i|^2 \frac{1}{\sigma(2\pi)^{1/2}} e^{-x_i^2/2\sigma^2}$$

$$= \sum_{i=1}^{4} z_i^2 \sigma^2$$

$$= z^2 \sigma^2$$

We now rewrite Eq.18 in the 4 dimensional case and expand each side in a series of terms. The left hand side yields:

$$< e^{i\bar{x}\cdot\bar{z}} > = < e^{i\sum_{j=1}^{4} z_j x_j} > \qquad (22)$$

$$= < 1 + i \sum_{j=1}^{4} z_j x_j - \frac{1}{2}\Big(\sum_{j=1}^{4} z_j x_j \Big)^2 - \frac{i}{3!}\Big(\sum_{j=1}^{4} z_j x_j \Big)^3 + \ldots$$

$$= \ldots + \frac{24}{4!} z_1 z_2 z_3 z_4 < x_1 x_2 x_3 x_4 > + \ldots$$

The term of the last line is the only term containing the factor $z_1 z_2 z_3 z_4$. The left hand side of Eq.18 is

$$e^{-1/2 \sum_{i,j=0}^{4} z_i z_j <x_i x_j^*>} = 1 - \frac{1}{2} \sum_{i,j=0}^{4} z_i z_j <x_i x_j^*> \qquad (23)$$

$$+ \frac{1}{2^2\, 2!} \left[\sum_{i,j=0}^{4} z_i z_j <x_i x_j^*> \right]^2 - \frac{1}{2^3\, 3!} \left[\sum_{i,j=0}^{4} z_i z_j <x_i x_j^*> \right]^3 + \ldots$$

$$= \ldots + \frac{1}{8} \left[\sum_{i,j=0}^{4} z_i z_j <x_i x_j^*> \right]^2 - \ldots$$

$$= \ldots + z_1 z_2 z_3 z_4 \; <x_1 x_2^*><x_3 x_4^*> \; <x_1 x_3^*><x_2 x_4^*> \; <x_1 x_4^*><x_2 x_3^*> - \ldots$$

The term of the last line is again the only term containing the factor $z_1 z_2 z_3 z_4$. Equating coefficients of these terms results in Eq.13 which was to be proven.

Appendix II-4 :

ELECTRIC FIELD AUTOCORRELATION FUNCTION FOR SCATTERERS UNDERGOING BROWNIAN MOTION (see p.54)

The scattered electric field $\vec{E}_s(\vec{k},t)$ scattered by N scatterers and detected at time t and at a scattering vector $\vec{k}$ can be written as

$$\vec{E}_s(\vec{k},t) = \sum_{i=0}^{N} \vec{n}_i(t)\, E^o{}_i(\vec{k},t)\, e^{i\vec{k}\cdot\vec{r}_i(t)}\, e^{-i\omega t} \qquad (1)$$

where $\vec{r}_i(t)$ is the position of particle i at time t and ω is the frequency of the incident and scattered field. Here we do not consider depolarized scattering (no optically anisotropic particles) so that all unit vectors $\vec{n}_i$ are equal and independent of time. If the particles moreover do not deform during the time of measurement, the complex amplitude $E^o{}_i(\vec{k},t)$ is time independent. The autocorrelation function $G(\tau)$ thus becomes

$$G(\tau) = \langle \vec{E}_s{}^*(\vec{k},t)\cdot\vec{E}_s(\vec{k},t+\tau) \rangle \qquad (2)$$
$$= \Big\langle \sum_{i=1}^{N}\sum_{j=1}^{N} E^o{}_i{}^*(\vec{k})\, E^o{}_j(\vec{k})\, e^{i\vec{k}\cdot(\vec{r}_j(t+\tau)-\vec{r}_i(t))}\, e^{-i\omega\tau} \Big\rangle .$$

For independent particles, the positions $\vec{r}_j(t+\tau)$ and $\vec{r}_i(t)$ are uncorrelated so that the difference between them is a random vector in time and the phase factor $e^{i\vec{k}\cdot(\vec{r}_j(t+\tau)-\vec{r}_i(t))}$ averages out to zero for $i \neq j$. Thus only the N terms for i = j are left:

$$G(\tau) = N\, |E^o{}_i(\vec{k})|^2 \langle e^{i\vec{k}\cdot(\vec{r}_i(t+\tau)-\vec{r}_i(t))} \rangle\, e^{-i\omega\tau} \qquad (3)$$

For $\tau=0$, $G(0) = N \left|E^{o}_{i}(\vec{k})\right|^2$ and thus the normalized correlation function $g(\tau)$ is

$$g(\tau) = < e^{i\vec{k}\cdot(\vec{r}(t+\tau)-\vec{r}(t))} > e^{-i\omega\tau} \tag{4}$$

where the subscript i was dropped from $\vec{r}_i$.

In order to further compute $g(\tau)$, one has to know what type of motion the scatterers perform. For example, if all particles move with uniform velocity $\vec{v}$ constant in time, then $\vec{r}(t+\tau) - \vec{r}(t) = \vec{v}\tau$. In the case of Brownian motion, one has to introduce the probability $P(\vec{R},\tau)$, the probability that a particle at a position $\vec{r}(t)$ at time t will be at a position $\vec{r}(t)+\vec{R}$ at time $t+\tau$. Note that in Brownian random walk, $P(\vec{R},\tau)$ is independent of t and $\vec{r}$. Thus the average in $g(\tau)$ is given by

$$< e^{i\vec{k}\cdot(\vec{r}(t+\tau)-\vec{r}(t))} > = \int_{scat\ vol} d^3R\ P(\vec{R},\tau)\ e^{i\vec{k}\cdot\vec{R}} \tag{5}$$

The probability $P(\vec{R},\tau)$ satisfies the diffusion equation for a Brownian random walk:

$$\frac{\partial P(\vec{R},\tau)}{\partial \tau} = D\ \nabla^2 P(\vec{R},\tau) \tag{6}$$

which has to be solved with initial condition $P(\vec{R},0) = \delta(\vec{R})$. The solution for this three dimensional problem is

$$P(\vec{R},\tau) = \frac{1}{4\pi D|\tau|^{3/2}} \exp\left[-\frac{|\vec{R}|^2}{4D|\tau|}\right] \tag{7}$$

The solution of the integral above yields

$$< e^{i\vec{k}\cdot(\vec{r}(t+\tau)-\vec{r}(t))} > = e^{-Dk^2|\tau|}. \tag{8}$$

The norm $|\tau|$ is introduced because $P(\vec{R},\tau)$ is a symmetric function of τ.

In the text the norm signs are dropped. The remaining factor $e^{i\omega\tau}$ is also dropped because $g(\tau)$ always appears in a product with $g^*(\tau)$ in the intensity autocorrelation functions. Thus, using the correct notation

$$g(\tau) = e^{-Dk^2|\tau|}\, e^{-i\omega\tau} \tag{9}$$

$$|g(\tau)| = e^{-Dk^2|\tau|}. \tag{10}$$

Appendix IV-1 :

VELOCITY GRADIENT ACROSS A RED BLOOD CELL IN FLOW CELL (see p.90)

We choose the direction of the flow to be the X direction. The flow cell can be approximated by a flow between two infinite parallel sheets. We call the direction perpendicular to the sheet the Z direction.

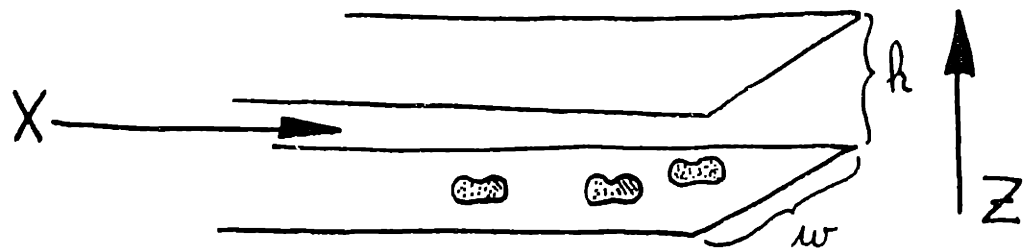

The equation of motion inside this flow is given by

$$\int_S \Phi \, \vec{n} \, d\vec{s} + \int_V \vec{F} \, \rho \, dv = \int_V \rho \, \frac{du}{dt} \, dv \qquad (1)$$

Using Green's formula in the first term, neglecting the external forces $\vec{F}$ (such as gravity) in the second term and considering a steady state flow ($du/dt = 0$), one obtains

$$\int_V \vec{\nabla}\Phi \, dv + 0 = 0 \, . \qquad (2)$$

The gradient of the stress tensor Φ can be written (see for example Milne and Thomson in "Theoretical hydrodynamics") as the sum of the gradient of pressure and the curl of the vorticity which is defined as $\vec{\nabla} x \vec{u}$:

$$- \vec{\nabla}\Phi = - \vec{\nabla}p + \eta \, \vec{\nabla} x (\vec{\nabla} x \vec{u}) = 0 \qquad (3)$$

where η is the viscosity of the fluid. Now $\vec{\nabla}x\vec{\nabla}x\vec{u} = \vec{\nabla}(\vec{\nabla u}) - \nabla^2\vec{u}$ and the first term is zero because the fluid is incompressible ($\vec{\nabla u} = 0$). Moreover, the pressure gradient has a non zero component only in the X direction and $\nabla^2\vec{u}$ contributes only the term in z. One thus obtains the equation of motion for our case:

$$-\frac{\partial p}{\partial x} + \eta\frac{\partial^2 u}{\partial z^2} = 0 \ . \tag{4}$$

The general solution is of the form

$$u = A + B\,z + \frac{1}{2\eta}\frac{\partial p}{\partial x}\,z^2 \tag{5}$$

which, with the boundary conditions u=0 for z=0 and z=h (no flow at the sheets), yields the solution

$$u = \frac{1}{2\eta}\frac{\partial p}{\partial x}\,(h - z)\,z \ . \tag{6}$$

What is $\partial p/\partial x$? It is found through the flow rate equation

$$\frac{dV}{dt} = w\int_0^h u(z)\,dz \tag{7}$$

where V is a fluid volume, h is the separation of the sheets and w is the width of the flow channel. It yields

$$\frac{\partial p}{\partial x} = \frac{dV}{dt}\,\frac{1}{w}\,\frac{12\eta}{h^3} \tag{8}$$

and

$$u(z) = 6\,\frac{dV}{dt}\,\frac{(h - z)\,z}{wh^3} \ . \tag{9}$$

Substitution of the the flow cell width and sheet separation $w = 8\times10^{-3}$m and $h = 5\times10^{-4}$m and using the maximum flow rate of $dV/dt = 0.15$ cc/min = 2.5×10^{-9} m^3/sec, one finds that the velocity u(z) at the top of the RBC

($z = 2 \times 10^{-6}$ m) is

$$u(z=2\mu m) = 1.5 \times 10^{-8} \text{ m/sec} . \qquad (10)$$

The fact that these flow rates are sufficient to deform the RBCs demonstrates that they are highly deformable, which is essential for their function. Indeed, they have to go into and get back out of capillary blood vessels that are narrower than they are in order to deliver oxygen to tissue.

Appendix IV-2 :

DIFFUSION OF OXYGEN INTO MICROCAPILLARY (see p.111)

The appropriate diffusion equation for the case of oxygen diffusion into the microcapillary from one leaky end, is the one dimensional diffusion equation for a semi infinite medium (see for example Crank in "The mathematics of diffusion"):

$$\frac{\partial^2 p}{\partial x^2} = \frac{1}{D}\frac{\partial p}{\partial t} \tag{1}$$

with

$$p(x, t<0) = 0 \tag{2}$$

$$p(x=0, t>0) = \text{constant} = p_0 \tag{3}$$

The corresponding integral equation is

$$\int_0^\infty dt\ e^{-mt}\frac{\partial^2 p}{\partial x^2} - \frac{1}{D}\int_0^\infty dt\ e^{-mt}\frac{\partial p}{\partial t} = 0 \tag{4}$$

Integration by parts for the second term yields just one term because the boundary term is zero through the boundary condition of Eq.(3). Using the following notation for the Laplace transforms

$$\overline{p}(t) = \int_0^\infty dt\ e^{-mt}\ p(t) \tag{5}$$

yields a simple equations in the Laplace transforms:

$$\frac{\partial^2 \bar{p}(t)}{\partial x^2} - \frac{1}{D} m \bar{p}(t) = 0 \qquad (6)$$

At $x=0$, $\bar{p}(t)=p_0/m$ and thus the solution to Eq.(6) is given by

$$\bar{p}(t,x) = \frac{p_0}{m} e^{-xn} \quad \text{with } n^2 = \frac{m}{D} \qquad (7)$$

Extracting $p(t,x)$ from $\bar{p}(t,x)$ requires taking the inverse Laplace transform from $\bar{p}(t,x)$ which yields (see any tables of Laplace transforms):

$$p(t,x) = p_0 \left[1 - \operatorname{erf} \frac{x}{2(Dt)^{1/2}}\right] \qquad (8)$$

$$= p_0 \left[1 - \frac{2}{\pi^{1/2}} \int_0^{x/2(Dt)^{1/2}} e^{-\eta^2} d\eta\right] .$$

The erf function is tabulated. The plot below shows the fraction of the assymptotic pressure p_0 as a function of time at $x = 0.5$ cm from the open edge. The values used were $D = 2 \times 10^{-5}$ cm²/sec and $p_0 = 150$ mmHg.